# Piezoelectric Energy Harvesting: Modeling, Optimization, and Experimental Study of Transient Charging Behavior

by

Shahriar Bagheri

A Thesis submitted to the Faculty of Graduate Studies of

The University of Manitoba

in partial fulfillment of the requirements of the degree of

DOCTOR OF PHILOSOPHY

Department of Mechanical Engineering

University of Manitoba

Winnipeg, Canada

Copyright © 2019 by Shahriar Bagheri

**Abstract**

Piezoelectric Energy Harvesters (PEH) are complex dynamic electromechanical systems. As such, derivation of an accurate model that can describe system's behavior under different operating conditions is challenging. Moreover, the interconnection between the piezoelectric transducer and any forms of power conditioning and storage further complicates the modeling process. This thesis tackles the problem of modeling the transient operation of a PEH during the charging process of an external storage device through electrical interfacing circuits. A semi-theoretical model is proposed based on the Euler-Bernoulli beam theory. The model takes into account the electromechanical coupling effects of the piezoelectric material, as well as the dynamic process of charging an external storage capacitor. The effects of an standard interfacing circuit with diode bridge rectifier and a non-linear synchronous switching circuit on the transient charging dynamics are modeled and comprehensively studied. Additionally, an experimental test setup is developed to validate the efficacy of the developed model and to further investigate the effect of different interfacing circuits on the energy harvesting system.

Furthermore, the problem of finding the optimal design parameters for a PEH is considered. A new simulation-based optimization procedure is proposed with the goal of acquiring the optimal geometric and circuit design parameters that lead to higher energy harvesting efficiency and also enhance the obtained electrical power. The basis of the optimization platform is the developed semi-theoretical model of the energy harvesting system. In order to avoid the time and space (memory)

complexities during the computer optimization caused by the expensive-to-evaluate Objective Function (OF) (i.e. simulation model) combination of Artificial Intelligence (AI) and Evolutionary Algorithm (EA) is used to facilitate the optimization process, while maintaining the required accuracy. More precisely, a computationally efficient Neural Network (NN) model is first trained based on a set of training data obtained from the simulation model. Performance and accuracy of the NN training is studied using available statistical methods. Second, a Genetic Algorithm (GA) optimization performs a block-box optimization procedure, using the trained NN model for OF evaluation. Finally a thorough analysis of the optimal design parameters obtained from the optimization process is provided.

# Acknowledgment

First and foremost, I would like to thank my supervisor, Prof. Nan Wu, and my co-supervisor, Prof. Shaahin Filizadeh. Thank you for taking me on as your student and for all the professional support over the past four years. My professional and personal growth is because of your sincere guidance. I am forever in your debt.

My sincere appreciation goes to the members of the examination committee, Prof. Lihua Tang (university external), Prof. Cyrus Shafai (departmental external) and Prof. Olanrewaju Ojo (departmental internal). Thank you kindly for agreeing to be part of my examining committee. I am thankful for all the enjoyable discussions we had over the past four years and also your invaluable feedback on this thesis. My gratitude to the amazing administrative staff, Kris Taylor, Roxana Semchuk and Bernice Ezirim, at the Department of Mechanical Engineering. Your great work and kind support to graduate students should not go unnoticed. Furthermore, financial support from the Natural Sciences and Engineering Research Council of Canada (NSERC) and the University of Manitoba (Graduate Enhancement of Tri-Council Stipends - GETS) is also greatly appreciated.

I would also like to thank my beloved partner-in-crime Parisa. Thanks for being with me every step of the way. Thank you for all the encouragement and the endless emotional support in all stages of my Ph.D. studies. Last but not least, my mother, Afsaneh, and my brother, Babak. I am grateful for the trust you have in me which allowed me to choose my own path. None of this would have been possible without your unlimited support.

# Dedication Page

This thesis is lovingly dedicated to my mother, Afsaneh Shojaie.

# List of Publication

### Journal Papers

1. S. Bagheri, N. Wu, and S. Filizadeh, "Modeling of capacitor charging dynamics in an energy harvesting system considering accurate electromechanical coupling effects," *Smart Materials and Structures*, vol. 27, no. 6, p. 065026, 2018

2. S. Bagheri, N. Wu, and S. Filizadeh, "Numerical modeling and analysis of self-powered synchronous switching circuit for the study of transient charging behavior of a vibration energy harvester," *Smart Materials and Structures*, 2019, (https://doi.org/10.1088/1361-665X/ab070f)

3. S. Bagheri, N. Wu, and S. Filizadeh, "Application of artificial intelligence and evolutionary algorithms in simulation-based optimal design of a piezoelectric energy harvester," *Ready for submission*

### Conference Paper

1. S. Bagheri, N. Wu, and S. Filizadeh, "Simulation-based optimization of a piezoelectric energy harvester using artificial neural networks and genetic algorithm," in *28th IEEE International Symposium on Industrial Electronics (ISIE), Vancouver, Canada*, p. TBD, IEEE, 2019

2. A. Keshmiri, S. Bagheri, and N. Wu, "Simulation-based optimization of a non-uniform piezoelectric energy harvester with stack boundary," in *International Conference on Advances in Electroceramic Materials (ICAEM), Vancouver, Canada*, p. TBD, WASET, 2019

# List of Copyrighted Materials

Materials used in chapter 3 and chapter 4 of this thesis are reproduced, with modifications from:

1. S. Bagheri, N. Wu, and S. Filizadeh, "Modeling of capacitor charging dynamics in an energy harvesting system considering accurate electromechanical coupling effects," *Smart Materials and Structures*, vol. 27, no. 6, p. 065026, 2018, (https://doi-org.uml.idm.oclc.org/10.1088/1361-665X/aabe9e)

2. S. Bagheri, N. Wu, and S. Filizadeh, "Numerical modeling and analysis of self-powered synchronous switching circuit for the study of transient charging behavior of a vibration energy harvester," *Smart Materials and Structures*, 2019, (https://doi.org/10.1088/1361-665X/ab070f)

Upon transfer of the copyright to the Institute Of Physics (IOP) publishing, the right to include the final published version of the mentioned records were granted back to the authors for the purpose of inclusion in the thesis.

# Contents

# List of Tables

# List of Figures

# Acronyms

| | |
|---|---|
| AC | Alternating Current. 17, 19, 22, 72 |
| ANN | Artificial Neural Network. 98, 100, 101, 107 |
| DC | Direct Current. 15, 17, 19, 22, 59 |
| DSSH | Double Synchronous Switch Harvesting. 25 |
| EA | Evolutionary Algorithm. 9, 30 |
| ESSH | Enhanced Synchronized Switch Harvesting. 23, 25 |
| GA | Genetic Algorithm. 30, 98, 109, 110, 112, 115–117, 125, 128–132, 136, 137 |
| IC | Integrated Circuit. 26 |
| MDOF | Multi Degree-of-Freedom. 18 |
| MEMS | microelectromechanical systems. 1 |
| MLP | Multi Layer Perceptron. 103, 105, 131, 137 |
| MSE | Mean Square Error. 123, 124 |
| NN | Neural Network. 98, 100–110, 116, 119, 120, 122, 123, 125, 126, 129, 131, 132, 136, 137 |
| OF | Objective Function. 31, 100, 108–112, 114–116, 125, 126 |
| PEH | Piezoelectric Energy Harvester. x, 3–6, 8–11, 16–18, 20–22, 26–34, 45, 52, 60, 63–65, 76, 83, 96–99, 109, 119, 129, 134–137 |
| PMN | Lead Magnesium Niobate. 22 |

PT Lead Titanate. 22
PV Photovoltaics. 2, 4
PZT Lead Zirconate Titanate. 13, 14, 22

RF Radio Frequency. 3, 4
RLC Resistor-Inductor-Capacitor. 59
RMS Root Mean Square. 83–85, 87, 89, 90

SDOF Single Degree-of-Freedom. 18, 20, 27, 70, 136
SECE Synchronous Electric Charge Extraction. 23–25, 138
SSHC Synchronized Switch Harvesting on Capacitor. 23
SSHI Synchronize Switch Harvesting on Inductor. 22–25, 27, 28, 53, 55–60, 63, 64, 68, 71, 76, 77, 81, 84, 89, 90, 93, 95, 96, 135

# Chapter 1

# Introduction

*"If you want to find the secrets of the universe, think in terms of energy, frequency and vibration."*

Nikola Tesla

## 1.1 The Big Picture

It has now been over two decades that discussions about regenerative energy sources, specifically, power sources for portable devices, off-the-grid electronic circuits, and microelectromechanical systems (MEMS), have surrounded the scientific community. On one hand, the prospect of creating self-powered electronic systems and devices, and on the other hand, technological advancements in power electronics, including the ability to manufacture micro-powered circuits and sensors, created strong incentives for development of novel energy harvesting methodologies. Many researchers studied multiple aspects of the relatively new field of energy harvesting. Some progress were made, but the journey is nowhere near the end.

The term "*energy harvesting*" is broadly used to describe the process of acquisition, conversion, and storage of energy from different ambient energy sources such as wind, solar or mechanical vibration. Energy harvesting is believed by many researchers to have the potential of powering up portable and/or remote electronic devices. Portable devices, to the most part, require a reliable power source to maintain proper functionality. Non-regenerative power supplies, such as batteries, have long been the main source of power for the operation of low-power portable electronic circuits. However, shortcomings associated with such power supplies justify the pursuit for a better, cheaper, and more environmentally friendly substitute to power electronic circuits [10].

Conventional batteries are commercially available and have good reliability. However, environmental considerations and replacement costs prevent batteries from being a suitable candidate for powering wireless devices [11]. Furthermore, in many applications battery replacement could be tedious, due to the location of the device (e.g., aerospace applications), or impose unnecessary risks (e.g., implantable biomedical devices such as pacemakers) [12]. In such cases, scavenging energy from the environment could potentially overcome some, if not all, the pitfalls of the traditional low-power energy sources.

Different means by which the ambient energy can be transformed into utilizable electrical energy exists. The type of the dominant energy source in the environmental usually determines the transduction mechanism. For instance, if the energy harvester is constantly exposed to sunlight (i.e solar energy), but is in a relatively static environment, then obviously a solar energy harvester (e.g. Photovoltaics (PV)) is a better option than a motion harvester (e.g. piezoelectric or induction). Among

the most common types of energy harvesters are solar, thermal, Radio Frequency (RF) and motion. Various transduction mechanisms exist for each energy harvesting method. Each mechanism offers a number of advantages and suffers from multiple shortcomings.

Among various types of energy harvsting schemes, scavenging energy from ambient mechanical vibration attracted a lot of attention. Three main transduction mechanisms for vibration energy harvesting are: electromagnetic, piezoelectric, and electrostatic. Among these methods, piezoelectricity has been constantly at the centre of attention of the scientific community due to its innate advantages. For instance, PEHs are considered to possess relatively high power densities (i.e. the ratio of the harvested electrical power to the volumetric size of the harvester, $W/cm^2$) when compared with harvesters employing other transduction mechanisms (e.g. thermal conversion) [13, 14]. It is also hard to neglect the fact that mechanical vibration is an integrated part of the environment, and therefore in most situations, mechanical vibration is abundantly available in the proximity of the electrical load [15].

Table 1.1[1] tabulates the power requirements for a number of electronic devices and sensors, and the output power range for different energy harvesting schemes. As can be seen in Table 1.1, a piezoelectric transducer can generate relatively low level of electric power (a range of approximately hundreds of microwatt to a few tens of miliwatt [17]). While still on the lower-end of the power spectrum, PEH can supply several devices and sensors, such as hearing aids, light sensors and accelerometers. Nonetheless, improving the efficiency and power generation capability of the PEH have been a constant endeavor.

[1]This table is put together from the data obtained from [13] and [16]

Table 1.1: Power requirements for typical electronic devices and sensors, and the power generation capability of common harvesters.

| Power Requirement | Typical Electronic Devices/Sensor | Energy Harvesting Technology |
|---|---|---|
| 10 nW | $\mu_{PC_{shutoffmode}}$ | mini PV |
| 100 nW | Quartz oscillator | |
| 10 $\mu$W | RFID tags | RF |
| 100 $\mu$W | Hearing aid | Motion |
| 10 mW | Low power wireless network | Thermal |
| 100 mW | Bluetooth receiver | PV |
| 1 W | OLED display | – |
| 10 W | Laptop/Tablet | – |

An investigation into the literature reveals that there are still fundamental challenges in development and real-world implementation of regenerative energy sources. From a practical standpoint, in most cases the raw electrical power obtained from an energy harvesting device is not directly utilizable. Since the intensity of the ambient energy varies constantly, the generated electric power is not always consistent. Therefore, the harvested power needs to be conditioned and sometimes stored before it could supply the electrical load efficiently.

Consequently, real-world PEHs are generally comprised of three main elements: a vibrating structure, a conversion mechanism (i.e. the piezoelectric material), and a conditioning and storage apparatus. These basic elements are depicted in Figure 1.1. All three elements are of paramount importance in the operation and overall efficiency of the harvester, and should therefore be considered, if accurate

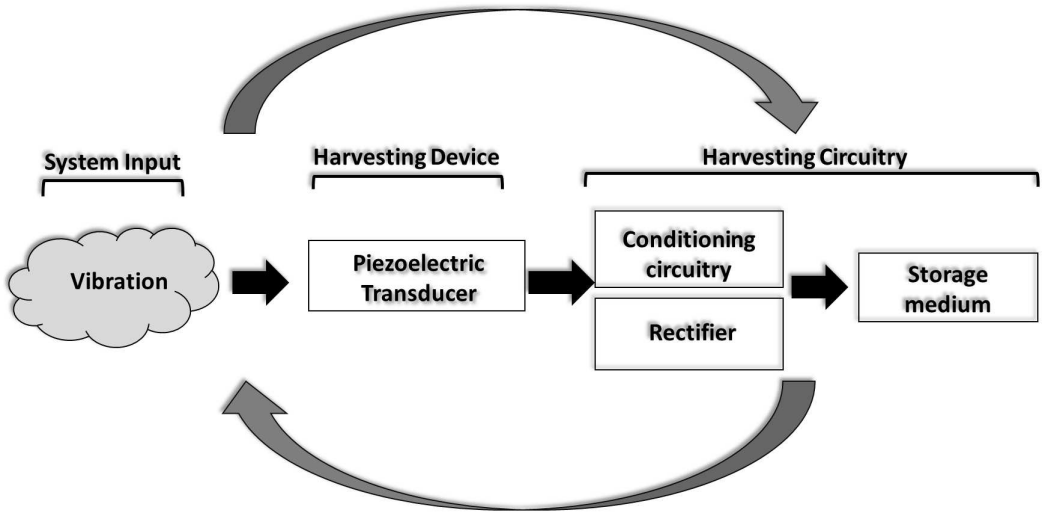


Figure 1.1: Basic components of a PEH

analysis of the system is required. Nonetheless, the effect of these elements on the overall operation of the PEH is usually overlooked.

PEH is a dynamical system and can therefore be described mathematically. An accurate mathematical model that can predict system's behavior under different operating conditions is beneficial, and is in fact required to fully understand and study the system. A proper mathematical description of the system would allow designers to study different aspects of the energy harvesting system through simulation, and optimize the design to achieve higher efficiency. Additionally, improving the power density through computer optimization is one way to enhance the power harvesting capability of energy harvesters. Computer optimization algorithms usually rely heavily on a model, or a description of the system.

However, while browsing through the literature it was determined that the electromechanical coupling effect, as well as the effect of conditioning and storage circuitry is often overlooked during the modeling process. In addition, the efficiency

of the harvested power and the operation of the system during transient is missing from most of the analyses available in the literature to date.

## 1.2 Thesis Statement and Objectives

### 1.2.1 Thesis Statement

The main focus of this thesis is on energy harvesting through piezoelectric materials. The aim is to model the behavior of these harvesters in the context of an interconnected system, as was shown in Figure 1.1, and then use the model to study and analyze the operation of PEHs more closely. Proposed model should possess the following two main attributes: first, the model should adequately capture the feedback electromechanical coupling effect of the piezoelectric material, and second, the model should take into account the effect of the external interfacing and storage circuitry. Additionally, the thesis aims to develop an optimization framework, built upon the mentioned simulation model, and to investigate the effects of different system parameters (e.g. geometric parameters and circuit elements) on the overall operation and efficiency of the energy harvesting system.

### 1.2.2 Objectives

The main objectives of this thesis are further categorized into two sub-objectives as follows.

**Objectives for PEH Modeling**

i. To develop an accurate mathematical model of the PEH. This model should:

(a) consider the accurate continuum-mechanical model of the vibrating structure;

(b) take into account the electromechanical coupling effect of the piezoelectric material;

(c) be able to properly capture (or, should be easily modifiable to do so) the effect of different interfacing circuits on the operation of the energy harvester;

(d) provide an accurate representation of the system during transient operation;

(e) include the effect of the charging dynamics of a capacitive load on the piezoelectric material;

(f) have the potential to be used in the context of a computer-based optimization problem.

ii. To design a suitable test setup and validate the proposed model experimentally. The experimental test setup should include:

(a) a vibrating mechanical structure coupled with piezoelectric materials;

(b) commonly used interfacing and storage circuits (a standard interfacing circuit with diode bridge rectifier and a storage capacitor, and a non-linear synchronized switching circuit);

(c) a number of sensors with acceptable accuracy to measure the physical variables during experimentation.

iii. To analyze and compare the energy conversion efficiency and generated power output of the commonly used interfacing circuits during charging of an external storage capacitor;

iv. To use the developed model and study the behavior of the PEH under different working conditions (i.e. perform parametric studies).

**Objectives for PEH Design Optimization**

i. Properly define a simulation-based optimization problem with the objective of finding the optimal design parameters of the harvester;

ii. determine which optimization technique is more suitable to be used for this particular problem;

iii. thoroughly examine the results of the optimization process.

### 1.2.3 Research Questions

In order to meet the objectives, following questions are ought to be answered.

I. What are the main challenges in PEH modeling and simulation?

II. How does different interfacing circuits affect the charging dynamics in PEH?

III. What parameters mostly affect the power harvesting efficiency in PEH and why?

IV. What is the proper way to define an optimization problem in the context of PEH design?

## 1.3 Organization of the Thesis

This remainder of this thesis is organized as follows. Chapter 2 provides an in-depth review of the currently available literature in the area of energy harvesting through piezoelectricity. The purpose of the literature survey is threefold: first, it provides an objective analysis of different mathematical modeling approaches for PEHs, second, it examines several energy generation/harvesting efficiency enhancement methodologies, and third, it presents currently available optimization methods for PEH optimal design. Energy harvesting efficiency enhancement techniques span over a wide range of methods including modifications to the mechanical structure and/or the interfacing circuit, all of which are discussed in chapter 2. Chapter 3 introduces the proposed mathematical model and the iterative numerical procedure for a typical PEH with a cantilever beam. Two different interfacing circuits (the standard interfacing circuit with a full-diode rectifier, and the non-linear synchronous switching circuit) are modeled with details outlined in chapter 3. The theoretical model of the beam coated with piezoelectric patches is obtained first, followed by a numerical solution that considers the effect of the transient charging dynamics and electromechanical coupling effect. The experimental test setup developed to validate the proposed model, and the series of experimental studies performed are presented in chapter 4. Several discussions around the experimental results, and the results obtained from various parametric studies are also provided in chapter 4. Chapter 5 describes the simulation-based optimal design problem of a PEH. The proposed optimization scheme benefits from available machine learning and Evolutionary Algorithm (EA) optimization tools. Finally, chapter 6 concludes the thesis by reiterating the main contributions, and suggesting several future research directions.

# Chapter 2

# Literature Survey

*"We have found a new method for the development of polar electricity in these same crystals, consisting in subjecting them to variations in pressure along their hemihedral axes."*

In a letter by Pierre and Paul-Jacques Curie announcing their discovery.

The interdisciplinary nature of energy harvesting and piezoelectric energy harvesting in particular, creates a situation where the topic is approached by a broad audience from across multiple scientific disciplines. Consequently, while this chapter aims to cover the state-of-the-art research in the areas of PEH modeling, simulation and optimization, fundamental principles of piezoelectricity and vibration-based energy harvesting, along with a brief summary of piezoelectric transduction mechanism are also provided.

The chapter presents a thorough discussion on modeling of energy harvesting systems with piezoelectric materials. An in-depth analysis of current state-of-the-art methods in PEH modeling and simulation is provided. That includes the mathematical description of the vibrating structure, as well as description of the generated voltage on piezoelectric material and power. Some of the shortfalls associated with each modeling approach discussed are also highlighted. Furthermore, a thorough overview of recent power enhancement methods involving modifications to the mechanical structure and the use of electrical interfacing circuits is presented. Primarily, the focus is on the non-linear electric interfacing via the synchronous switching technique. Finally, the use of computer optimization techniques for power enhancement is discussed.

In short, the literature survey presented in this chapter aims to answer the following key questions:

i. What are the fundamental working principles of a piezoelectric energy harvesting system?

ii. What are the main attributes/components of a practical PEH?

iii. Why is modeling important and what are the attributes of a good system model?

iv. What are the current state-of-the-art approaches to power enhancement in PEH?

v. How can optimization techniques help increase the efficiency and power output of the PEH?

## 2.1 Fundamentals of Piezoelectricity

### 2.1.1 Brief Historical Remarks

History is a delicate subject matter. Perhaps just like any other historical subjects, a scientific breakthrough is ought to be recited with great caution. Nonetheless, discussing any subject matter (science included) without recognizing the pioneers and individuals who laid the foundation and made significant contributions to the field is morally questionable and ethically debatable. Therefore, this section provides, what could only be described as a glimpse into the history of piezoelectricity, as it is known today. The hope is that this way, the rest of this thesis is better put into context. There are of course great sources available (e.g. [18, 19]), that an interested reader can refer to, should he/she wants to know more about how this field emerged into what it is today.

During the late 19th century the Curie brothers, Pierre and Jacques, were conducting several experiments on different types of crystals including, among others, tourmaline and quartz. It was during those experiments that they first encountered the interesting property of certain types of crystals to generate surface-bounded electrons when mechanically deformed. The term "*piezoelectric*" originating from the Greek word *"piezein"* (meaning *"to press"*), was later emerged to distinguish this property from the so-called *"pyroelectric"* effect (i.e. the electrical charge generated on certain types of crystals when heated). The brothers first documented their findings in a french scientific journal ([20]) in 1880. So in essence, the Curie brothers laid the foundation of what is now referred to as the piezoelectric field.

What the Curie brothers discovered originally, was later referred to as the "direct"

piezoelectric effect. The "converse" (or inverse) piezoelectric effect, which is the mechanical deformation of the crystal subjected to an electric field, was mathematically predicted in 1881 by another french physicist Gabriel Lippmann ([21]) based on the rules of thermodynamics. The inverse piezoelectric effect was later experimentally confirmed, once again, by the Curie brothers.

After their original discovery, the Curies continued their effort to characterize different aspects of the piezoelectric phenomenon through systematic experimental tests. Other researchers, including but not limited to the German physicist Woldemar Voigt, set to determine the relationship between piezoelectricity and the structure of the crystal. This further triggered an enormous effort during the 1950's to synthesize materials with higher electromechanical coupling than the crystals found in nature. As a result, the field was revolutionized after the development of piezoceramic materials after the World War II, which exhibit significantly higher electromechanical coupling effects, compared to their natural counterparts. Perhaps the most noticeable breakthrough was the development of Lead Zirconate Titanate (PZT) type materials. Variations of the originally developed PZT materials are still largely in use today.

On the practical side, perhaps the earliest application of piezoelectricity can be traced back to the World War I. The application involved a Sonar system based on piezoelectric quartz crystal that generated 50 KHz signals in order to detect and identify submarines. Many applications of piezoelectric transducers that began during the 1950's are still in use today. Among familiar examples are commercial piezoelectric accelerometers, microphones and crystal oscillators.

### 2.1.2 Basic Principles and Constitutive Equations

A commercially available piezoelectric ceramic, in it's simplest form, is comprised of a piezoelectric material sandwiched between two surface electrodes as shown in Figure 2.1. When the ceramic is subjected to mechanical strain, electric polarization proportional to the strength of the applied mechanical strain is produced on the surface of the material due to the direct piezoelectric effect. Surface electrodes surrounding the piezoelectric material then collect the generated electric charge. On the other hand, as Lippmann [21] argued, the converse piezoelectric effect should also exist simultaneously to guarantee thermodynamic consistency. This means that the generated electric charge causes the piezoelectric ceramic to deform mechanically. This is in fact the nature of the electromechanical coupling effect in piezoelectric materials.

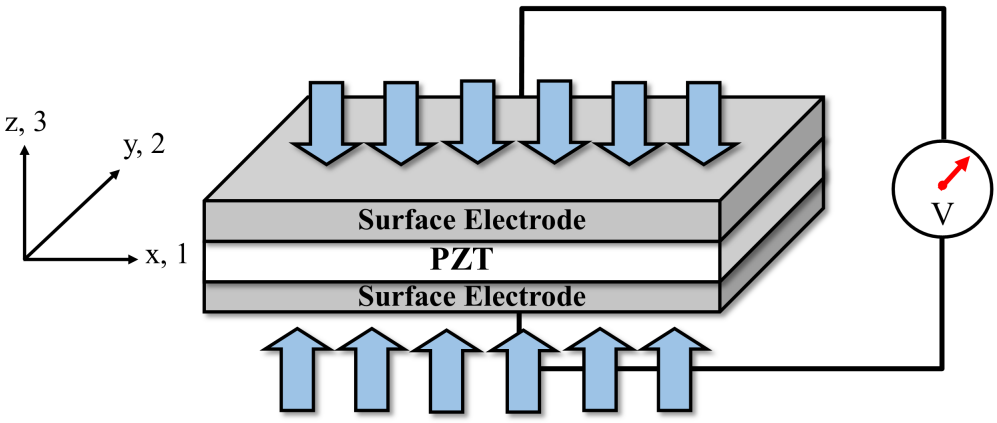


Figure 2.1: Schematic of a piezoelectric transducer under mechanical stress.

Synthetic piezoelectric ceramics, such as PZT-5, are manufactured and artificially poled, through the so-called poling process. The poling process involves subjecting

the ceramic to a strong Direct Current (DC) electric field at a certain temperature. The result of the poling process is permanent polarization of the ceramic, even after the DC source is removed [22].

The IEEE standard on piezoelectricity [23] is generally accepted as the source of the piezoelectric constitutive equations that describe the electromechanical behavior of piezoelectric ceramics. This standard assumes that the ceramic material behaves linearly. For most applications, this is not a limiting assumption since at low mechanical stress and low electrical field intensity, such materials behave (almost) linearly. Piezoelectric constitutive equations describe the relationship between mechanical properties (stress and strain) and electrical properties (electric field and displacement). Therefore, there are four field variables to consider:

- Mechanical stress tensor $T_{ij}$ $(N/m^2)$
- Mechanical strain tensor $S_{ij}$ $(m/m)$
- Electric field tensor $E_k$ $(V/m)$
- Electric displacement tensor $D_k$ $(C/m^2)$

Where the subscripts $i, j, k$ refer to direction in the piezoceramic coordinate system [22]. Field variables are coupled through piezoelectric coefficients. Depending on which of the two field variables are considered as independent variables, different forms of constitutive equations can be structured. As an example, consider the

following stress-electric displacement equation written in matrix form:

$$\begin{bmatrix} T_1 \\ D_3 \end{bmatrix} = \underbrace{\begin{bmatrix} c_{11}^E & -e_{31} \\ e_{31} & \epsilon_{33}^S \end{bmatrix}}_{\mathcal{C}} \begin{bmatrix} S_1 \\ E_3 \end{bmatrix} \tag{2.1}$$

The numerical subscripts $(1, 2, 3)$ correspond to the material axes, where $1 \rightarrow x$-axis, $2 \rightarrow y$-axis and $3 \rightarrow z$-axis, based on the coordinate system depicted in Figure 2.1. Superscripts $S$ and $E$ denote that the variable is evaluated at constant strain and constant electric field, respectively. The matrix $\mathcal{C}$ contains the elastic compliance coefficient ($c_{11}^E = \frac{1}{s_{11}^E}$), the piezoelectric constant ($e_{31} = \frac{d_{31}}{s_{11}^E}$), and the dielectric constant ($\epsilon_{33}^S = \epsilon_{33}^T - \frac{d_{31}^2}{s_{11}^E}$).

Equation (2.1) is based on Euler-Bernoulli assumptions for thin beams and is only valid if the piezoelectric ceramic is thin enough so that any stress component other than the 1-D bending moment is negligible. Furthermore, the electrodes are assumed to be placed perpendicular to the z-axis (3 direction). Further description of the constitutive equations including the derivation for thick beams formulas can be found in the Appendix A of Erturk and Inman [24].

## 2.2 Mathematical Modeling of PEH

Generally speaking, a PEH is comprised of at least three main elements: a piezoelectric transducer (usually a piezoceramic in the form of stack, disk, plate etc.), a vibrating mechanical structure, and, a conditioning and storage circuitry . The piezoceramic, either under vibration itself or mechanically bounded to a substrate

vibrating structure (such as a beam or plate) generates certain amount of electric charge. The generated output voltage is conditioned through an electronic conditioning circuitry and then stored in an storage device, or, is used to recharge a battery. Most electronic circuits that are the receiving-end of the harvested electrical power require constant (usually DC) power to operate. Therefore, existence of some means for voltage conversion (e.g. conversion from Alternating Current (AC) to DC), voltage treatment, or storage is inevitable when dealing with real-life applications.

It is needless to say that vibration to electrical energy conversion through piezoelectricity has been widely studied. A comprehensive review of power harvesting from vibrations is provided by Sodano *et al.* [25]. Apart from the applications of piezoelectric energy harvesters, many researchers set to understand the behavior of these devices and proposed mathematical methods to model systems using piezoelectric transducers. Considering that energy harvesting research, and particularly piezoelectric transducer, is by nature multi-disciplinary, researchers from a wide spectrum of disciplines have tackled the problem of modeling a PEH.

In order to judge whether a model sufficiently describes the behavior of the harvester, the proposed model must accurately describe the behavior of the system in both mechanical and electrical domains. In the work of Erturk and Inman [26], different approaches to piezoelectric harvesters modeling were thoroughly studied and issues with each modeling logic and the underlying assumptions were clearly outlined. The focus of the authors was on the mechanical properties of each model. A model that solely focuses on the mechanical aspects, and fails to accurately consider the electrical circuitry (i.e., interfacing and storage circuit), or vice versa, is not able to provide the required accuracy.

An investigation into the literature of the PEHs modeling reveals several different classes of mathematical models, each of which attempts to describe the electromechanical behavior of the energy harvesting system. These classes range from the so-called Single Degree-of-Freedom (SDOF) models (also known as the lumped parameter models), to Multi Degree-of-Freedom (MDOF) models, to approximated distributed parameter models, and even analytical distributed parameter models. Although there are modeling approaches within each class that are significantly different in the way that they consider the electromechanical coupling effect, the general modeling theme is nonetheless similar.

SDOF models (e.g. [27–30]) are generally built upon the concept of a mass-spring-damper system. Different variations of the SDOF models exist in the literature. For instance, authors in [27] use passive circuit elements (i.e., inductor, resistor, capacitor) to describe the mechanical portion of the system. This concept was initially introduced by Flynn and Sanders [31]. This is an interesting approach that helps simplify the analysis by replacing the harvesting system with an equivalent electrical circuit. Different circuit anaylsis tools could then be used to study the behavior of the system. Nonetheless, this approach is not immune to the issues associated with SDOF modeling. As explained by Erturk and Inman [26], SDOF models are not considered accurate for piezoelectric harvester modeling, mainly due to the simplification of the electromechanical coupling term(s).

Distributed parameter models, to the best of this author's knowledge, were originally proposed by Erturk and Inman [32]. This approach proposes a closed-from analytical solution using Euler-Bernoulli beam theory. The electromechanical coupling term considered in the distributed parameter model is based on the constitutive

relations [23] of the piezoceramic described in section 2.1.2, and is therefore capable of accurately modeling the effect of the generated electrical charge on the mechanical vibration response of the system. The model propsed by Erturk and Inman [32] was experimentally validated for a bimorph cantilever beam in [33]. Although the distributed parameter model proposed by Erturk and Inman [32] accurately considers the coupling effects, the external electrical circuit was simplified with only a resistive load, which is not an accurate charging circuit to harvest piezoelectric energy. As mentioned earlier, practical harvesters utilize power conditioning and storage circuitry that cannot be necessarily modeled as a simple resistive load. Several papers have considered more realistic interfacing circuits [34–37]. For instance, Lan *et al.* [34] study the effect of AC and DC interfacing circuits on a bistable piezoelectric energy harvesting system. Although authors consider the effect of rectifying circuitry for the DC interfacing scenario of the system coupled with nonlinear magnetic forces, the simplified electromechanical coupling term in the motion governing equations are prone to errors addressed by Erturk and Inman [26], and the charging dynamics of the filter capacitor and its effect on the piezoelectric voltage is not considered.

In other papers [35–37], an equivalent electrical circuit comprised of a current source in parallel with a capacitor is used to model the piezoelectric element in the mechanical structure of the system. Wickenheiser *et al.* [37] investigate the effect of the charging process of an external capacitor in systems with different levels of electromechanical coupling effect. Although the electrical part of the model is closer to the practical system when compared with the resistor model, to easily obtain the electromechanical voltage and power outputs and simplify the system parameters optimization process, the mechanical structure equations in [37] are based on a

SDOF model. Therefore, the electromechanical coupling effect is still not quite accurate, especially for any structure subjected to excitation frequencies higher than its first natural frequency. Based on [38], the error resulting from this method for predicting the relative motion at the tip of the beam is very high and even increases for the higher vibration modes. Thus, the SDOF approach requires a correction factor and/or modification in the modeling process.

## 2.3 Efficiency enhancement in PEH

It was mentioned earlier that PEHs require a vibrating host structure, a conversion mechanism (i.e. the piezoelectric material), and conditioning or storage apparatus. Any efficiency enhancement should therefore include a modification/adjustment of one the three main elements of the energy harvesting system just described. While an in-depth analysis and detailed review of all available power enhancement methods in vibration energy harvesters is obviously outside the scope of this work, this section presents an overview of power enhancement methodologies in PEHs. An interested reader can refer to available reviews on the topic (e.g. [15, 39–42]) for a more comprehensive analysis.

Traditionally, most research in the area of PEH was focused on linear resonant harvesters. In linear resonators, a vibrating structure, such as a cantilever beam, was placed under dynamic (and usually harmonic) motion. The physical design of the beam in the case of the linear resonator played an important role in the overall effieicny of the system. The goal was usually to match the natural frequeny of the beam with the frequency of the harmonic motion in order to benefit from

the resonance phenomenon, and therefore obtain higher output electrical power. However, over the past decade, several methods involving mechanical nonlinearity (e.g. [43–45]), the use of bi-stability (e.g. [46–48]) or general modifications to the geometric shape of the harvester ([49–51]) were proposed.

### 2.3.1 PEH power enhancement via mechanical modification

Modifications to the mechanical structure in order to benefit from the intrinsic mechanical non-linearities can overcome some of the major drawbacks of resonant (linear) vibration energy harvesters [43, 45, 52, 53]. Perhaps the most noticable issue with linear PEH, is the poor harvesting efficiency for non-resonance vibration frequencies. In resonant vibration harvesters, if the vibration pattern of the host structure deviates even slightly from the resonance frequency, the efficiency of the power harvesting system will be deteriorated significantly. In the works of Erturk and Inman [52] and Hajati and Kim [53], impressive power improvement were reported, in part, due to the wider frequency range of the newly proposed energy harvesting system exploiting non-linearity. Other example of efficiency enhancment through mechanical modification include the use of tapered beam as opposed to the conventional rectangular beams that was reported by Keshmiri *et al.* [44]. A recently published article by Tran *et al.* [39] conducts a comprehensive critical review of the performance enhancement achieved through non-linearity.

Another key element that also plays an important role in the efficiency of energy extraction is the type of piezoelectric material used in the PEH. Different piezoelectric materials exhibit different levels of electromechanical coupling, that can directly impact the power efficiency of the PEH. The most common type of piezoelectric

material is the PZT. However recently, there has been different studies [54–56] that showed single crystal Lead Magnesium Niobate (PMN) Lead Titanate (PT) type piezoelectric material, are also viable alternatives to the widely used PZT-type materials for energy harvesting applications.

Despite aforementioned breakthroughs that involves improving efficiency of harvested power through mechanical modifications and material properties, power obtained from PEH is still quite limited to the range of approximately hundreds of microwatt to a few tens of miliwatt [17]. As mentioned in section 2.2, electronic circuits usually require constant DC, and as such, existence of some means for voltage conversion (e.g. conversion from AC to DC), voltage treatment, or storage is inevitable when dealing with real-life applications.

### 2.3.2 PEH power generation enhancement via interfacing circuits

The family of synchronous techniques for energy enhancement in piezoelectric energy harvesting began to appear in 2005 and very rapidly became popular in the scientific arena. In a paradigm shifting idea, Guyomar *et al.* [6] for the first time proposed the notion of a non-linear interfacing electrical circuit in which the non-linear processing was applied directly to the generated voltage on the piezoelectric patch. The first technique, called Synchronize Switch Harvesting on Inductor (SSHI), later refered to as the parallel-SSHI technique, was introduced, and has been at the centre of attention for more than a decade. Since the original idea was reported in 2005, significant effort was made toward further research and development of these techniques. Nowadays, multiple varieties of the so-called synchronous techniques exist, while the research in

this area is still on-going. Each method is trying to overcome a particular shortfall of the previous synchronous switching method. [7, 9, 57–60]. Some of the main categories of synchronous techniques include:

- Synchronize Switch Harvesting on Inductor (SSHI) [6]
- Synchronous Electric Charge Extraction (SECE) [7]
- Enhanced Synchronized Switch Harvesting (ESSH) [8]
- Synchronized Switch Harvesting on Capacitor (SSHC) [9]

Figure 2.2 illustrates typical circuit architectures for these interfacing circuits. It should be mentioned however that modified versions of these architectures exist in the literature, and therefore implementation of these interfacing circuits are not restricted to the designs depicted in Figure 2.2. While at first glance these methods may appear to be fundamentally different, a closer investigation reveals that the common denominator in all these methods is the minimization of wasted charge due to self-discharging and recharging of the internal piezoelectric capacitor. What is different, however, is the realization of the switching idea especially when self-powered operation is intended.

SSHI method takes advantage of the dielectric nature of the piezoelectric element by reversing the charge polarity on the piezoelectric element at the point of zero velocity of vibration (i.e., the point where displacement extremum occurs). The voltage inversion results in a cumulative process that increases the magnitude of the generated voltage [17]. In order to achieve this voltage inversion, a voltage processing unit comprised of an electrical switch and an inductor is connected in

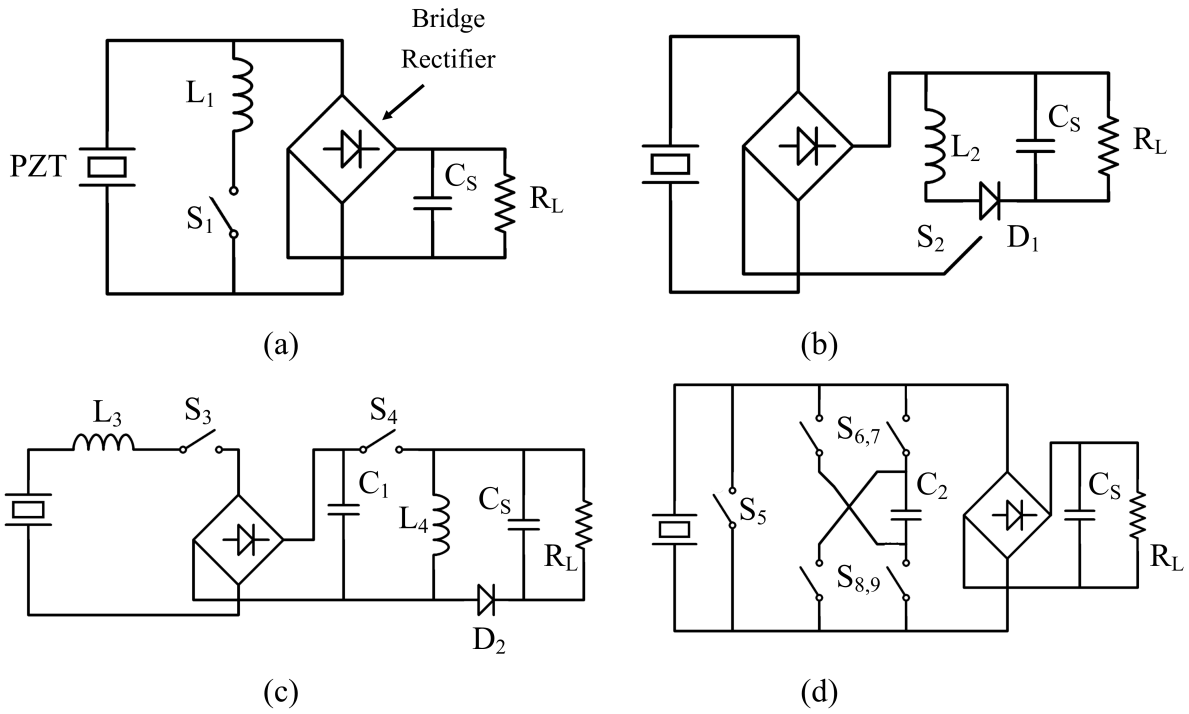


Figure 2.2: Typical circuit architecture for different synchronous switching techniques: (a) Parallel-SSHI [6], (b) SECE [7], (c) ESSH [8] and (d) SSHC [9]

parallel (parallel-SSHI [6]), or in series (series-SSHI [61]) with the piezoelectric active element. Significant efficiency improvement was reported by many researchers for weakly coupled structures and systems operating in an out of resonance condition (e.g. [6, 62, 63]).

Following the original idea of parallel-SSHI, later in 2005, Guyomar *et al.* [7] proposed the SECE technique, which was reported to have increased the harvested power by an extraordinary 400%. The major difference between the two interfacing circuits is that SECE is a two-step process in which the maximum generated piezoelectric energy is transferred to an inductor ($L_2$) in one step, and the piezoelectric element is disconnected from the circuit and the energy stored in the inductor

is transferred to the load in another step. This intermittent connection of the piezoelectric element and the load reduces the dependency of the harvested power to the connected electrical load. Due to this difference, the control law for the $S_2$ switch is different from the control law of the switch $S_1$ in the SSHI circuit.

Other improvments to the original SSHI circuit include the use of magnetic rectifiers [57] or the ESSH [8]. ESSH is an extension to the Double Synchronous Switch Harvesting (DSSH) proposed by the same research group who initially conceived the idea of the SSHI circuit back in 2005 [64]. In DSSH, a combination of a series-SSHI and SECE circuits are used to better control the trade-off between the energy extraction and the mechanical damping effect of the piezoelectric element. Initially, part of the generated power is transferred to $C_1$ while the remaining generated energy is used during the inversion process. The energy stored in $C_1$ is then transferred to $L_4$, and finally to the storage capacitor $C_s$. The depicted ESSH in Figure 2.2 provides an enhancement to the DSSH by allowing better control of the capacitance ratio (i.e. the ratio between $C_1$ and the piezoelectric capacitance).

Recently, a new family of synchronous switching circuits were proposed that use capacitors instead of inductors to perform the voltage inversion process [9, 59, 60]. Removing the inductor reduces the overall size of the interfacing circuit that is of great interest for many practical applications. Du *et al.* [9, 59] proposed an inductor-less bias-flip circuit, while Chen *et al.* [60] proposed an array of capacitors to perform voltage inversion on the piezoelectric material. Despite these improvements, the original parallel-SSHI technique is still in use, and is the subject of various research.

Despite the simple and elegant idea behind the SSHI interfacing circuit, real-world implementation of the switching function is in fact complex; especially, when self-

powered operation is required. It should be noted that the ultimate objective of an energy harvesting apparatus is to produce sufficient energy so that devices and circuits utilizing that energy can be self-powered. Therefore, having an externally powered switching circuit defies this objective. Perhaps the main complication in the operation of a self-powered switching circuit is the control of the switch timing.

According to the theory describe by Guyomar *et al.* [6], switching function should occur intermittently at the peak extremum of displacement of the host structure. There has been several studies on the design and operation of the switching circuit [57, 58, 65–70]. To date, the majority of the switching mechanism reported in the literature belong to the following three categories: mechanical switches (e.g. [57, 71]), Integrated Circuit (IC)s (e.g. [69, 72]), and electronic breakers (e.g. [58, 65, 70]).

Methods using electronic breakers have the advantage of being relatively simple to implement and reliable. Nonetheless, in self-powered realization of the original electronic breaker proposed in [58, 73], certain components in the circuit (i.e. envelope resistor and capacitor, and switch's parasitic capacitance) negatively influence the performance of the PEH. Several comprehensive studies are available (e.g. [15, 74–76]) for PEHs using synchronous switching techniques with an electronic breaker. In these studies, the effect of different components in the circuit on the overall performance of the switching circuit is discussed. Some studies (e.g. [76, 77]) proposed analytic solutions to mathematically describe the harvested electrical power. In fact, there has been extensive research on quantifying the harvested electrical power obtained from piezoelectric energy harvester through different varieties of synchronous switching techniques. The original paper by Guyomar *et al.* [6] presented an expression for the harvested electrical power based on the assumption that the external excitation and

the speed of the mass are in-phase (in the context of the SDOF modeling approach where the energy harvesting system is modeled as a mass-spring-damper system). This is in fact a logical claim for systems operating at resonance. Different from the power expression offered by Guyomar *et al.* [6], Shu *et al.* [76] and Lien *et al.* [62] presented an analytical power expression that is not limited to the in-phase assumption and can predict system's behavior in the vicinity of resonance. The former focuses on parallel-SSHI circuit while the latter investigates the series-SSHI. Both papers focus on steady-state operation of the piezoelectric generator.

Table 2.1 tabulates a comparison between recent works on PEH modeling based on a variety of factors including the electronic interfacing circuit. The majority of studies that tackle modeling of PEHs with SSHI interfacing circuit using electronic breaker suffer from inaccuracies due to followings. First, many of the available analyses focus on steady-state operation. However in reality and for many applications where, for instance, the power requirement of the load is smaller than the power harvested by the PEH (e.g. wireless sensor operating in microvolts range) most power is transferred to the load during transient operation [1, 36, 37]. As such, the dynamics of the system during transient is of paramount importance and should be included in the model. Second, as described in section 2.2, the underlying assumptions involved in the mechanical model when using the so-called SDOF modeling approach, that tends to over-simplify the electromechanical coupling effect, can lead to inaccuracies in the developed mathematical model [26].

Table 2.1: Comparison of relevant research on PEH with different interfacing circuits.

| Publication | Circuit | Host Structure | Inductor | Frequency | Transient study? |
|---|---|---|---|---|---|
| Yang *et al.* [55] | P-SSHI | Cantilever | 52.5 mH | $25 \leq \text{FRF} \leq 45$ | Yes |
| Yang *et al.* [63] | S-SSHI | Reversible nonlinear harvester | 52.5 mH | $5 \leq \text{FRF} \leq 25$ | No |
| Du *et al.* [9] | P-SSHI | Cantilever | 47 mH | 30 | No |
| Chen *et al.* [60] | SSHC | N.A. | N.A. | 110 KHz | No |
| Liang *et al.* [70] | P-SSHI | Cantilever | 47 mH | 30 Hz | No |
| Lu *et al.* [72] | P-SSHI | Cantilever | $940\mu$ H | 225 Hz | No |
| Bagheri *et al.* [1] | Standard rectifier | Cantilever | N.A. | 50 Hz | Yes |
| Wickenheiser *et al.* [37] | Standard rectifier | Cantilever | N.A. | $65, 56, 59$ Hz | Yes |
| Chen *et al.* [78] | P-SSHI | N.A. | 68.2 nH | 50 Hz | No |
| This work | P-SSHI | Cantilever | 50 mH | 50 Hz | Yes |

## 2.4 Optimal Design of PEH

Regardless of the choice of power enhancement schemes described in the previous section, designing a commercially feasible PEH for real-world applications ultimately boils down to the selection of appropriate physical, and if applicable, circuit parameters. Therefore, one fundamental question that needs to be addressed when designing such a system is how can one translate design requirements (e.g. target frequency) into system parameters (e.g. geometric shape, physical dimensions and circuit parameters). This imposes an interesting challenge with significant impact on efficiency and proper functionality of PEHs. Adding to the challenge is the electromechanical nature of the piezoelectric material, as well as the coupling that exists between any interfacing and storage circuit with the piezoelectric transducer. It is

due to such phenomenons that PEH is considered to be a complex dynamical system. System designer is therefore faced with lots of design considerations and unavoidable trade-offs. In many cases, multiple computer simulations are performed to study the applicability of a particular design architecture. This requires a simulation model that can capture the underlying working principles of the system.

One way to address such design challenges in a systematic way is through the use of optimization algorithms. The objective can be maximizing the output electrical power or efficiency for a constrained range of system design variables. This is by no means a trivial task. As Erturk and Inman [26] clearly point out, the nature of the electromechanical coupling effect in piezoelectric materials is rather complex, and, as was described in the proceeding sections, in real-world operating conditions, electrical interfacing and storage circuitry also have an impact on the operation of the harvester. Therefore, obtaining an accurate and reliable definition of the output power is difficult, and often times a more complex simulation models are needed to fully describe this system's behavior.

There have been an increasing number of research in the area of optimal design of a piezoelectric harvester. Similar to the power enhancement schemes explained in section 2.3, efforts to increase the output power through optimization can also be broadly classified into optimization of the mechanical structure, and optimal selection of circuit parameters.

Mechanical design optimization usually deals with the optimization of the physical dimension of the harvester (e.g. length, thickness, width), as well as proper placement of the piezoelectric transducer on the vibrating structure. In the work of Shafer *et al.* [79], a simplified algebraic equation for the output power of the piezoelectric harvester

was proposed, and the optimal thickness ratio was obtained for a bimorph beam without the need to use an optimization algorithm. Dietl and Garcia [80] studied the effects of different beam cross-section areas and shapes, and used gradient search to find the optimal width profile. Zheng *et al.* [81] studied the topology optimization of a piezoelectric cantilever beam under static loading and used gradient-based optimization algorithm to maximize the obtained electrical energy. In the electrical domain, efforts to optimize circuit parameters, for instance, the components of the switching or rectifying circuit [7, 82], or optimization of the resistive loads [83–85] can be mentioned.

With the advancements in many areas of soft computing and optimization, some researchers studied the optimization of PEH using EAs. EAs are nature inspired computer algorithms that are able to find optimal (or close to optimal) solutions to optimization and search problems [86]. For instance, Mangaiyarkarasi *et al.* [87] used multiple Hybrid optimization techniques to obtain optimal geometric design of a unimorph cantilever beam. Bourisli *et al.* [88] studied the optimization of the piezoelectric patch size and placement on a cantilever beam using Genetic Algorithm (GA) in order to find the maximum modal electromechanical coupling for short-circuit, as well as open-circuit operating conditions. Farnsworth *et al.* [89] used an EA optimization technique to optimize the physical dimension of the harvester considering the closeness of the obtained natural frequency with the target frequency.

Regardless of the chosen optimization algorithm, actual optimality of the design parameters in a real-world scenario is directly tied to the accuracy of the power definition used during the optimization process. It should be noted here that often times, it is challenging to propose a single power equation that adequately reflects

the behaviour of a complex dynamic system under different operating conditions. As will be shown in the upcoming chapters, considering even a simple transient behavior of charging a storage capacitor can affect the piezoelectric voltage, and consequently power output of the PEH. One possible solution in such cases is to use a simulation model of the process as opposed to, for instance, an analytical equation for the harvested electrical power. In this case, evaluation of the objective function during optimization occurs by performing a complete system simulation. This area has taken the name simulation-based optimization [1]. Simulation-based optimization has been widely used in many areas of engineering for difficult optimization problems. For a comprehensive review of methods and applications of simulation-based optimization, refer to Gosavi [90].

One key challenge to address is the trade-off between how realistic the simulation model is, and how expensive it is to evaluate the Objective Function (OF) through the simulation model at each iteration of the optimization process. Most optimization algorithms require multiple evaluation of the objective function, and therefore an expensive-to-evaluate OF imposes time and space (i.e. memory) complexities and a computational burden that might be outside the operating range of day-to-day computers.

## 2.5 Summary and Chapter Conclusions

The survey presented in this chapter provided a summary of piezoelectric research while focusing on energy harvesting applications. Fundamental principles and constitutive equations of piezoelectricity along with a brief historical remark were

[1] Also being referred to as optimization via simulation.

provided. This was mostly due to the interdisciplinary nature of the field and was included to assist readers not particularly familiar with the topic at hand. Particular attention was given to mathematical modeling of PEHs. It was found that the dynamic nature of the electromechanical coupling in piezoelectric materials complicates the modeling process of PEH.

A summary of available methods to increase the power generation capabilities of PEH was also presented. The family of synchronous switching methods were thoroughly investigated. It was also shown that geometric design of the harvester and the use of interfacing circuits can have a significant impact on the power generation capabilities of the harvester and should be further studied.

Based on the survey presented in this chapter, a mathematical description of PEH that combines an accurate continuum mechanical model and the precise electrical charging process is still missing. Furthermore, the effect of different interfacing circuits on energy storage should be experimentally investigated. Once accurate model of the system is obtained, one can, in theory, obtain the optimal design parameters of the system using computer simulations and appropriate optimization algorithms. Therefore, in the upcoming chapters, an accurate semi-theoretical model is proposed in which a continuum mechanical model of the beam, as well as the transient dynamics of the charging process are included.

# Chapter 3

# Iterative Numerical Model for a PEH

*"I never satisfy myself until I can make a mechanical model of a thing. If I can make a mechanical model I can understand it."*

William Thomson, 1st Baron Kelvin (a.k.a. Lord Kelvin)

Some of the challenges faced in mathematical modeling of a PEH was discussed in section 2.2. It was also determined that the electromechanical coupling of the piezoelectric material, as well as the coupling effect of the external interfacing and storage circuitry on the operation of the system cannot be neglected in any accurate representation of the system. Given that an accurate model of the PEH system is extremely invaluable, both for performance analysis and system design purposes, this chapter presents the derivation of a novel semi-analytical model of the piezoelectric energy harvester. This model combines accurate continuum mechanical model, and the precise transient dynamics of the charging process through

electrical interfacing circuits, considering the electromechanical coupling effect of the piezoelectric material. Charging dynamics through two of the commonly used interfacing circuits are considered. First, the numerical model is derived for a PEH charging a storage capacitor through a diode bridge rectifier, hereinafter referred to as the standard interfacing circuit. Second, the model is modified to consider the charging process through a non-linear synchronous switching circuit.

This chapter is organized as follows. Section 3.1 introduces the mathematical model and the proposed iterative numerical procedure for a cantilever beam under harmonic tip excitation. Section 3.2 presents the a numerical solution that considers the effect of the charging dynamics and electromechanical coupling effect for standard interfacing circuit. Section 3.3 presents the modifications to the model to consider the charging dynamics through synchronous switching circuit. Section 3.4 highlights some of the limitations of the proposed modeling approach, and finally section 3.5 summarizes the chapter.

## 3.1 Governing Equations of Motion - Thin Beams

Over the years, several beam theories have been developed with different assumptions and various levels of accuracy. One of the commonly used theories, that is both computationally simple and reasonably accurate for a thin beam, is the Euler-Bernoulli beam theory. Although there are simplifying assumptions that can limit the use of this theory for certain operating conditions (these assumptions are highlighted in section 3.4 as some of the limitations of the modeling approach proposed in this chapter), for the general purpose of mechanical modeling of a linear PEH with cantilever beam, the Euler-Bernoulli beam theory is sufficiently accurate.

According to the theory, the partial differential equation governing a uniform beam under lateral forced vibration is as follows.

$$EI\frac{\partial^4 w(x,t)}{\partial x^4} + \rho A\frac{\partial^2 w(x,t)}{\partial t^2} + C_d I\frac{\partial^5 w(x,t)}{\partial x^4 \partial t} = f(x,t) \tag{3.1}$$

where $E$ is the Young's modulus, $I$ is the moment of inertia and assuming a uniform beam with rectangular cross-section $I = \frac{H^3}{12}b$, $\rho$ is the density of the beam structure, $A$ denotes the cross-section area, $C_d$ is the equivalent viscoelasticity damping coefficient (Erturk and Inman [32]), and $w(x,t)$ is the dynamic displacement function that can be found using the method of separation of variables [91]. Equation (3.1) is the building block of the proposed numerical model. It requires two initial conditions and four boundary conditions, as there is a second-order derivative term with respect to time "$t$", and a fourth-order derivative term with respect to location "$x$". There are a number of commonly used boundary conditions, such as free-end, simply supported (pinned) end and fixed-end, just to name a few. The cantilever beam studied throughout this thesis is fixed (clamped) at one end, and free at the other end.

The external excitation function, $f(x,t)$, can also take many different forms. Two commonly used functions that has also been studied in this thesis are the harmonic tip excitation in the form of a point-force ($f_{PF}(t)$), and the relative harmonic base-motion ($f_{BE}(t)$), represented mathematically by the following equations:

$$\begin{aligned} f_{PF}(t) &= F\sin(\Omega t)\delta(x-L); && \text{Point-Force} \\ f_{BE}(t) &= \rho A Y \Omega^2 \sin\Omega t; && \text{Base-Excitation} \end{aligned} \tag{3.2}$$

where $x$ is the location along the length of the beam, $F(N)$ is the amplitude of excitation and $\Omega(rad/sec)$ is the excitation frequency. The Dirac-delta function $\delta$ describes the point-force applied to the beam at $x = L$. $Y(m)$ represents the displacement amplitude of the base [92]. Note that external excitation functions described in equation (3.2) are only functions of time.

According to the traditional vibration theory of continuum structures [91], the forced-vibration response of a thin beam can be obtained using the mode superposition principle, assuming the following form for the deflection function $w(x,t)$:

$$w(x,t) = \sum_{n=1}^{\infty} W_n(x) q_n(t) \tag{3.3}$$

The subscript $n = 1, 2, 3, ..., \infty$ denotes the mode shape number, $W_n(x)$ is the $n$th mode shape function obtained from the free-vibration response, and $q_n(t)$ is referred to as the generalized coordinate and can be obtained from the Duhamel integral. Interested reader can refer to [91], chapter 8, for details on the derivation of the Duhamel integral and solution of equation (3.3).

### 3.1.1 Theoretical, and Numerical Model of a Partially-Coated Cantilever Beam

In this section, the forced vibration response of a cantilever beam partially coated with piezoelectric patches is obtained. Figure 3.1 illustrates the schematic design of the mechanical system, comprised of a cantilever beam of length $L$, width $b$, and thickness $H$; the piezoelectric patch is located at a distance of $L_1$ from the fixed-end

of the cantilever beam, with length $L_p = L_2 - L_1$, width $b$, and thickness $h$. For now, also assume that the beam is under harmonic tip excitation given in equation (3.2).

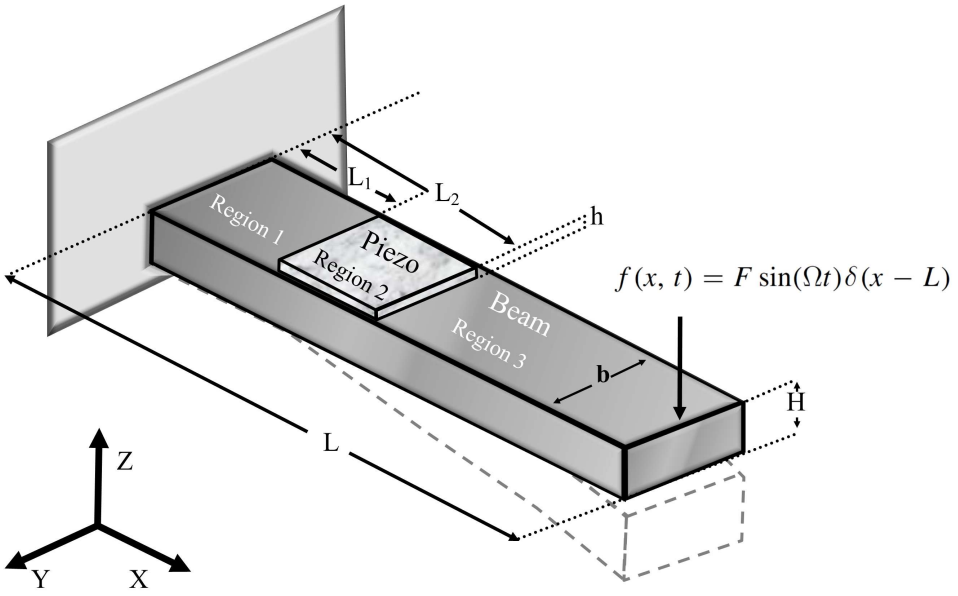


Figure 3.1: Schematic of the piezoelectric cantilever beam under tip excitation

Note that the beam depicted in Figure 3.1 is partially coated with piezoelectric patch. Therefore, the stiffness and mass per length is different at the coating region. As will be explained further in detail in section 3.1.2, the distributed stiffness and mass per length due to the added piezoelectric patch is incorporated into the model through an equivalent stiffness ($EI'$) and mass per length ($m'$), leading to the following governing equation for the piezoelectric-coated section.

$$(EI)' \frac{\partial^4 w(x,t)}{\partial x^4} + m' \frac{\partial^2 w(x,t)}{\partial t^2} = f(x,t) \qquad (L_1 \leq x \leq L_2) \tag{3.4}$$

where the added piezoelectric mass and stiffness are taken into account through the

equivalent mass, $m'$, and the equivalent stiffness ($EI'$), which can be calculated as:

$$\begin{aligned} m' &= \rho H b + \rho' h b \\ (EI)' &= E\Big(\frac{(H-h)^2}{24} + \frac{(H+h)^3}{24}\Big)b + E_p\Big(\frac{(H-h)^2}{24} + \frac{(H+h)^3}{24}\Big)b \end{aligned} \tag{3.5}$$

where $E_p$ is the modulus of elasticity of the piezoelectric.

To further simplify the calculation of the displacement function $w(x,t)$, the beam in Figure 3.1 is divided into three sections: a piezoelectric-coated section in the middle ($L_1 \leq x \leq L_2$), and two non-coated sections ($0 \leq x \leq L_1$ & $L_2 \leq x \leq L$). Using the Euler-Bernoulli beam theory, the governing equations for piezo-coated and non-coated sections can be expressed as:

$$EI\frac{d^4W1}{dx^4} + \rho A\omega_n^2 W1 \quad = 0 \qquad (0 \leq x \leq L_1) \tag{3.6}$$

$$(EI)'\frac{d^4W2}{dx^4} + m'\omega_n^2 W2 \quad = 0 \qquad (L_1 \leq x \leq L_2) \tag{3.7}$$

$$EI\frac{d^4W3}{dx^4} + \rho A\omega_n^2 W3 \quad = 0 \qquad (L_2 \leq x \leq L) \tag{3.8}$$

where $\omega_n$ is the $n$th natural frequency and $W1, W2, W3$ are the mode shapes of the three beam sections corresponding to the non-coated regions (1 and 3), and piezoelectric coated region (2). In this context, $W$ can be re-defined as the mode shape of the entire beam which is obtained by joining the mode shapes of the three

beam sections, $W = W1 + W2 + W3$.

$$
\begin{aligned}
W1 &\begin{cases} \neq 0 & \text{for } 0 \leq x \leq L_1 \\ = 0 & \text{otherwise} \end{cases} \\
W2 &\begin{cases} \neq 0 & \text{for } L_1 \leq x \leq L_2 \\ = 0 & \text{otherwise} \end{cases} \\
W3 &\begin{cases} \neq 0 & \text{for } L_2 \leq x \leq L \\ = 0 & \text{otherwise} \end{cases}
\end{aligned}
\tag{3.9}
$$

Under the assumption that the solution of the mode shape function has the form $W(x) = Ce^{sx}$, with $C$ and $s$ constants as described in [91], the free-vibration solution for different beam sections is obtained:

$$
\begin{aligned}
W1(x) &= C_1 \cos\beta x + C_2 \sin\beta x + C_3 \cosh\beta x + C_4 \sinh\beta x \quad (0 \leq x \leq L_1), \\
W2(x) &= C_5 \cos\beta' x + C_6 \sin\beta' x + C_7 \cosh\beta' x + C_8 \sinh\beta' x \quad (L_1 \leq x \leq L_2), \\
W3(x) &= C_9 \cos\beta x + C_{10} \sin\beta x + C_{11} \cosh\beta x + C_{12} \sinh\beta x \quad (L_2 \leq x \leq L)
\end{aligned}
\tag{3.10}
$$

in which $\beta = \sqrt[4]{(\rho A\omega_n^2)/(EI)}$, $\beta' = \sqrt[4]{(m'\omega_n^2)/(EI)'}$ and $C_*$ are constants that are

obtained from the following boundary conditions:

$$
\begin{aligned}
& W1 = 0, \qquad \frac{dW1}{dx} = 0; \qquad (x = 0) \\
& W1 = W2, \qquad \frac{dW1}{dx} = \frac{dW2}{dx}, \qquad EI\frac{d^2W1}{dx^2} = (EI)'\frac{d^2W2}{dx^2} + \mathcal{M}_e, \\
& EI\frac{d^3W1}{dx^3} = (EI)'\frac{d^3W2}{dx^3}; \qquad (x = L_1) \\
& W2 = W3, \qquad \frac{dW2}{dx} = \frac{dW3}{dx}, \qquad EI\frac{d^2W3}{dx^2} = (EI)'\frac{d^2W2}{dx^2} + \mathcal{M}_e, \\
& EI\frac{d^3W3}{dx^3} = (EI)'\frac{d^3W2}{dx^3}; \qquad (x = L_2) \\
& \frac{d^2W3}{dx^2} = 0, \qquad \frac{d^3W3}{dx^3} = 0; \qquad (x = L)
\end{aligned}
\tag{3.11}
$$

The boundary conditions of equation (3.11) are based on the observation that both the deflection, and the slope ($\frac{\partial w}{\partial x}$), are zero at the fixed-end ($x = 0$) of the structure and, the bending moment and the shear force are zero at the free-end ($x = L$). The cantilever beam boundary conditions used as the case study in this thesis does not limit the applicability of the proposed model. Other structures can also be modeled with the proposed method by easily changing the boundary conditions of equation (3.11). Another important observation is that the bending moment induced by the piezoelectric patch (due to the converse piezoelectric effect described in section 2.1) is included in the boundary and continuity condition through the $\mathcal{M}_e$ term. This bending moment is related to the voltage across the piezoelectric material along its

poling direction ($V_p$), by the following equation.

$$\mathcal{M}_e = \Big(\frac{EHb}{(\psi+\alpha)}\frac{d_{31}V_p}{h}\Big)\frac{H-h}{2} \tag{3.12}$$

where $d_{31}$ is the piezoelectric charge coefficient, $\psi = (EH)/(E_p h)$, and $\alpha = 6$. The generated electric charge $\tilde{\mathbf{Q}}$, and the corresponding voltage $V_p$ are further calculated as:

$$\tilde{\mathbf{Q}} = -e_{31}\int_{L_1}^{L_2} b(\frac{H+h}{2})\frac{d^2w(x,t)}{dx^2}dx \tag{3.13}$$

$$V_p(t) = -\frac{e_{31}(H+h)}{2C_v'}\Big(\frac{dW_{2,n}(x)}{dx}\Big|_{x=L_2} - \frac{dW_{2,n}(x)}{dx}\Big|_{x=L_1}\Big) \tag{3.14}$$

where $W_{2,n}(x)$ is the $n$th mode shape of the beam section coated with piezoelectric material. Furthermore, $e_{31}$ is the piezoelectric constant and $C_v'$ is the capacity-per-unit-width of the piezoelectric patch.

As mentioned earlier in chapter 2, in many practical applications the generated electrical energy of piezoelectric harvesters need to be stored in a capacitor and/or a battery, before it could be effectively utilized. It was observed from the above equations that the generated voltage on piezoelectric patch affects the mechanical vibration response of the host beam (in the form of a bending moment exerted to the beam) due to the converse electromechanical coupling effect. Additionally, $\tilde{\mathbf{Q}}$ and $V_p$ are functions of the vibration motion of the structure. Therefore, any voltage processing, for instance, through the interfacing and storage circuit, will have an

affect on the vibration pattern of the system. The change in the vibration pattern will in turn affect the electrical power generation of the harvester. As a result of this electromechanical coupling phenomenon caused by the external interfacing and storage circuit, conventional model using Duhamel integration does not lead to an accurate vibration response of the beam coated with piezoelectric patch, if one wants to accurately consider the effect of external electrical circuitry. Consequently, following iterative method is used to solve the forced vibration response for the cantilever beam depicted in Figure 3.1.

### 3.1.2 Forced Vibration Response Through Iterative Method

Considering the eletromechanical coupling effect, which is induced by pizoelectricity charging external capacitor, following iterative process is applied to solve the forced vibration response and the charging process. The total calculation time, $T$, is divided into small discrete time segments, $t_i$, where the subscript $i$ donates the iteration number and $\Delta t = t_{i+1} - t_i$ is the period of calculation. $\Delta t$ should be relatively small in order to gurantee the convergence of the model. Interested reader can refer to [93] for more details on the convergence study. For the first iteration step ($i = 1$), assuming that the beam is initially at rest, the deflection function $w(x,t)|_{t=0}$ and the corresponding velocity $\frac{\partial w(x,t)}{\partial t}\Big|_{t=0}$ are equal to zero. The vibration response of the first iteration time step $(0 \leq t \leq t_i)\Big|_{i=1}$ can, therefore, be obtained using the

Duhamel integral:

$$
\begin{aligned}
w_i(x,t) &= \sum_{n=1}^{\infty} W_n(x) q_{n,i}(t) = \sum_{n=1}^{\infty} W_n(x) \frac{1}{\rho A B \omega_d} \int_0^{t_i} Q_n(\tau) \exp^{\zeta\omega_n(t_1-\tau)} \sin\omega_d(\tau) d\tau, \\
Q_n(\tau) &= \int_0^L f(x,t) W_n(x) dx, \\
B &= \int_0^L W_n^2(x) dx, \\
\omega_d &= \sqrt{1-\zeta^2}\omega_n,
\end{aligned}
\tag{3.15}
$$

where $\zeta$ is the damping ratio and $f(x,t)$ is the external excitation explained in section 3.1. Note that the free-vibration response part of the Duhamel integral solution can be removed from equation (3.15) for the first iteration step due to the zero initial condition assumption explained above.

The dynamic displacement solution of the first iteration step can further be used to calculate the initial condition for the subsequent time steps. For instance, for the second iteration, $(t_{i-1} \leq t \leq t_i)\Big|_{i=2}$ one gets:

$$
w_{i,free}(x,t) = \sum_{n=1}^{\infty} W_n(x) \exp^{\zeta\omega_n(t)} A_n \cos\omega_d t + B_n \sin\omega_d t \tag{3.16}
$$

Note that the constants $A_n$ and $B_n$ can be found from the generalized coordinate

solution $(q_{n,i}(t)\Big|_{i=1})$ of the previous iteration in equation (3.15).

$$\begin{aligned} q_{n,t_1}(t) &= A_n \cos\omega_d t + B_n \sin\omega_d t, \\ \frac{d\ q_{n,t_1}(t)}{dt} &= \frac{d\ \exp^{\zeta\omega_n(t)} A_n \cos\omega_d t + B_n \sin\omega_d t}{dt} \end{aligned} \tag{3.17}$$

Thus, the total vibration response for the second iteration $(t_{i-1} \le t \le t_i)\Big|_{i=2}$ can be obtained by augmenting equation (3.15) with the free-vibration response equation (3.16):

$$\begin{aligned} w_i(x,t) &= \sum_{n=1}^{\infty} W_n(x) q_{n,i}(t) \\ &= \sum_{n=1}^{\infty} W_n(x) \Big[ \exp^{-\zeta\omega_n t} A_n \cos\omega_d t + B_n \sin\omega_d t \\ &+ \frac{1}{\rho A B \omega_d} \int_{t_{i-1}}^{t_i} Q_n(\tau) \exp^{\zeta\omega_n(t_1-\tau)} \sin\omega_d(\tau) d\tau \end{aligned} \tag{3.18}$$

Constants $A_n$ and $B_n$ for $i = 2$ are obtained from equation (3.17) as:

$$\begin{aligned} B_n &= \frac{\frac{dq_{n,i-1}(t)}{dt} \exp^{\zeta\omega_n t} \cos\omega_d t + q_{n,i-1}(t) \exp^{\zeta\omega_n t} \sin\omega_d t}{\omega_d \sin^2\omega_d t + \cos^2\omega_d t} \\ A_n &= \frac{q_{n,i-1} \exp^{\zeta\omega_n, t} - B_n \sin_{\omega_d t}}{\cos\omega_d t} \end{aligned} \tag{3.19}$$

A similar concept can be applied to find the total vibration response for the period $0 \le t \le T$.

## 3.2 Charging Process Through Standard Interfacing Circuit

In the numerical model described above, the exact vibration solution of the beam under harmonic excitation was derived. Nonetheless, in many practical applications a storage apparatus is also included in the system architecture. When a capacitor is used as the storage buffer, the coupling effect of the capacitive load on the PEH should be incorporated into the model. In this section, an iterative procedure is proposed to accurately model the charging and non-charging bi-linear phenomenon of an external capacitor during vibration of the piezoelectric harvester, and the coupling effect of the charging process on the generated charge of the piezoelectric patch, which does affect the mechanical response as well.

Figure 3.2 illustrates a simplified rectification and storage circuit, comprised of four Schottky diodes, a toggle switch, and a storage capacitor donated as $C_s$. Similar to the iteration process explained earlier, the total calculation time is divided into many small discrete time segments $t_i$.

If the toggle switch is initially closed with zero charge on the external capacitor, there will be a current flow from the source (piezoelectric patch) to the external capacitor. Electric charge flowing away from the piezoelectric material will result in a voltage drop on the patch. Therefore, one can assume that the total generated charge obtained through equation (3.13) due to the mechanical deformation of the beam is distributed in the circuit, as soon as the switch connecting the storage

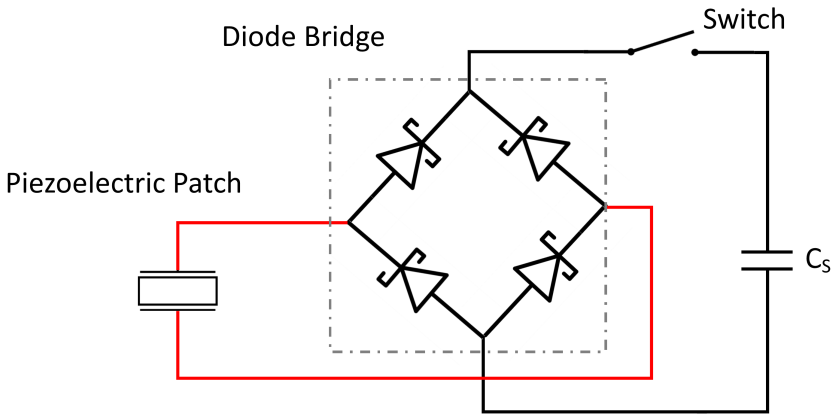


Figure 3.2: Schematic of the standard interfacing circuit with storage capacitor.

circuit to the harvester is closed at $t_{i=1}$.

$$\begin{aligned} \tilde{\mathbf{Q}}_{\mathbf{i}} &= |Q_{p,i}| + Q'_{s,i} \\ Q_{s,i} &= Q_{s,i-1} + Q'_{s,i} \end{aligned} \tag{3.20}$$

where $\tilde{\mathbf{Q}}_{\mathbf{i}}$ is the total generated charge on the piezoelectric patch at the $i^{th}$ iteration; $|Q_{p,i}|$ and $Q'_{s,i}$ are the charge on the piezoelectric material, and the newly added charge to the external capacitor during the period $t_i \sim t_{i+1}$, respectively; $Q_{s,i}$ is the accumulated charge on the external capacitor from the beginning of the charging process up until $t = t_i$. Note that the absolute value of $|Q_{p,i}|$ is used to represent the rectification of the diode bridge circuit. From this point onward and for simplicity of notations, $Q_{p,i}$ denotes $|Q_{p,i}|$. Before proceeding to the modeling of the charging process, one should note that the voltage drop of the diode bridge circuit illustrated in Figure 3.2 must be taken into consideration for any accurate modeling of the piezoelectric energy harvesting process. Although the voltage drop is relatively small (for a generic Schottky diode the drop is approximately $\leq 0.3$) it will affect the

charging process since the total generated charge and voltage of the piezoelectric energy harvester during vibration can also be small.

Assuming that the load resistance is infinite and the external capacitor $C_s$ is initially discharged, the following relationship exists between the voltage across the external capacitor $V_{s,t_i}(t)$ and the piezoelectric patch $V_{p,t_i}(t)$:

$$\begin{aligned} V_{t_i}(t)\Big|_{i=1} &= \frac{Q_{p,i}}{C_p} = \frac{Q_{s,i}}{C_s} + V_{drop}, \\ \frac{Q_{p,i}}{C_p} &= \frac{Q_{s,i-1} + Q'_{s,i} + C_s V_{drop}}{C_s} \Rightarrow \frac{Q_{p,i}}{C_p} = \frac{Q_{s,i-1} + (\tilde{\mathbf{Q}}_{\mathbf{i}} - Q_{p,i}) C_s V_{drop}}{C_s} \end{aligned} \tag{3.21}$$

Note that $Q_{p,i}(t)$ and $V_{t_i}(t)$ are the the total generated charge and voltage due to mechanical deformation at time $t_i$, and $V_{drop}$ is the voltage drop on the diode bridge circuit. $C_p$ is the total capacitance of the piezoelectric patch and is obtained from $C'_v$ ($C_p = (C'_v\, b\, L_p)/(b\, h)$).

The accurate voltage drop of the bridge circuit subjected to different voltages was obtained experimentally and was used in the model. The rationale behind using the experimentally obtained input/output voltage curve instead of the conventional I-V characteristic curve is that in a non-ideal diode, a small amount of current always passes through the diode even for voltages below the forward voltage drop. Figure 3.3 shows the diode voltage input/output curve obtained from the experiment. A second-order polynomial regression is performed to obtain the relationship between the independent variable (i.e., bridge input voltage) and the dependent variable (i.e., bridge output voltage). Thus, an accurate $V_{drop}$ can be obtained in each iteration.

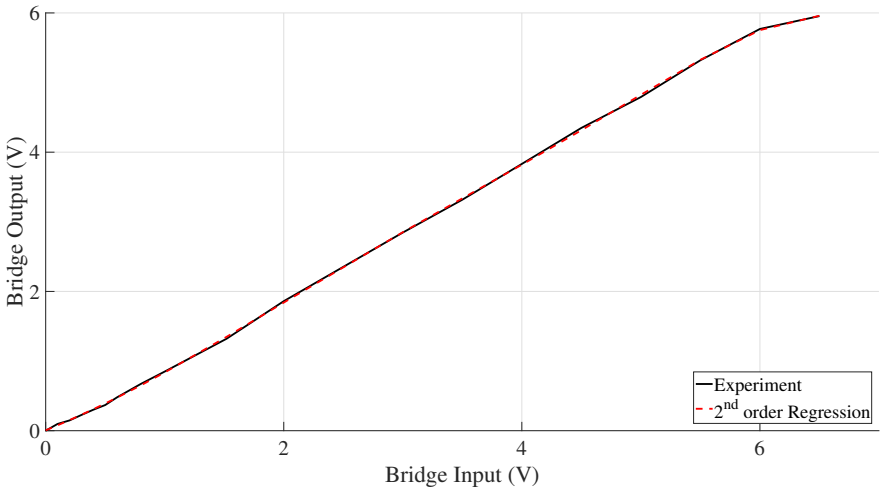


Figure 3.3: Experimental input/output voltage curve of the Schottky diode bridge

Straightforward mathematical manipulation of equation (3.20) and equation (3.21) leads to the following equations, which could be used to obtain the accurate charge on the piezoelectric material and the external capacitor during the charging process:

$$\begin{aligned} Q_{p,i} &= \frac{C_p(Q_{s,i-1} + \tilde{\mathbf{Q}}_\mathbf{i}) + C_s V_{drop}}{C_s + C_p}, \\ Q_{s,i} &= Q_{s,i-1} + Q'_{s,i} = Q_{s,i-1} + \frac{\tilde{\mathbf{Q}}_\mathbf{i} C_s - C_p(Q_{s,i-1} + C_s V_{drop})}{C_s + C_p} \end{aligned} \tag{3.22}$$

Finally, voltages $V_{p,i}$ and $V_{s,i}$ are calculated from equation (3.22) as follows:

$$V_{p,i} = \frac{Q_{p,i}}{C_p}, \qquad V_{s,i} = \frac{Q_{s,i}}{C_s} \tag{3.23}$$

So far, the charging process of the external capacitor is described. It should however be noted that an ideal diode bridge circuit will block current flowing from

the storage capacitor back to the piezoelectric material. Therefore, the bridge circuit acts similar to a logic switch that only allows current to pass in one direction towards the storage capacitor. This leads to the bi-linear phenomenon of the electromechanical coupling effect and is the main reason behind using an iterative method. If $V_{p,i} \leq V_{s,i}$, diode bridge does not conduct. In the non-charging state, assuming that the capacitor retains all its previously stored charge, $Q_{s,i} = Q_{s,i-1}$, which leads to the voltage on the external capacitor remaining constant during non-charging state (i.e. $V_{s,i} = V_{s,i-1}$). However, the voltage on the piezoelectric patch during non-charging depends on whether the previous iteration $(i-1)$ was a charging state or not. The following equations describe the non-charging state voltage on the piezoelectric patch:

$$Q_{p,i} = \begin{cases} \tilde{\mathbf{Q}}_{\mathbf{i}} & \text{for } i-1: \text{ non-charging} \\ Q_{p,i-1} & \text{for } i-1: \text{ charging} \end{cases} \tag{3.24}$$

Furthermore, due to the electromechanical coupling, the generated electrical charge on the piezoelectric material induces a bending moment ($\mathcal{M}_e$) at the two tips of the piezoelectric patch. As mentioned earlier in section 3.1.1, this bending moment can be calculated from the potential difference on the piezoelectric patch using equation (3.12). Although the intensity of the electromechanical coupling varies in different systems and depends on a variety of factors (e.g. the relative size of the piezoelectric patch and the host structure), the effect of this coupling phenomenon on the overall mechanical vibration response should be considered for an accurate modeling of the piezoelectric energy harvesting system.

Since the modeling scheme proposed in this chapter is based on an iterative

process, the bending moment induced by the exact voltage on the patch during charging of an external capacitor or battery can be incorporated into the model. Using the governing differential equation of an elastic curve, one can separately calculate the deflection of the beam induced by $\mathcal{M}_e$ at $x = L_1$ and $x = L_2$ and then use the principle of superposition to obtain the deflection caused by $\mathcal{M}_e$.

$$W_{i,\mathcal{M}_e}(x) = \frac{\mathcal{M}_{i,e}(L_1)x}{2EI} + u(x-L_1)[\theta(L_1)x] + \frac{-\mathcal{M}_{i,e}(L_2)x}{2EI} + u(x-L_2)[\theta(L_2)x] \quad (3.25)$$

where $u(x - L_*)$ represents the Heaviside step function and $\theta$ is the angle between the tangent line and the deflection curve at $L_1$ and $L_2$. In other words, the dynamic response of the beam due to the external harmonic excitation is obtained (the first three vibration modes were considered), then the backward coupling moment is calculated from the remaining voltage on the piezoelectric patch, and finally, through the superposition principle, the total response is obtained. The simplified flowchart depicted in Figure 3.4 demonstrates the numerical calculation process described in this sub section.

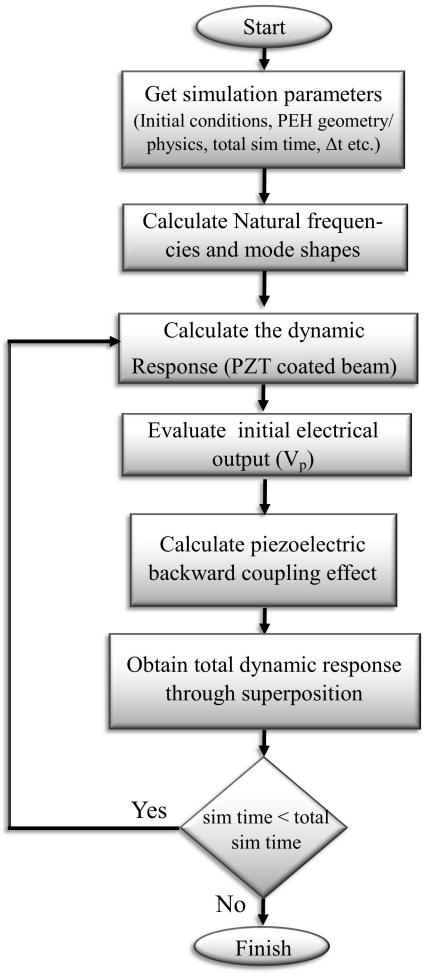


Figure 3.4: Flowchart of the numerical iteration process for calculating the total dynamic response of the PEH.

## 3.3 Charging Process Through Non-linear Interfacing Circuit

Although efficiency enhancement through non-linear processing of piezoelectric voltage is a well-established research area, accurate modeling of the transient dynamics during charging process has not been fully addressed; particularly, when self-powered operation is intended. As will be explained in this section, the self-powered switching

circuitry has an impact on the charging curve and should be considered in the model. Here, the numerical modeling approach presented in section 3.1.2 is augmented to include the effect of the self-powered switching circuit, as well as the transient charging dynamics of storage capacitor. Before proceeding with the description of the model, the operation of the PEH with non-linear processing of voltage is briefly described. For a more detailed description, the reader is encouraged to refer to the original paper by Guyomar [6].

### 3.3.1 Basics of the Non-linear Processing of Piezoelectric Voltage

Figure 3.5 shows the simplified diagram of PEH connected in parallel with the inductor $L_{SSHI}$, through an electrically operated switch $S_{SSHI}$. For ease of analysis, assume that the piezoelectric patch is a pure capacitor with capacitance $C_p$, and that the motion of the beam is harmonic. Under these assumptions, the generated voltage on the piezoelectric material is in phase with the displacement of the structure shown in Figure 3.5 (b). Therefore, displacement extremum of the mechanical structure corresponds to maximum voltage on the piezoelectric patch. For instance, when the beam is at its maximum upward position (point of zero velocity), piezoelectric patch is positively charged with respect to the beam which is negatively charged (assuming that the direction of polarization is positive towards the positive $z$-axis).

The electrical switch $S_{SSHI}$ is almost always open, which means that $L_{SSHI}$ is disconnected from the circuit. If however, $S_{SSHI}$ is closed for a relatively short period of time when displacement extremum occurs ($t_i = t_{ext}$). $L_{SSHI}$ and $C_p$ will be placed in parallel, forming an $LC$ resonant circuit. The $LC$ circuit starts oscillating

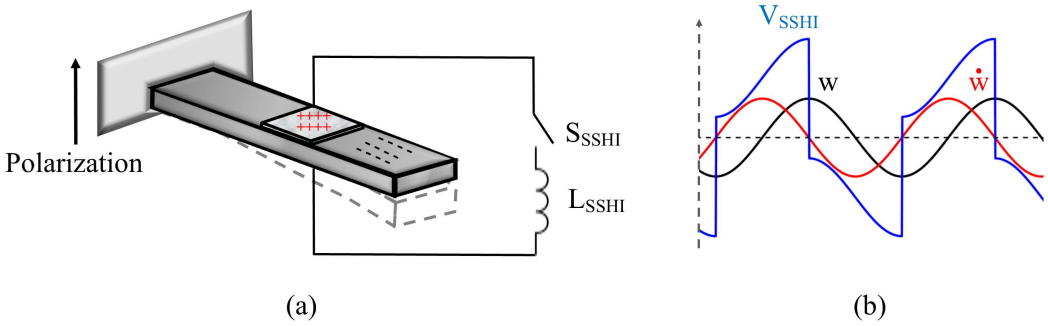


Figure 3.5: (a) conceptual PEH with parallel-SSHI interfacing circuit, (b) waveforms depicting beam displacement ($w$), velocity ($\dot{w}$) and piezoelectric patch voltage ($V_{SSHI}$).

with frequency $f_{SSHI} = 1/(2\pi\sqrt{L_{SSHI} \quad C_p})$ due to resonance. At resonance, the reactance of the inductor and capacitor will cancel each other out, leading to an artificially boosted voltage on the piezoelectric patch. According to the original theory, the switch should remain closed for approximately half the period of electrical oscillation ($\delta_t = \pi\sqrt{L_{SSHI}C_p}$) and then re-opened again for the system to resume normal operation. It is also important that the $f_{SSHI} >>> \Omega$ so that the switching occurs almost instantaneously ($\delta_t <<< \Delta t$).

As a result of this quasi-instantaneous procedure, charge polarities on the piezoelectric patch is reversed, and newly generated charge is added to the existing charge on the patch when the beam starts moving towards the opposite extremum [6]. This voltage inversion process is included in the numerical model and the total available charge and voltage on the piezoelectric patch obtained from equation (3.13) and equation (3.14), are replaced with $\tilde{\mathbf{Q}}_{\mathbf{SSHI}}$ and $V_{SSHI}$, when the SSHI circuit is being studied. Due to the voltage inversion process at the displacement extremum, new voltage and charge on the piezoelectric patch considering the SSHI interfacing circuit

can be obtained as follows.

$$V_{SSHI}(t_{ext}) = -V_{SSHI}(t_{ext})\ e^{\frac{-\pi}{2\lambda}} \tag{3.26}$$

$$\tilde{\mathbf{Q}}_{\mathbf{SSHI}}(t_{ext}) = V_{SSHI}(t_{ext})\ C_p \tag{3.27}$$

where $\lambda$ is the so-called inversion quality factor. Basically, the inversion process causes dissipation of some of the energy stored on the piezoelectric patch [6]. $\lambda$ is a very important factor that directly affects the harvested power. As will be explained in the following chapter, the proposed model enables the analysis of the effect that $\lambda$ has on the overall harvested power efficiency.

At first glance, it appears that implementation of synchronous switching only requires two additional components: the electrical switch $S_{SSHI}$ and the inductor $L_{SSHI}$. However, proper operation of the switch and the detection of correct opening and closing times require additional circuitry, especially, when self-powered operation is intended. The electronic breaker depicted in Figure 3.6 is used to implement the electrcil switch ($S_{SSHI}$). A comprehensive analysis of the electronic breaker is available in the literature (e.g. [15, 58, 70, 73]) and therefore is not addressed here, however, a brief overview of different components of the circuit is provided to help the reader better follow the numerical modeling proposed in this thesis.

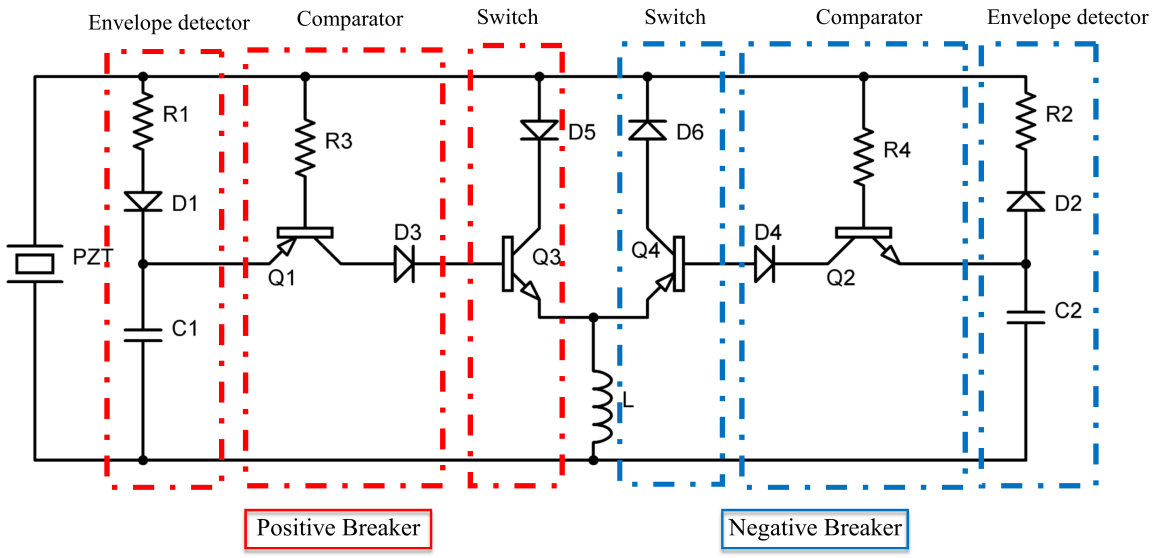


Figure 3.6: SSHI circuit with electronic breaker

### 3.3.2 Synchronous Switching Technique Through Electronic Breaker

Consider the positive breaker depicted in Figure 3.6. The circuit is comprised of three main segments: an envelope detector, a comparator, and, an electric switch. The effect of individual components in the circuit on the overall conversion efficiency is outside the scope of this work and is fully addressed by Liu [15] along with guidelines on component selection. This thesis is mainly concerned with the effect of the self-powered SSHI circuit on the charging dynamics and efficiency from the standpoint of energy harvesting and storage.

Looking at Figure 3.6, it is instantly clear that the circuit is more complicated than the simplified circuit shown in Figure 3.5 which was mainly representative of

the idea of synchronous switching. One major difference that has an impact on the transient charging dynamics of the storage device, which is one of the main subjects of this thesis, is that the envelope detector stays connected to the piezoelectric patch at all times during the operation of the system. Therefore, part of the charge generated on the piezoelectric patch will flow towards the envelope detector in order to charge $C_1$ (or $C_2$ in case of the negative breaker). As such, the envelope detector $RC$ circuit will have an effect on the voltage in the form of a phase lag [15], which together with $\lambda$ are perhaps the two most important parameters to be considered in the circuit. The phase lag is in fact the delay of the switching action relative to the exact position of the voltage extremum [15]. Other elements in the electronic breaker circuit, such as the transistors in the comparator ($Q1$ and $Q2$) and the switch ($Q3$ and $Q4$) also contribute to the loss of power and switching delay which were not included in the proposed modeling scheme. However, it is worth noting that according to one comprehensive study of the switching time delay in self-powered parallel-SSHI circuits by Chen. *et al.* [78], the primary sources of the switching delay were found to be the resistors and capacitors in the envelope detector and the inductor due to the very short period of the switch circuit being included. One can refer to the original paper by Chen. *et al.* [78] for a more detailed discussion on switching delay in SSHI circuits.

In the current proposed model, switching time delay $\varphi$ was considered as a number of the small time step length to simulate the phase lag in the following manner. When the peak value of the voltage is detected at time $t_{ext}$, the voltage inversion is delayed by $\varphi \times \Delta t$. Exact value of $\varphi$ was measured experimentally. Therefore, when using the electronic breaker circuit, the inversion of voltage on the piezoelectric

patch occurs after the voltage extremum. As a result, equation (3.26) and equation (3.27) are modified accordingly:

$$V_{SSHI}(t_{ext} + (\varphi\ \Delta t)) = -V_{SSHI}(t_{ext} + (\varphi\ \Delta t))\ e^{\frac{-\pi}{2\lambda}} \tag{3.28}$$

$$\tilde{\mathbf{Q}}_{\mathbf{SSHI}}(t_{ext} + (\varphi\ \Delta t)) = V_{SSHI}(t_{ext} + (\varphi\ \Delta t))\ C_p \tag{3.29}$$

It should also be mentioned that both these parameters are considered as part of the parametric studies performed in the following chapter.

### 3.3.3 Modification to the Mechanical Model to Include Parallel-SSHI Circuit

To consider the charging dynamics of the external capacitor $C_s$, once again consider the schematic shown in Figure 3.1. Total simulation time T, is discretized into small time segments $t_i$. Assume that the external capacitor is completely discharged. As soon as the output of the parallel-SSHI circuit is connected to the capacitive load $C_s$, electric current will flow towards the storage capacitor. This reduction of electric charge results in a voltage drop on the piezoelectric patch (this phenomenon was observed during experimentation and will be explained in details in chapter 4). The electric charge distribution for the small time period $t_i$ during charging process can be described mathematically as:

$$\begin{aligned} \tilde{\mathbf{Q}}_{\mathbf{SSHI,i}} &= |Q_{p,i}| + Q'_{s,i} \\ Q_{s,i} &= Q_{s,i-1} + Q'_{s,i} \end{aligned} \tag{3.30}$$

where $\tilde{\mathbf{Q}}_{\mathbf{SSHI,i}}$ is the available electric charge on the piezoelectric patch at the $i^{th}$ iteration when connected to the SSHI circuit; $|Q_{p,i}|$ and $Q'_{s,i}$ are the charge on the piezoelectric material, and the charge delivered to the capacitive load over the period $t_i \sim t_{i+1}$, respectively; $Q_{s,i}$ is the cumulative electric charge on the capacitor from the beginning of the charging process up until $t = t_i$. Once again, for the purpose of notational convenience, $Q_{p,i}$ denotes $|Q_{p,i}|$ in order to represent the rectification through diode bridge.

The relationship between piezoelectric voltage $V_{p,t_i}(t)$ and external capacitor voltage $V_{s,t_i}(t)$ can be described as:

$$V_{t_i}(t)\Big|_{i=1} = \frac{Q_{p,i}}{C_p} = \frac{Q_{s,i}}{C_s} + V_{drop},$$

$$\frac{Q_{p,i}}{C_p} = \frac{Q_{s,i-1} + Q'_{s,i} + C_s V_{drop}}{C_s} \Rightarrow \frac{Q_{p,i}}{C_p} = \frac{Q_{s,i-1} + (\tilde{\mathbf{Q}}_{\mathbf{SSHI,i}} - Q_{p,i}) C_s V_{drop}}{C_s} \tag{3.31}$$

Note that similar notations are used for $Q_{p,i}(t)$ and $V_{t_i}(t)$ (total generated charge and voltage due to mechanical deformation at time $t_i$) and also the voltage drop on the diode rectifier $V_{drop}$. Equation (3.31) indicates that once the external storage circuit is connected to the piezoelectric patch, the total available charge on the patch is no longer just a function of the mechanical deformation; Instead, it depends on the charging/not-charging state of the system in the previous time step.

In other words, the electrical coupling that exists between the piezoelectric device and the storage circuit dictates that the available amount of charge split between the piezoelectric patch, and the external capacitor. If $V_{p,i} \leq V_{s,i}$, the diode bridge

blocks the current flow from the piezoelectric patch to the external capacitor and the system will operate at non-charging state. During the non-charging state and under the assumption that the $C_s$ retains all its previously stored charge, $Q_{s,i} = Q_{s,i-1}$, the voltage on the external capacitor remains constant (i.e. $V_{s,i} = V_{s,i-1}$). However, the available voltage on the piezoelectric patch depends on the charging/non-charging state of the previous time step $(i-1)$. Similar to equation (3.24), the voltage on the piezoelectric patch during a non-charging state can be obtained as follows:

$$Q_{p,i} = \begin{cases} \tilde{\mathbf{Q}}_{\mathbf{SSHI,i}} & \text{for } i-1: \text{ non-charging} \\ Q_{p,i-1} & \text{for } i-1: \text{ charging} \end{cases} \tag{3.32}$$

Further mathematical manipulation on equation (3.30) and equation (3.31) is required to calculate the exact charge on the external capacitor and the piezoelectric material, as well as the rate of charge of the external capacitor. During experimentation, it was observed that the charging time of the external capacitor was increased when the SSHI circuit was connected to the piezoelectric patch. The main reason behind this delay in charging is explained next.

Since all electronic components exhibit certain level of resistance towards current flow, the electronic breaker circuit forms an Resistor-Inductor-Capacitor (RLC) oscillation loop with the piezoelectric patch. The total resistance of the RLC loop in the breaker circuit is a combination of the on-resistance of the analog switches, DC resistance of the inductor and all parasitic resistances in the circuit. Determination of the exact value of the RLC loop resistance experimentally is challenging, however, an investigation into the literature reveals a reported value of 20 ohms to 70 ohms for the combined resistance of the RLC loop (e.g. [94]).

Furthermore, the voltage drop that was observed after the capacitive load was first connected to the piezoelectric patch, and the fact that the generated current of the PEH is very small (in the order of a few microamps) result in a large series resistance of the two active diodes in the bridge circuit during each half-cycle of operation. A comparison of different modeling approach for series resistance for Schottkey diodes is available in [95]. Basically, two diodes of the bridge circuit are operating in the non-linear range of the corresponding I-V curve. Consequently, large variations in the diode input voltage ($\Delta V$) and very small variations in the diode current ($\Delta I$), leads to high series resistance ($\frac{\Delta V}{\Delta I} = R_I$) initially after the charging circuit is triggered. Once the voltage on the piezoelectric patch is restored, this series resistance is reduced until it becomes negligible.

In an effort to include the approximate effect of the mentioned resistances on the charging rate of the capacitor $C_s$, the numerical model considers an equivalent series resistance $R_{series}$. Because of the non-linearities in the analog switches and diodes, the value of $R_{series}$ is approximated as a bi-linear function of the voltage on the piezoelectric patch:

$$R_{Series} = \begin{cases} 40\ ohms & \text{for } V_{p,i} \leq 4v \\ 25\ ohms & \text{for } V_{p,i} > 4v \end{cases} \tag{3.33}$$

In reality however, this series resistance is non-linear. An electric charge source with the value corresponding to $Q'_{s,i}$ is considered to be connected in series with $R_{series}$ and $C_s$. The precise amount of the electrical charges on the piezoelectric patch and $C_s$ during the charging process with SSHI interfacing circuit and electronic

breaker can therefore be calculated as:

$$\begin{aligned} Q_{s,i} &= Q_{s,i-1} + [Q'_{s,i}(1 - e^{\frac{-t}{R_{series} * C_s}})] \\ &= Q_{s,i-1} + (\frac{\tilde{\mathbf{Q}}_{\mathbf{SSHI,i}} C_s - C_p(Q_{s,i-1} + C_s V_{drop})}{C_s + C_p})(1 - e^{-\Delta t/(R_{series} C_s)}) \end{aligned} \tag{3.34}$$

$$Q_{p,i} = \frac{C_p(Q_{s,i-1} + \tilde{\mathbf{Q}}_{\mathbf{SSHI,i}}) + C_s V_{drop}}{C_s + C_p}, \tag{3.35}$$

Finally, voltages $V_{p,i}$ and $V_{s,i}$ are obtained from equation (3.35) and equation (3.34), respectively, as follows:

$$V_{p,i} = \frac{Q_{p,i}}{C_p}, \qquad V_{s,i} = \frac{Q_{s,i}}{C_s} \tag{3.36}$$

Once the accurate charge on the piezoelectric material for each iteration step during charging is obtained, the dynamic piezoelectric bending moment $\mathcal{M}_e$ of equation (3.12) at the two tips of the piezoelectric patch can be calculated. This represents the electromechanical coupling effect of the electrical-domain, on the mechanical-domain model. Once again, it is noted that many factors influence the intensity of the electromechanical coupling, nonetheless, an accurate model of the piezoelectric energy harvester should adequately capture the effect of this coupling phenomenon.

## 3.4 Limitations of the Proposed Numerical Model

Mathematical models are approximations of the physical phenomenon they intend to describe. Therefore, all models have inherent limitations and are only valid under a predefined sets of assumptions. The proposed iterative modeling approach described in this chapter is no exception. The model, in its current form, has the following sets of assumptions and limitations:

i. The two primary Euler-Bernoulli assumptions:

   - During deformation, the cross-section of the beam remains planar and normal to the deformation;
   - Deformation angle is small and the beam cross-section does not severely bend as the result of the external loading.

ii. The iteration time step ($\Delta t$) is assumed to be small enough so that the variations of the charge distribution between the piezoelectric patch and the external circuit can be considered linear.

iii. The external capacitor $C_s$ is assumed to be completely discharged at the beginning of the charging process, and that the capacitor can store all the delivered electrical charge without self-discharging.

iv. Envelope capacitors of the electronic breaker circuit are small enough and will be instantaneously charged at each time step.

v. Assumptions involving diodes and transistors in the comparator and the switch of the electronic breaker circuit, more precisely, the voltage drop and

losses due to transistors and diodes in the self-powered implementation of the parallel-SSHI circuit were not explicitly included in the proposed model.

## 3.5 Summary and Chapter Conclusions

This chapter presented a semi-analytical model of piezoelectric-based energy harvesting system. The proposed iterative method was based on the Euler-Bernoulli beam theory. The mechanical model considering multiple beam modes during its vibration was augmented and coupled with a numerical procedure that took into consideration the effect of conditioning (rectification circuit) and storage (charging process of an external capacitor) circuitry. The physical process of charging of the external capacitor by a PEH considering electrical-mechanical coupling effect was explained adequately through an iteration process. The numerical model facilitates the inclusion of charging dynamics of a capacitive load in PEH equipped with SSHI interfacing circuit into the model.

# Chapter 4

# Experimental Evaluation and Parametric Study

*"Nothing is too wonderful to be true, if it be consistent with the laws of nature; and in such things as these, experiment is the best test of such consistency."*

Laboratory journal entry 10,040 (19 March 1849) - Michael Faraday

This chapter presents a comprehensive evaluation of the semi-theoretical model proposed in chapter 3. Several experimental tests, as well as a series of carefully designed parametric studies are performed. The main objective of this chapter is to assess the efficacy and accuracy of the proposed model in predicting the charging dynamics in a PEH. Multiple experimental tests are performed for both standard and parallel-SSHI interfacing circuits. The developed experimental test setup also allows careful analysis and behavioral study of a typical PEH during transient phase of charging a storage capacitor.

The organization of this chapter is as follows. Section 4.1 presents the development of the experimental test setup. Different sensors and components used during experimentation are disclosed. Section 4.2 provides a thorough discussion around the results of multiple experimental tests. The focus is on the transient operation of the PEH during the charging process, and finally, section 4.3 presents the results of the parametric studies using the developed numerical model of chapter 3. Summary and chapter conclusions are highlighted in section 4.4.

## 4.1 Developed Experimental Test Setup

An overview of the developed experimental test setup is depicted in Figure 4.1. This setup is comprised of the following main elements: an aluminum cantilever beam coated with a piezoelectric patch, a signal generator and data acquisition unit, an interfacing and storage circuitry, and finally, a vibration shaker.

The cantilever aluminium beam is partially coated with piezoelectric patches in a unimorph configuration. The piezoelectric patches are glued to the host beam, and are perfectly bonded using an industry standard adhesive (3M Scotch-Weld Epoxy DP420 [96]). Physical and material properties of the host beam, piezoelectric patch and the conditioning circuitry are tabulated in Table 4.1.

The data acquisition system is a four-channel Siemens LMS SCADAS mobile integrated with LMS Test.Lab [97]. An oscilloscope (DSO06014A manufactured by Agile Technologies [98]) provides real-time monitoring of the charging process. A vibration shaker is connected to the beam tip to provide harmonic excitation of the piezoelectric-coated aluminium beam. The sensors used to capture the motion

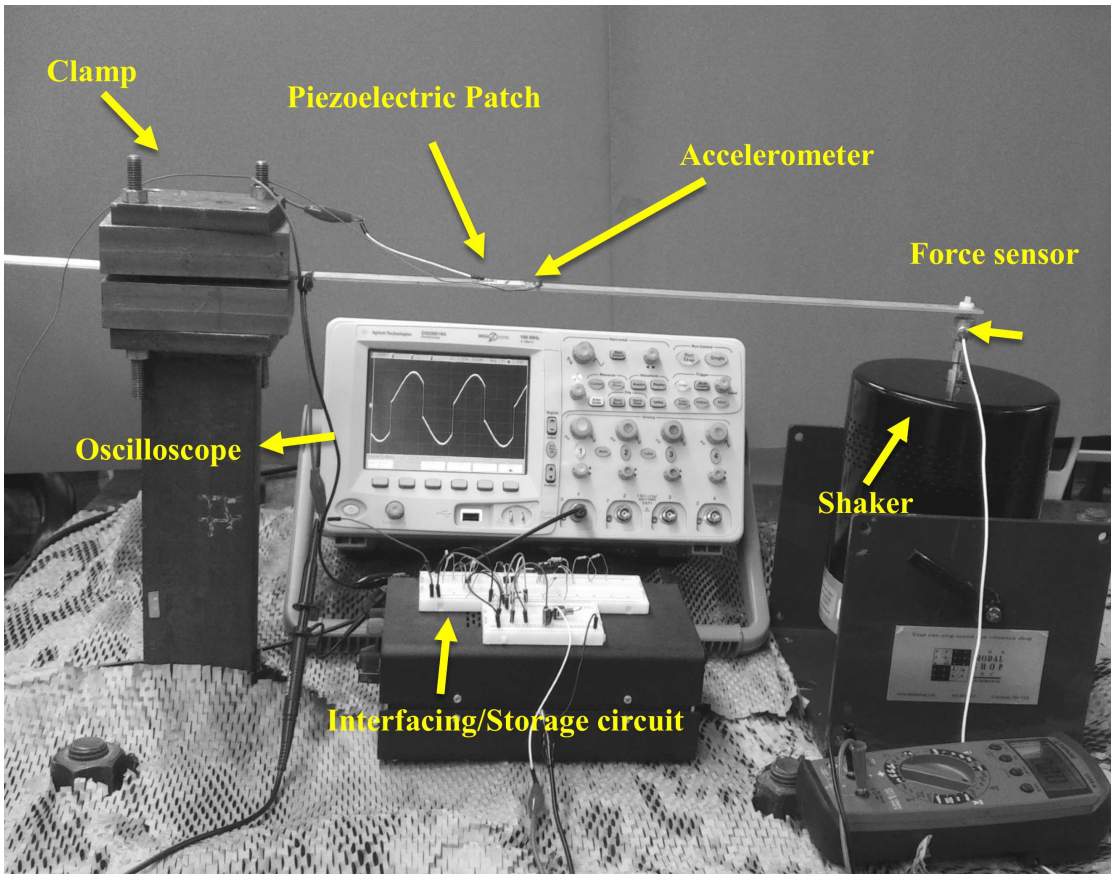


Figure 4.1: Overview of the experimental test setup.

Table 4.1: Physical and geometrical properties of the cantilever beam and the piezoelectric patch.

| Parameter | Host beam | Patch |
|---|---|---|
| Length (m) | $L = 0.5$ | $L_p = 0.0325$ |
| $L_1$ (m) | — | 0.1277 |
| $L_2$ (m) | — | $L_1 + L_p = 0.1602$ |
| Thickness (m) | $H = 0.0027$ | $h = 0.0009$ |
| Width (m) | $b = 0.01905$ | $b = 0.01905$ |
| Young's modulus($N/m^2$) | $E = 6.9e10$ | $E_p = 6.3e10$ |
| Density ($Kg/m^3$) | $\rho = 2800$ | $\rho_p = 7600$ |
| Piezoelectric constant | — | $e31 = -12.5$ |
| Piezoelectric charge coefficient | — | $d31 = -1.75e^{-10}$ |
| Capacitance(F) | — | $C'_v = 5.5311e^{-9}$ |
| Excitation freq. (Hz) = 50 | — | — |

Table 4.2: Standard interfacing circuit components.

| Parameter | Value |
|---|---|
| $C_s$ | $10e^{-6}$ |
| Rectifying Diode | SD101A |
| Toggle Switch | EG2447-ND |

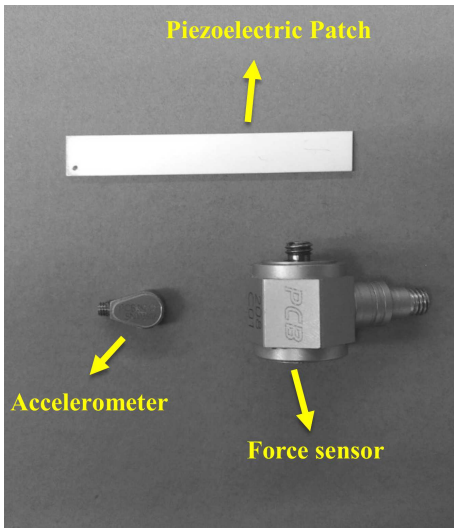


Figure 4.2: Top-view of the accelerometer, force sensor, and the piezoelectric patch used during experimentation.

of the beam, and the amplitude of the harmonic excitation signal, as well as the top-view of the piezoelectric patch used during experimentation are illustrated in Figure 4.2. The accelerometer is a miniature shear ICP sensor (352A21) designed by PCB Piezotronics [99]. The ICP sensor is also glued next to the piezoelectric patch, as was shown in Figure 4.1.

As mentioned before, two different interfacing circuits are considered during experimentation and simulation studies. Figure 4.3 (a) shows the standard interfacing circuit comprised of a diode bridge circuit, a manual toggle switch, and a 10 $\mu$F storage capacitor. The diodes in the bridge circuit are Schottky-type diodes ($1N5817$

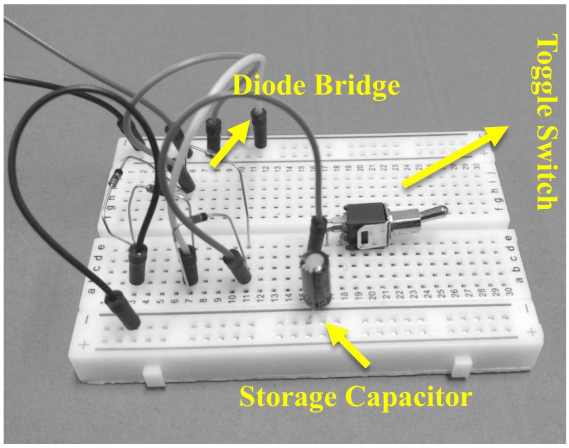


(a)

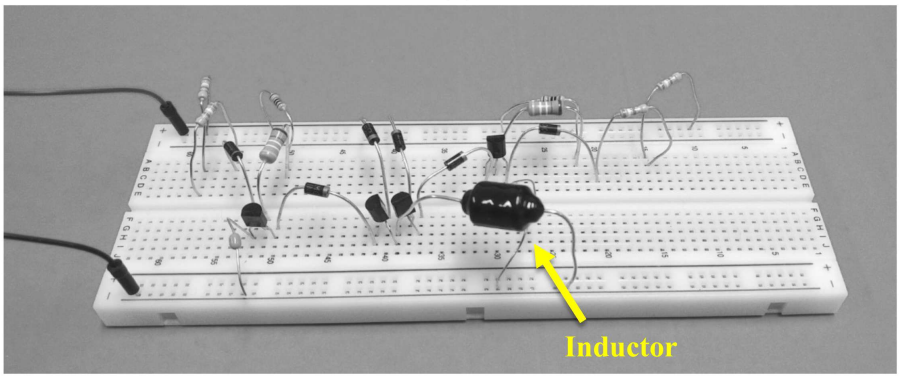


(b)

Figure 4.3: (a) Standard interfacing/storage circuit with diode bridge rectifier, 10$\mu$F storage capacitor and a toggle switch, (b) self-powered parallel SSHI interfacing circuit.

manufactured by Diodes Incorporated [100]). The main advantage of Schottky diodes over regular *p-n* junction diodes is the low forward voltage drop, which is a favorable characteristic for applications involving low voltage/current levels. The manual toggle switch was used to control the start of the charging process.

Figure 4.3 (b) illustrates the self-powered parallel SSHI circuit developed based on the electronic breaker circuit described in section 3.3.1. Values for different components in the SSHI circuit are chosen according to the guidelines available

Table 4.3: Electronic components used in the parallel-SSHI circuit.

| Component | Value |
|---|---|
| R1 = R2 | 8 MΩ |
| R3 = R4 | 700 KΩ |
| C1 = C2 | 330 pF |
| D1 − 6 | $1N4004$ |
| Q1,Q4 | $2N3906$ |
| Q2,Q3 | $MPSA06$ |
| L | 50 mH |
| $\lambda$ | 2.5 |
| $\phi$ | 0.005 |

in the literature (e.g. [15]). Extra attention is given to components used in the envelope detector (specifically, resistors R1-R2, and capacitors C1-C2). Final selected components are tabulated in Table 4.3.

Prior to the validation of the charging process, the validity of the mechanical model is assessed by comparing the natural frequencies and acceleration of the beam under harmonic tip excitation. The first two natural frequencies of the beam were obtained experimentally from an impact hammer modal test. The acceleration data was captured by the ICP accelerometer that was shown in Figure 4.2. A hammer with a load cell attached to its tip is used to apply an impact force to the beam in order to replicate an impulse-like function. The magnitude of the input signal is measured experimentally and is $\approx 0.312$ N. Two peaks at frequencies 9.25 Hz and 55.00 Hz with amplitudes 1.597 $m/s^2$ and 5.064 $m/s^2$ are respectively observed, corresponding to the first two natural frequencies of the beam. This is shown in Figure 4.4. As can be seen in the figure, during this test, the second harmonic was excited more than the first harmonic as the second acceleration peak was higher than the peak corresponding to the first natural frequency. This was in fact due to the

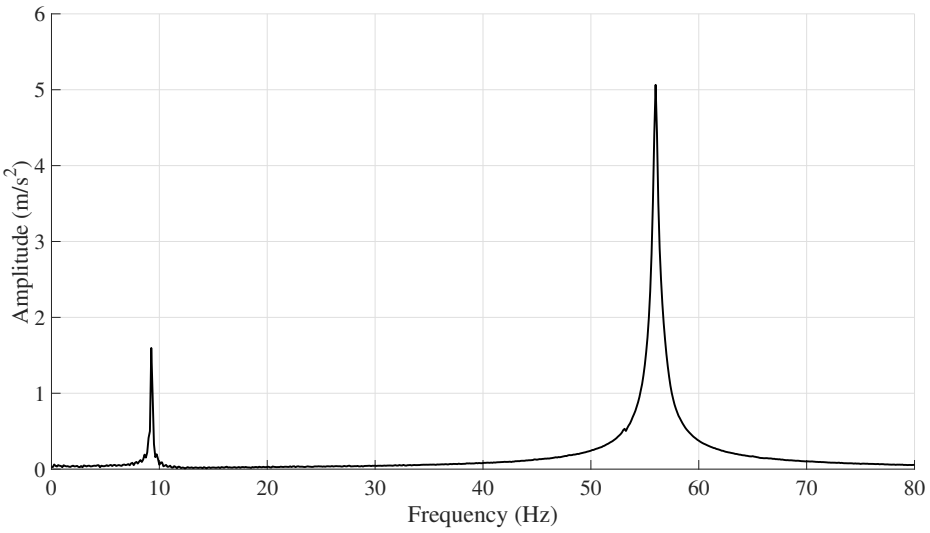


Figure 4.4: First two natural frequencies of the beam from experiment.

positioning of the hammer during the impact hammer test. Numerical simulations based on Euler-Bernoulli assumptions resulted in frequencies of 9.125 Hz and 55.63 Hz that are conforming to the experimental results.

The top plot of Figure 4.5 illustrates the excitation signal of amplitude of around 10 N, and frequency 50 Hz, while the bottom plot shows the acceleration of the beam at $x \approx L_2$. It should be further explained that with only a few exceptions, the majority of the experiments and simulations presented in this thesis consider the excitation frequencies between the first, and the second natural frequency of the beam (while being closer to the second natural frequency). The main rationale behind experimenting around the second resonance frequency of 55 Hz is to showcase the ability of the proposed distributed model with truncated modes in predicting the behavior of the system operating in the proximity of the higher vibration modes. As previously mentioned, SDOF models generally fail to predict system's behavior operating at higher vibration modes where multiple mode shapes determine the

movement of the structure. The model described in chapter 3 is based on the continuous model of the beam and can therefore simulate higher vibration modes (2nd, 3rd, etc.) which leads to a more accurate continuum mechanical model of the cantilever beam. Furthermore, frequencies exciting higher vibration modes result in more significant curvature distribution for similar displacement amplitude and as such, higher electrical output power can be harvested.

The second reason behind using higher excitation frequencies closer to the second vibration mode has to do with the limitations of the experimental test setup. It was observed that in the proximity of the first resonance frequency ($\approx$ 9 Hz), due to the large displacement of the beam tip, the vibration shaker may hit its maximum displacement stroke ($\pm$2.5 cm) and therefore the voltage on the piezoelectric patch may not be purely sinusoidal. In the event of a non- sinusoidal beam movement, the SSHI circuit's peak detector would fail to detect the peak voltage properly. Similarly, due to the same limitation (i.e. the shaker's maximum displacement stroke) movements of the beam may enter nonlinear regions which may further violate the linearity assumption of the Euler-Bernoulli beam theory.

The force sensor used to measure the magnitude of the excitation signal is a multi-purpose ICP sensor manufactured by PCB Piezotronics [99]. As can be seen in Figure 4.5, the vibration acceleration amplitude obtained from simulation matches well with the experimental results.

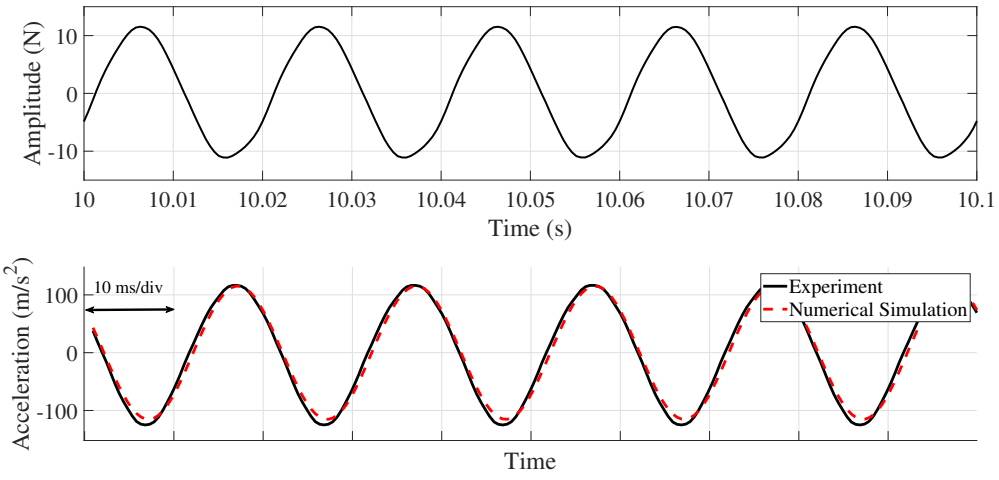


Figure 4.5: (Top) Harmonic tip excitation of the cantilever beam measured experimentally and, (bottom) comparison between simulation and experimental beam accelerations at $x \approx L_2$.

## 4.2 Results of the Experimental Studies

### 4.2.1 Standard Interfacing Circuit

The schematic of the experimental test setup with standard interfacing circuit is depicted in Figure 4.6. This is the simplest form of interfacing circuit in which the generated AC voltage is rectified through the diode bridge. The charging process initiates as soon as the toggle switch is closed, and the storage capacitor $C_s$ begins to accumulate the electric charge generated by the piezoelectric patch.

A comparison between the iterative numerical simulation and the experiment for the external capacitor charging curve is shown in Figure 4.7. Three different curves illustrate different charging curves resulting from various steady-state peak voltages across the piezoelectric material with different excitation amplitudes. Note that the only variable was the excitation amplitude and other parameters such as $C_s$ and

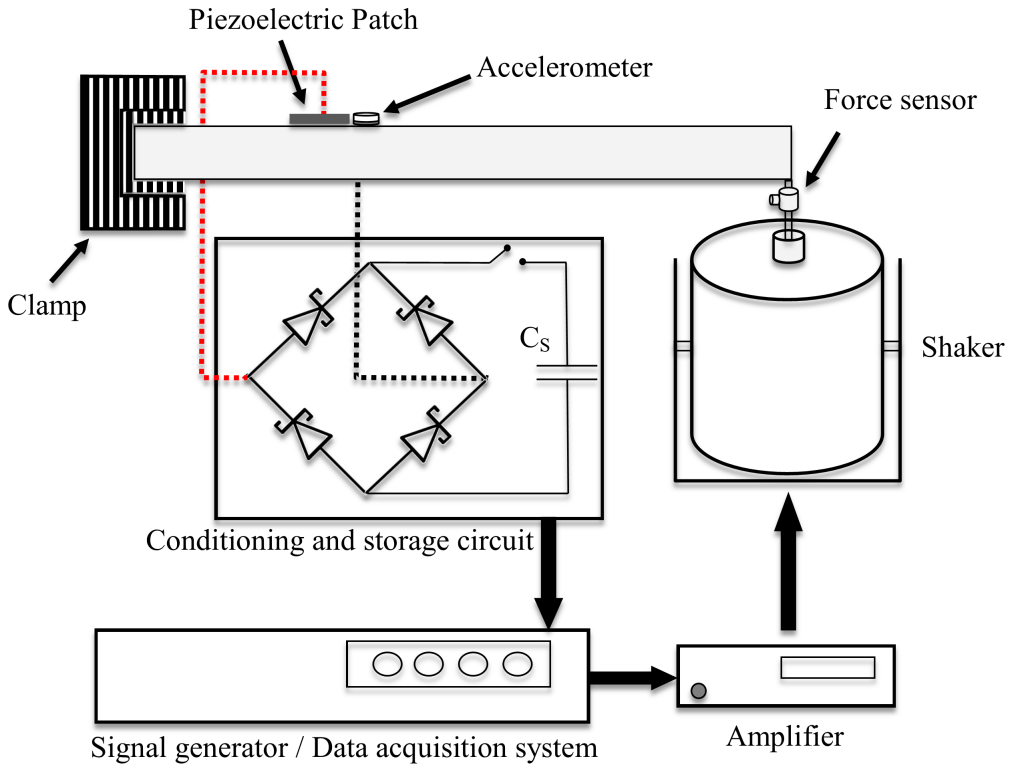


Figure 4.6: Schematic of the experimental test setup with standard interfacing circuit.

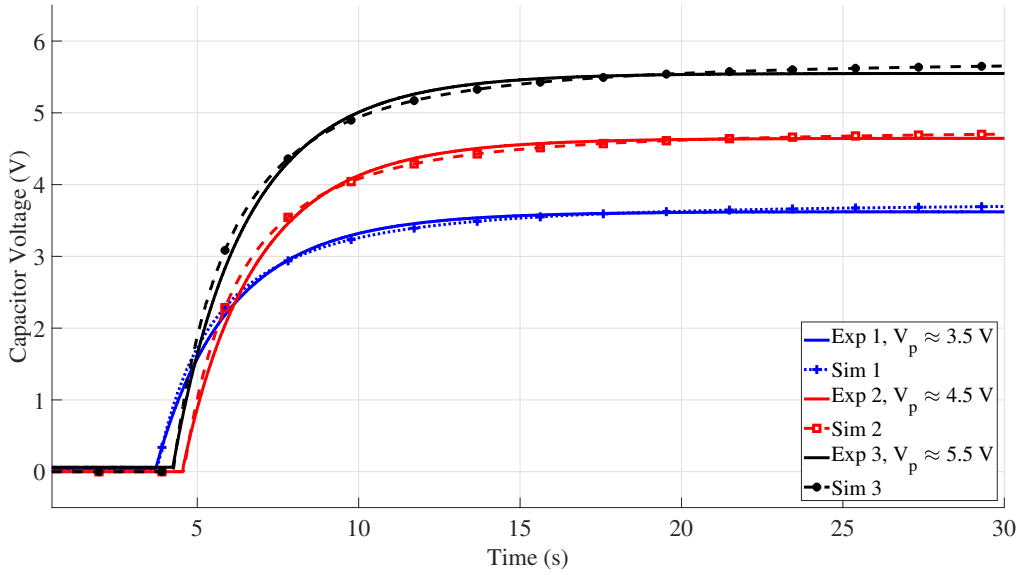


Figure 4.7: Capacitor charging curves with standard interfacing circuit for different excitation amplitude.

excitation frequency were kept constant in Figure 4.7 [$C_s = 10\,\mu F$, $C_v' = 5.5311\,nF$, $f = 50$ Hz, $L_p = 0.0325\,m$, $L_1 = 0.1277\,m$]. It is observed from Figure 4.7 that the voltage obtained from simulation is slightly higher than the experiment. This is in fact caused by errors in the measurement of the diode bridge input/output voltages. The voltage drop on the bridge circuit in the actual experiment is slightly higher than the one used in the simulation study, which causes the simulated capacitor voltage to be higher than the experimental one.

According to the modeling logic described in chapter 3, the removal of electric charge from the piezoelectric patch reduces the amount of voltage on the piezoelectric patch. This phenomenon is observed during experimentation and is shown in Figure 4.8. It can be seen that the initiation of the charging process at $T = 5$ seconds, reduces the voltage on the piezoelectric patch by $\approx 50\%$.

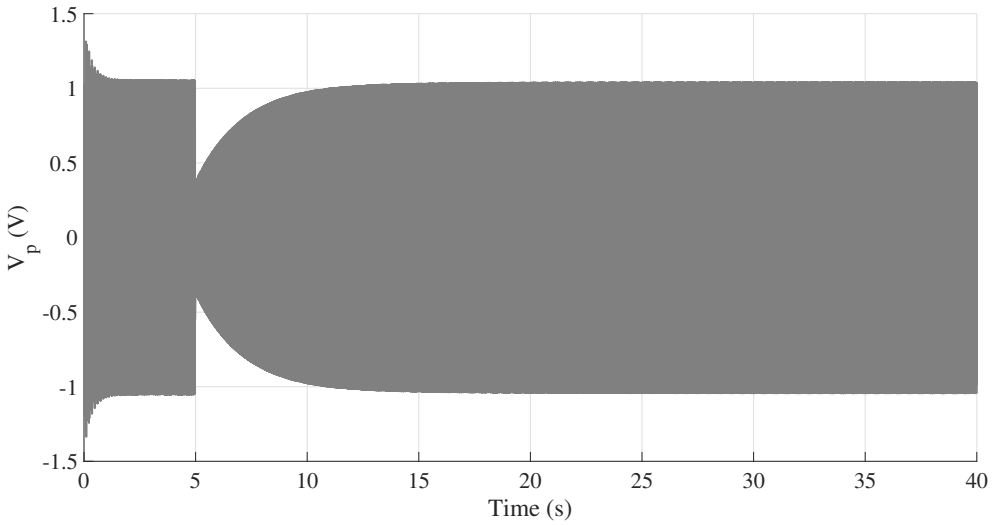


Figure 4.8: Experimentally observed voltage drop on piezoelectric material due to the initialization of the external capacitor charging at $T = 5$

Furthermore, the average power charging the storage capacitor during simulation is shown in Figure 4.9. Notice that the large peak of $1.049e^{-4}$ W at $T \approx 5.9$ second is logical, due to the assumption that $C_s$ is initially discharged. Right after the charging process begins, higher current flows towards the storage capacitor, and as the capacitor reaches the steady-state period after approximately 10 seconds, less power is transferred to $C_s$, and current reduces exponentially.

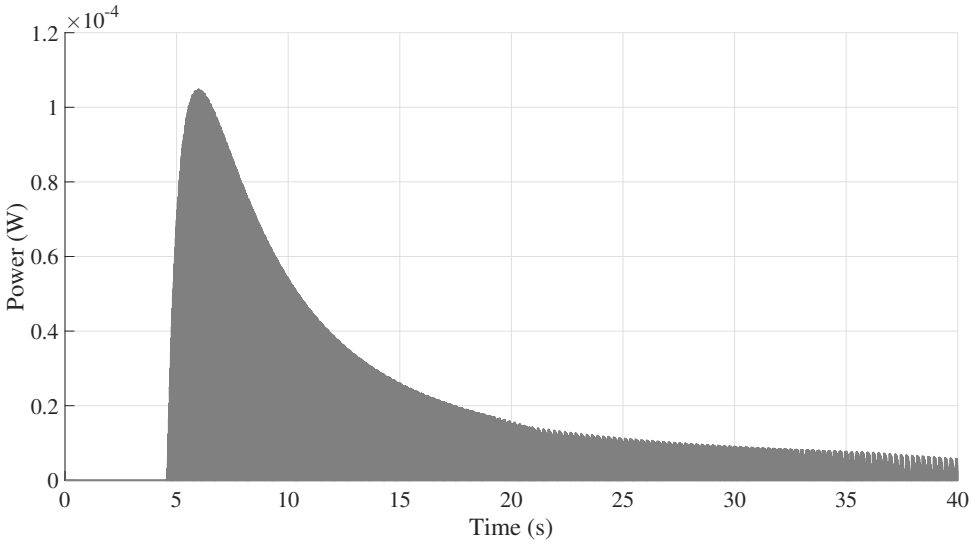


Figure 4.9: Average power charging the storage capacitor during simulation.

### 4.2.2 Self-powered SSHI Interfacing Circuit

The schematic of the PEH equipped with non-linear SSHI interfacing circuit is illustrated in Figure 4.10. The main difference between Figure 4.6 and Figure 4.10 is the inclusion of the electronic breaker circuit. The generated voltage on the piezoelectric patch, once connected to the circuit will be transformed to the shape depicted in the figure. The rest of the circuit is similar to the standard interfacing circuit. The rectification occurs using the diode bridge rectifier and then charges the storage capacitor.

Before comparing the transient charging behavior of this system, the experimental voltage obtained from the piezoelectric patch through SSHI interfacing, without any connection to the external capacitor, was compared against the numerical simulation results based on the modeling approach proposed in chapter 3. The cantilever beam was excited at 50 Hz (which lies between the first, and the second natural

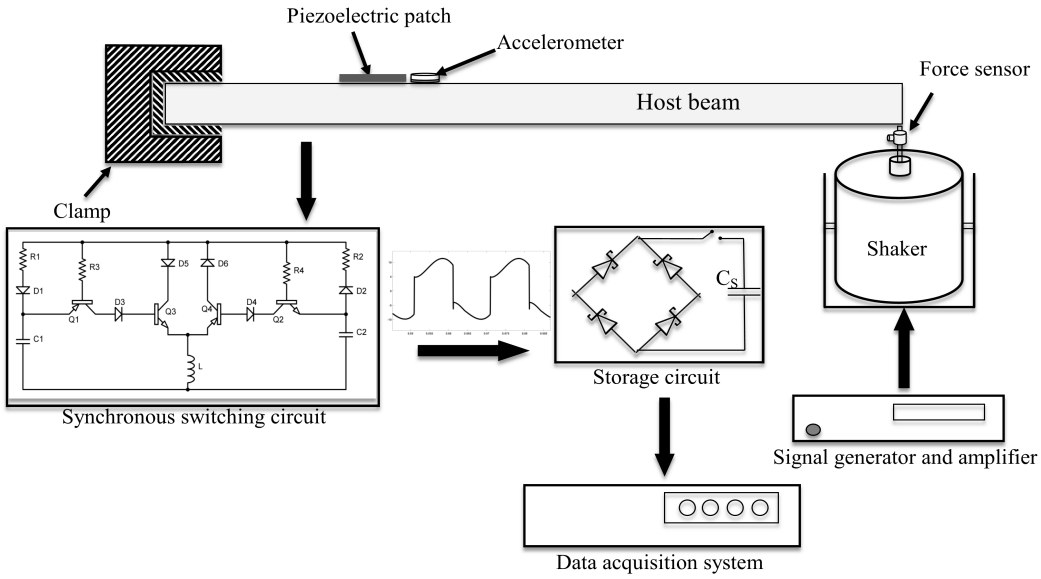


Figure 4.10: Schematic of the experimental test setup with parallel-SSHI Interfacing Circuit.

frequencies of the structure) with magnitude of approximately 10 N. As can be seen in Figure 4.11, the acceleration of the beam at the piezoelectric patch location from the numerical model is close to the obtained experimental data. The bottom plot of Figure 4.11 shows the voltage on the piezoelectric patch. The switching time delay ($\varphi$) away from the exact voltage peak locations caused by the operation of the electronic breaker can be clearly observed. In order to provide a better comparison, similar switching delay was incorporated into the numerical model based on the procedure described in section 3.3.3. It was seen that the simulated piezoelectric voltage is higher when compared with the experimental results. This is in fact due to a slightly overestimated conversion quality factor ($\lambda = 2.5$) of the SSHI circuit during simulation.

Once the validity of the model considering the self-powered SSHI but without external charging circuit is confirmed, the accuracy of the numerical method during

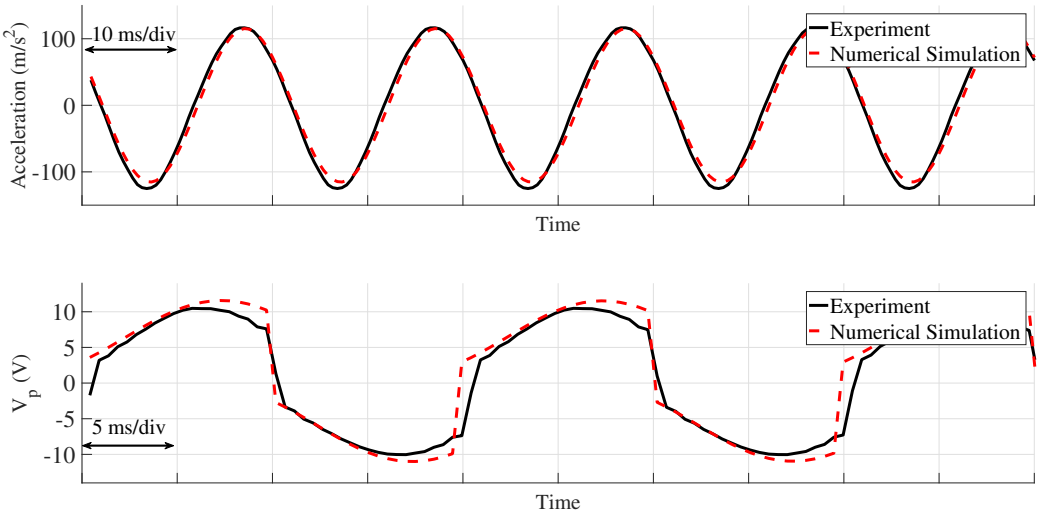


Figure 4.11: (Top) Simulated and experimental obtained beam acceleration at $x \approx L_2$ and, (bottom) piezoelectric patch voltage using SSHI interfacing circuit.

transient charging operation is investigated. Similar to the standard interfacing circuit, the voltage on the piezoelectric patch drops when connected to a purely capacitive load. This is depicted in Figure 4.12. As can be seen in the bottom plot of Figure 4.12, the iteration numerical model is well capable of simulating this voltage drop. Furthermore, the transient dynamics of the charging process of external capacitor for different piezoelectric voltage levels match well with the experimental data depicted in Figure 4.13 [$C_s = 10\,\mu F$, $C_v' = 5.5311\,nF$, $\Omega = 314.15$ rad/sec, $L_p = 0.0325\,m$, $L_1 = 0.1277\,m$]. It is believed that the small difference between the numerical and experimental charging curves is due to the non-linearity of the switching function, as well as the variability of the series resistance that certain electrical components, such as diodes, exhibit in the circuit. One can replace the approximated bi-linear series resistance explained in section 3.3.3 with a more accurate model to better represent such non-linearities.

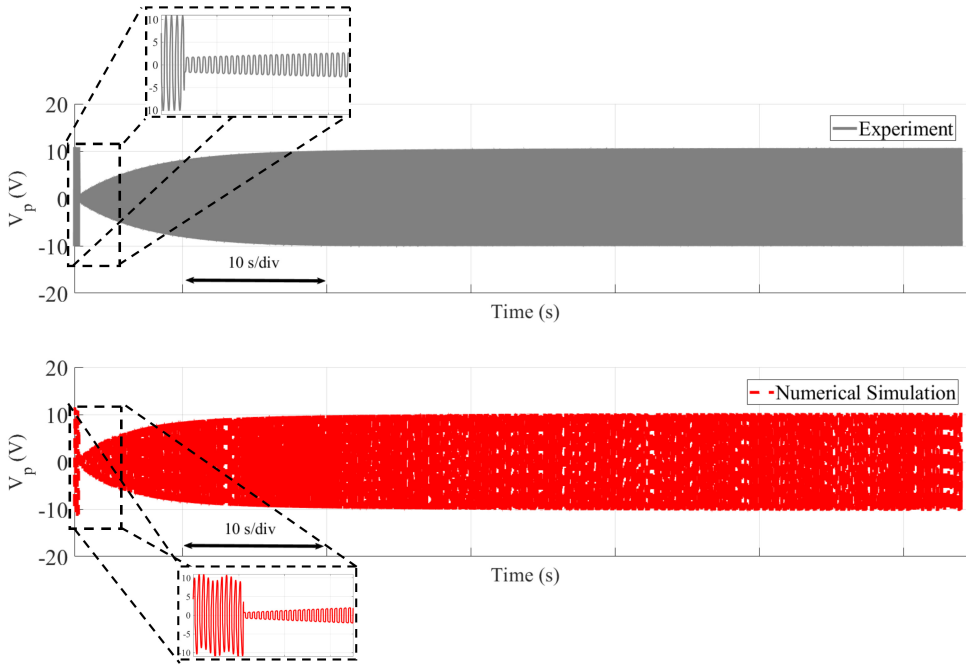


Figure 4.12: Experimental (top), and simulated (bottom) piezoelectric patch voltage drop after being connected to a purely capacitive load through SSHI interfacing circuit.

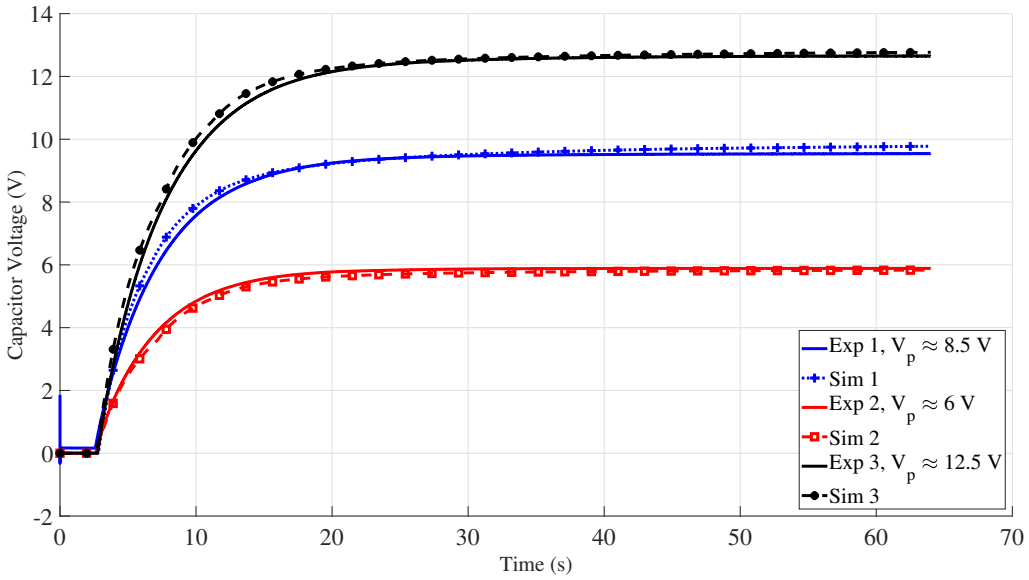


Figure 4.13: External capacitor charging curves for different excitation amplitude of the host beam ($f \approx 50$ Hz, $F \approx 8.5, 10, 12.5$ N).

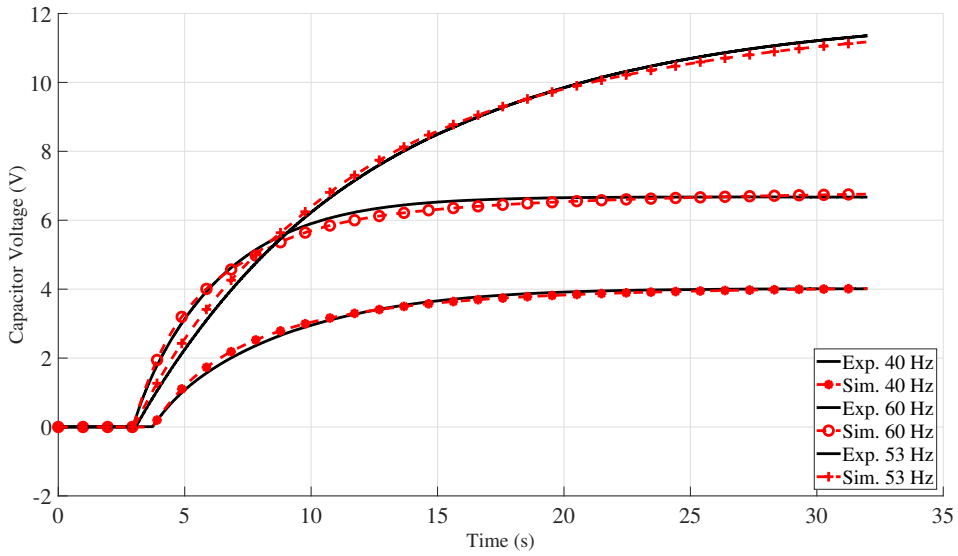


Figure 4.14: External capacitor charging curves for different vibration frequencies of the host structure.

It is also important to show that the model functions satisfactory, if the operating conditions of the system are to be changed. For instance, if the excitation frequency of the host structure changes, the vibration pattern, as well as the generated voltage on the piezoelectric patch will change, which will consequently change the transient behavior of the charging process. Figure 4.14 illustrates charging transient for different excitation frequencies with all other parameters unchanged [$C_s = 10\,\mu F$, $C_v' = 5.5311\,nF$, $F \approx 11$ N, $L_p = 0.0325\,m$, $L_1 = 0.1277\,m$]. These frequencies were intentionally selected to be higher (60 Hz), lower (40 Hz), and close to the second natural frequency (53 Hz) of the structure. The original test was performed at a frequency of 50 Hz (between the first and second modes of operation) and was shown in Figure 4.13.

From Figure 4.14 it is clearly noticed that both capacitor charging curves obtained from the numerical model agree with the experimental results. It can also be

seen that for similar excitation amplitude, higher vibration frequency (i.e. 60 Hz) resulted in higher stored voltage on the storage capacitor ($\approx$ 6.5 V for 60 Hz, as opposed to $\approx$ 4 V for 40 Hz). Note that operating the system in the vicinity of the natural frequency with high excitation amplitude could potentially damage the mechanical structure, the vibration shaker, or the piezoelectric patch. The purpose of operating the system at 53 Hz (very close to resonance frequency of $\approx$ 55 Hz) was to demonstrate the range of higher electrical power that can be obtained from this system under current operating condition.

Finally, to provide a comparison between standard interfacing circuit and non-linear SSHI circuit during transient charging, an experiment was performed where all parameters were kept constant [$C_s = 10\,\mu F$, $C_v' = 5.5311\,nF$, $\Omega = 314.15$ rad/sec, $L_p = 0.0325\,m$, $L_1 = 0.1277\,m$], with the only difference of adding non-linear processing of the voltage through the self-powered SSHI circuit. Obtained results depicted in Figure 4.15 shows the advantage of using non-linear processing during charging process. It can be seen that the self-powered SSHI circuit resulted in a peak voltage of $\approx$ 10 V on the piezoelectric patch, whereas the standard interfacing circuit resulted in $\approx$ 5.2 V.

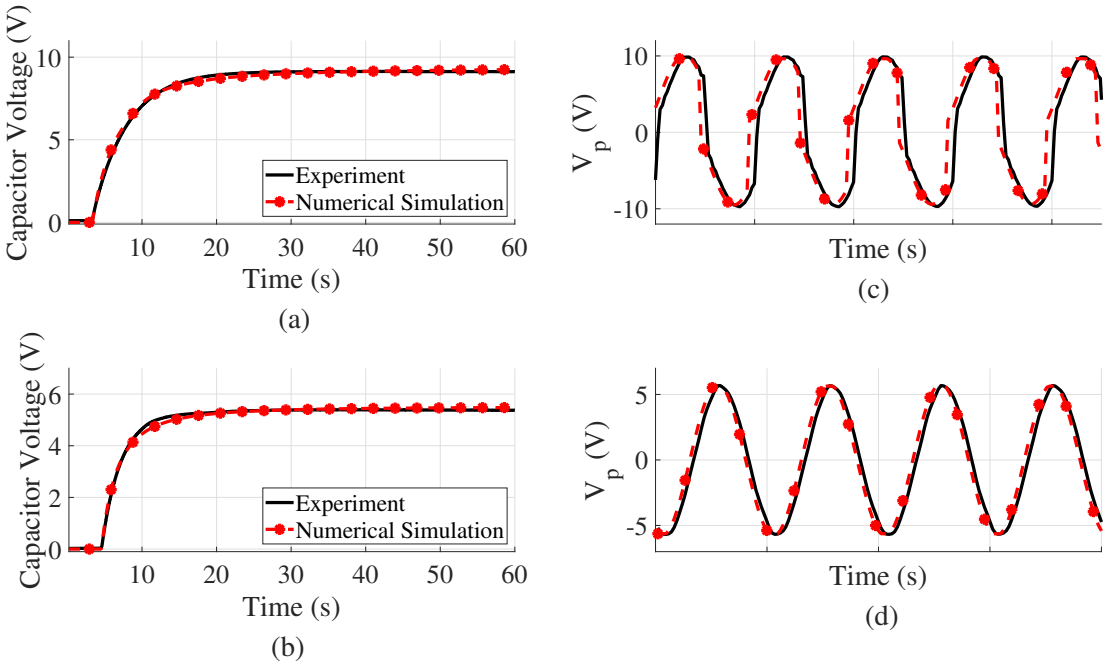


Figure 4.15: (a)-(b) Experimental and simulated transient charging behavior and, (c)-(d) voltage on piezoelectric patches using (top) SSHI and (bottom) standard interfacing circuits after $C_s$ is charged.

## 4.3 Results of the Parametric Studies

One of the advantages of a robust and reliable simulation model of the PEH, is that it provides an efficient tool for the designer to optimize system parameters and maximize power harvesting efficiency. The experimental studies performed in the previous section proved the accuracy of the semi-theoretical model in predicting the transient charging dynamics of the PEH. It is now straightforward to study how variations in different system parameters impact the energy harvesting efficiency. This section summarizes the results of the performed parametric studies. Particularly, the focus is on energy harvesting and storage efficiency considering the power output during the transient capacitor charging when non-linear electronic interfacing is employed. All simulations are carried out in MATLAB® . In essence, this section lays the groundwork for the optimization of the PEH that will be discussed in chapter 5.

It should also be mentioned that an explicit definition of power and efficiency is needed to better interpret the result of the following parametric studies. In other words, a quantifiable performance measure is needed to distinguish between high efficiency energy harvester, the one that generates more electrical power for less amount of mechanical vibration, and low efficiency.

In this context, *efficiency* of the power harvesting system is defined as the ratio of the Root Mean Square (RMS) of the harvested electric power ($P_e$), to the RMS of the input mechanical power ($P_m$), $Eff = \frac{P_e^{RMS}}{P_m^{RMS}}$. Note that the mechanical power definition for the system undergoing harmonic base-motion is different from the system undergoing point-force vibration. Equation (4.1) represents the mechanical,

and electrical powers:

$$P_e^{RMS} = \sqrt{\frac{1}{T}\int_0^T \Big(\frac{\frac{1}{2}[C_s(V_{s,i}^2 - V_{s,i-1}^2)]}{\Delta t}\Big)dt}$$

$$P_m^{RMS} = \sqrt{\frac{1}{T}\int_0^T [F\sin(\Omega t)\delta(x-L)\frac{dW_n(L)}{dt}]dt}; \qquad \text{Point-Force} \tag{4.1}$$

$$P_m^{RMS} = \sqrt{\frac{1}{T}\int_0^T [\rho A Y^2 \Omega^3 2\sin(\Omega t)\cos(\Omega t)]dt}; \qquad \text{Base-Excitation}$$

where $P_e^{RMS}$ is the RMS of the potential power stored on the storage capacitor obtained from the average power charging the storage capacitor through the parallel-SSHI circuit, and, $P_m^{RMS}$ represents the RMS of the mechanical power. Note that throughout the simulation, the integration period $T$ was selected so that the external capacitor $C_s$ was at least 90% charged.

Parametric studies performed in this section are based on the assumption that the beam is under harmonic tip excitation (point-force). That is to provide consistency with the experimental results provided in section 4.2. In chapter 5 however, both operating conditions (i.e. point-force and harmonic base motion) are considered during the optimization process.

### 4.3.1 Capacitor Charging Through Standard Circuit

Figure 4.16 (a) and (b) show the effect of variations in the excitation frequency on the mechanical and electrical powers, and the efficiency of the power harvesting

system, respectively [$C_v' = 5.5311\,nF$, $L_p = 0.0325\,m$, $L_1 = 0.1277\,m$]. One can notice two peaks at frequency $\approx 10$ and 56 Hz shown in Figure 4.16 (b). Frequency varies between $4 - 70$ Hz which covers the first and second natural frequencies of the tested beam. From Figure 4.4, one can observe that these frequencies are close to the first two natural frequencies of the piezoelectric-coated beam. Reasonably, exciting the system around the natural frequency will cause the system to resonate, producing more electrical, as well as mechanical power. Looking at the efficiency results, it is noted that the energy harvesting efficiency is higher at the first resonance (0.0147) compared with the peak corresponding to second resonance ($1.719e^{-4}$). The second peak at 56 Hz is orders of magnitude smaller than the first peak, indicating harsher movements of the beam at the excitation frequency of $\approx 10$ Hz. With same displacement at the loading point, due to the larger curvature distributed at the piezoelectric patch location at the first vibration mode, the electrical power output increases more dramatically at the first resonance.

Changing the size of the external capacitor $C_s$ will also affect the electrical power generation and the overall energy harvesting efficiency. Figure 4.16 (c) and (d) illustrate this effect. The capacitor size was varied from 6 to $18\,\mu F$. Results indicate that the output electrical power increases with higher capacitance up to a certain point. The relatively rapid increase in the electrical power observed in Figure 4.16(c), (from $7.798e^{-6}$ for $C_S = 6\,\mu F$ to approximately $7.896e^{-6}$ for $C_S = 12\,\mu F$) becomes more gradual for $C_S \geq 12\,\mu F$. The small slope observed in Figure 4.16(c) for $16 \leq C_S \leq 18\,\mu F$ shows that increasing the capacitance of the external capacitor any further does not have a significant impact on the obtained RMS of the electrical power.

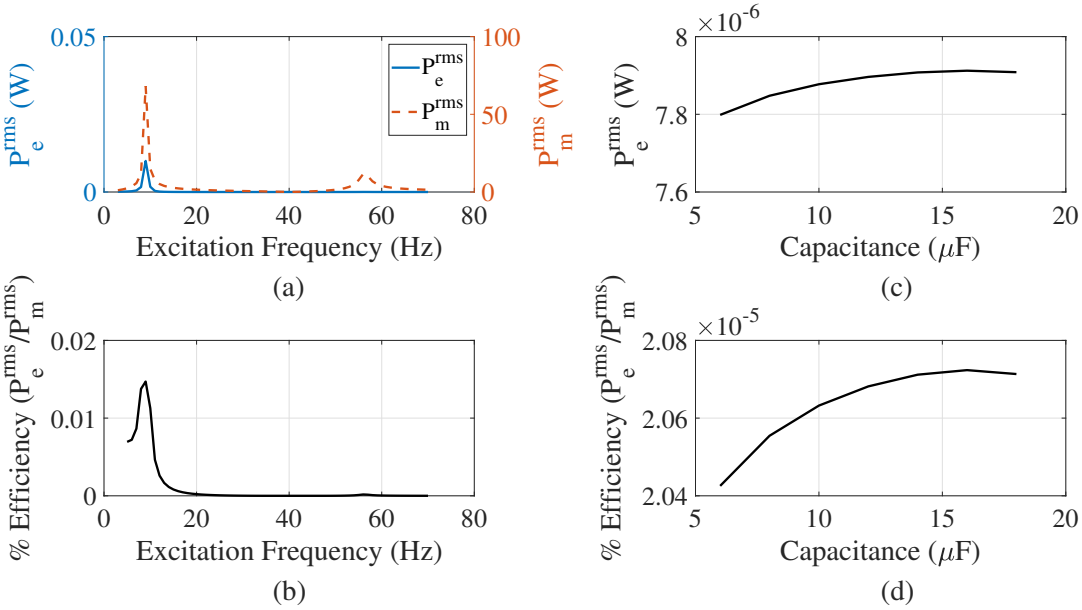


Figure 4.16: (a)-(b) Effect of varying excitation frequency, and (c)-(d) external capacitor size ($C_S$), on energy harvesting efficiency and the RMS of the power (constants: $C_0 = 5.5311\,\mu F$, $L_p = 0.0325\,m$, $L_1 = 0.1277\,m$)

Furthermore, Figure 4.17 (a) and (b) show the simulated capacitor charging curves and the average power charging the storage capacitor for different $C_s$ sizes, respectively. Notice that the higher the capacitance, the lower the charging slope. Therefore, the capacitor takes longer to charge. With a small capacitance ($5\,\mu F$), the charged voltage and power charging the capacitor increase significantly at the first 0.5 second into the charging process, from 0 to 1.16 V, and 0 to $3.274e^{-5}$ W at $T = 4.45$ second, respectively. However, after 2 second of charging, the charged voltage increment becomes very slow leading to a dramatically reduced electrical power from $T = 5$ second to $T = 6$ second and low power value for the rest of the charging time. On the other hand, for a large capacitance ($16\,\mu F$), the voltage keeps increasing from $T = 4$ second to $T = 20$ second smoothly, indicating that the

charging takes place for a longer period, compared with the small capacitance case with higher RMS value of the electrical power of the charging operation period of the harvester.

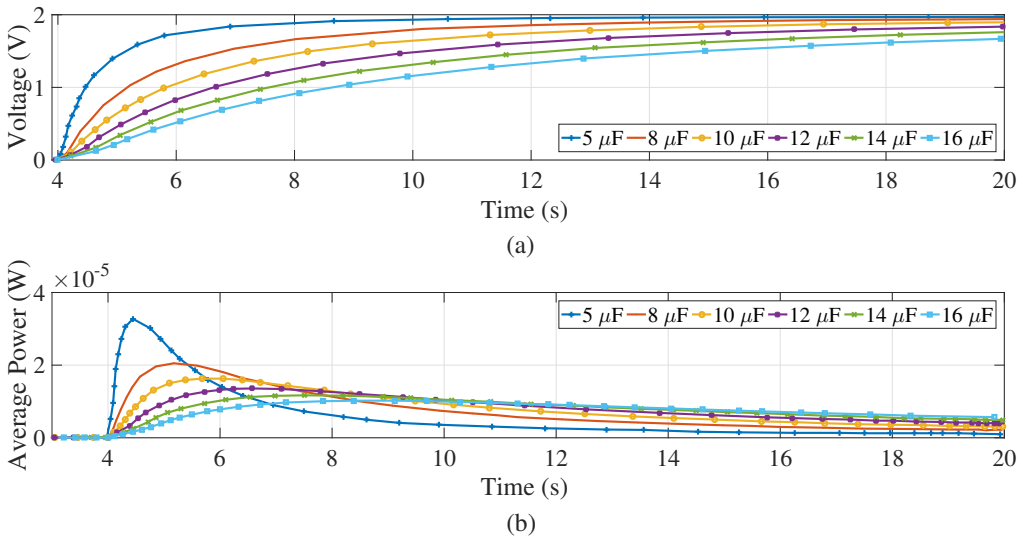


Figure 4.17: Variations of the capacitor charging curve (a) and the average power charging the external capacitor for varying $C_S$ (constants: $C_v' = 5.5311\,nF$, $L_p = 0.0325\,m$, $L_1 = 0.1277\,m$)

Additionally, the effect of using conventional PN junction diodes (red) on the charging curve was simulated and compared with the case of using Schottky diodes. As can be seen in Figure 4.18, the higher forward voltage drop of the PN junction diodes causes the $C_s$ steady-state voltage to be lower compared to the case of the Schottly diodes. Information obtained from this parametric study can help in the design of the interfacing circuit for better overall system efficiency.

An important criteria in the design of an energy harvesting system is the length and location of the piezoelectric patch on the host structure. Although such parameters are mostly application dependent, a general idea on how these parameters affect the energy harvesting efficiency is very useful, particularly to system designers.

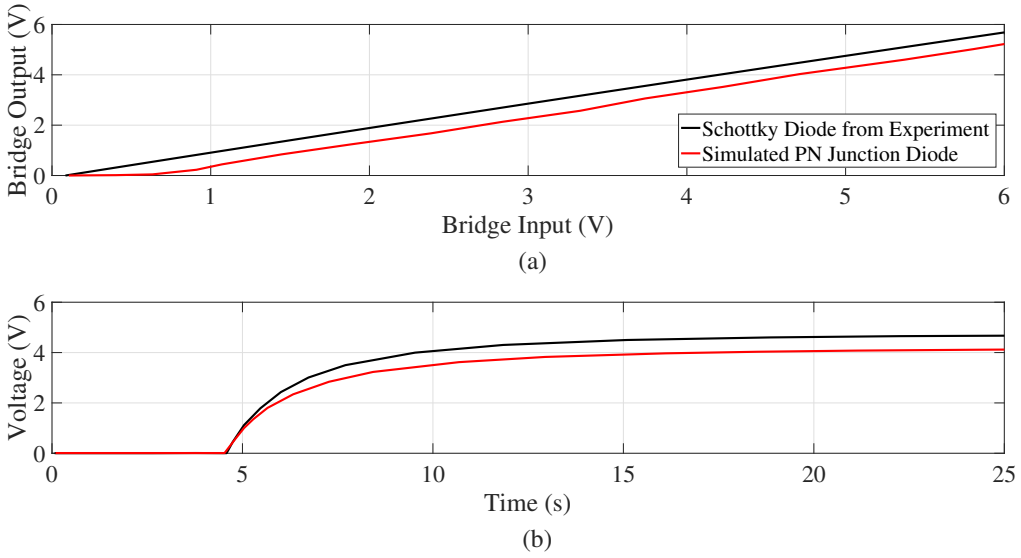


Figure 4.18: (a) Input/output diode bridge voltage based on experimentally measured Schottky diodes (black), and simulated conventional PN junction diodes (red), and the corresponding charging curves (b)

Therefore, variations of piezoelectric patch length and location on the host beam are also studied. As can be seen in Figure 4.19(a) and Figure 4.19(b), increasing the piezoelectric patch length will increase the efficiency only upto a certain point. As can be seen from Figure 4.19 (b), maximum power harvesting efficiency (0.04659) was obtained for patch length of 22 cm. Increasing the patch size any further will in fact have a negative effect on efficiency. Although the maximum electrical power was obtained for the patch length of 14 cm, the maximum energy harvesting efficiency was obtained for $L_1 = 22$ cm. The reason is that beyond the patch length of 14 cm, the mechanical power of the system reduced drastically, leading to the higher overall energy harvesting efficiency. In other words, less mechanical power was consumed for relatively same amount of electrical power. Similar observation is made from Figure 4.19(c) and Figure 4.19(d). Moving the piezoelectric patch from the fixed-end

towards the tip of the beam will increase the obtained electrical power only upto $\approx 30$ cm from the fixed-end.

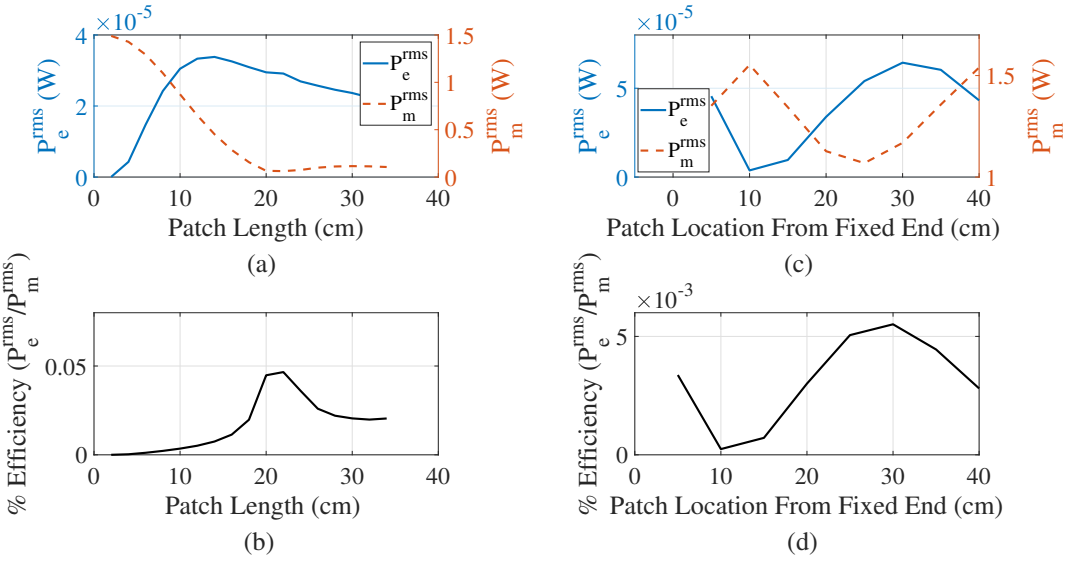


Figure 4.19: (a)-(b) Effect of varying piezoelectric patch length ($L_p$), (c)-(d) and location ($L_1$) on energy harvesting efficiency based on the RMS of the power (constants: $frequency = 50$, $C_s = 10\,\mu F$, $C_v' = 5.5311\,nF$)

### 4.3.2 Capacitor Charging Through Self-powered Parallel-SSHI Circuit

Similar to the standard interfacing case study described in the previous sub-section, in this section, the effects of varying external excitation frequency ($\Omega$), and size of the external capacitor ($C_s$), are considered for the SSHI interfacing circuit. Once again, excitation frequency is varied between $4 - 70$ Hz, and $C_s$ increases from $6 - 18\,\mu F$. All other system parameters are constant during this study: $C_v' = 5.5311\,nF$, $F \approx 11$ N, $L_p = 0.0325\,m$, $L_1 = 0.1277\,m$.

Figure 4.20 (a) shows the RMSs of both electrical and mechanical powers for

variable $\Omega$ when SSHI interfacing is employed. Two large peaks at $f \approx 10$ and 56 Hz are noticed which corresponds to the first two natural frequencies of the beam. It is clear that the peak due to first resonance is much larger than the second peak. The efficiency of the energy harvesting in case of varying frequency with/without SSHI circuit is depicted in Figure 4.20 (b). It can be seen that SSHI interfacing results in higher efficiency than the standard circuit. Power variations due to changes in $C_s$ is shown in Figure 4.20 (c). It is clear that the mechanical power is not affected by the size of the external storage device, however, the electrical power, as well as the power harvesting efficiency (d) are initially increased (for $C_s \leq 16\,\mu F$) and then reduced for $C_s \geq 16\,\mu F$. Once again, note that when utilizing non-linear electrical charging processing with SSHI circuit, the efficiency depicted in Figure 4.20 (d) was approximately double of the standard circuit efficiency.

Figure 4.21 (a)-(c) shows the effect of varying patch length and location from the fixed-end of the structure on the RMS power output charging the external capacitor. Piezoelectric patch length is varied from 2 cm to approximately 35 cm in order to cover more than half of the top surface area of the beam. An increasing trend in the RMS of the electrical power is observed in Figure 4.21 (a) for $L_p \leq 15$ cm, with the maximum obtained for $L_p = 14$ cm. Increasing the length beyond that point led to a decrease in the obtained electrical power. In order to verify the result obtained from this parametric study, an experimental test was performed with the cantilever beam coated with a variable number of piezoelectric patches. Figure 4.22 depicts the test setup with the modified cantilever beam after the final experiment with five piezoelectric patches glued, and perfectly bonded on the beam. Initially, the beam was coated with only three piezoelectric patches (patch length of 5 cm with

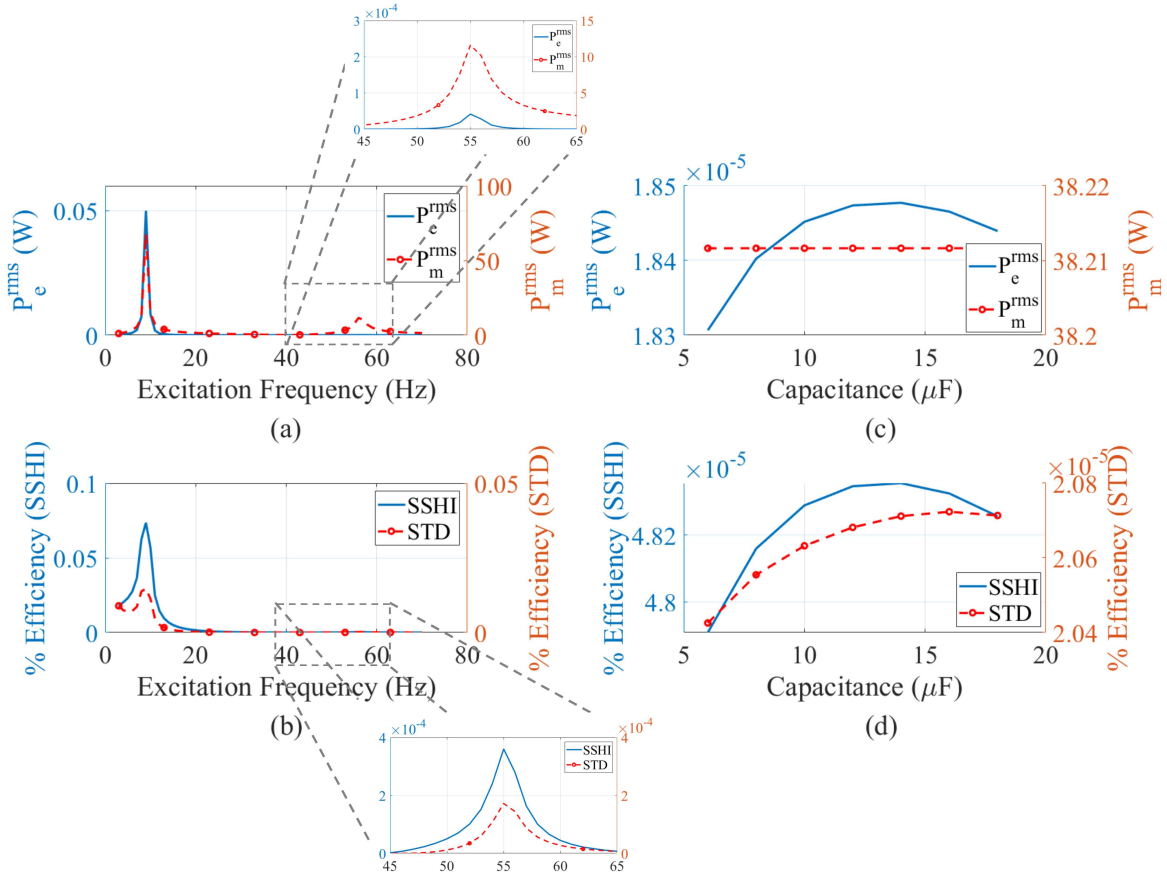


Figure 4.20: (a)-(b) Effect of varying excitation frequency, and (c)-(d) external capacitor size ($C_s$), and, comparison of the efficiency of energy harvesting system during charging process with/without SSHI interfacing circuit(constants: $C_v' = 5.5311\ \mu F$, $L_p = 0.0325m$, $L_1 = 0.1277m$).

$L_1 = 0.1277$ m) and was harmonically excited at 50 Hz with the magnitude of $\approx 1.2$ N. This test resulted in 3.15 V on piezoelectric patches. Furthermore, two additional experiments were performed with four and five piezoelectric patches with the same excitation amplitude and frequency, which led to the same voltage measurement of approximately 2.9 V. Therefore, using five piezoelectric patches with the combined piezoelectric layer length of 25 cm reduced the generated voltage by 8 percent, when compared with the experiments performed with three piezoelectric patches.

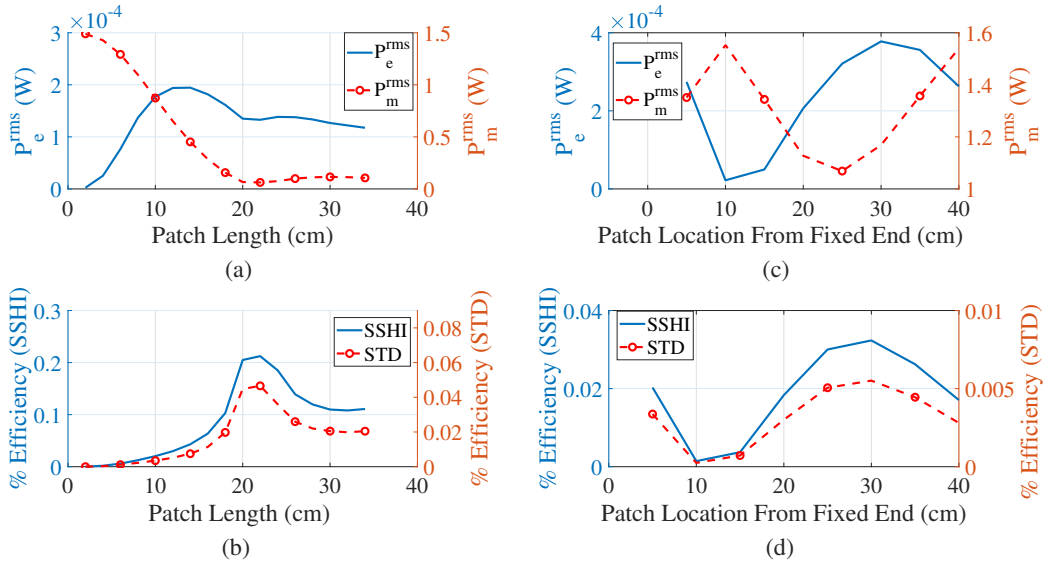


Figure 4.21: (a)-(b) Effect of varying piezoelectric patch length ($L_p$), and (c)-(d) location ($L_1$), and, comparison of the efficiency of energy harvesting system during the charging process with/without SSHI interfacing circuit (constants: $f = 50$, $C_s = 10\ \mu F$, $C_v' = 5.5311$ nF)

The main reason is that since the frequency of excitation is selected to be close to the second vibration mode of the beam, when the piezoelectric layer covers a relatively large beam surface area with positive and negative curvature distributions, electric charge on the piezoelectric patch could potentially cancel out, leading to a lower voltage and a reduction in the electrical power obtained from the harvester.

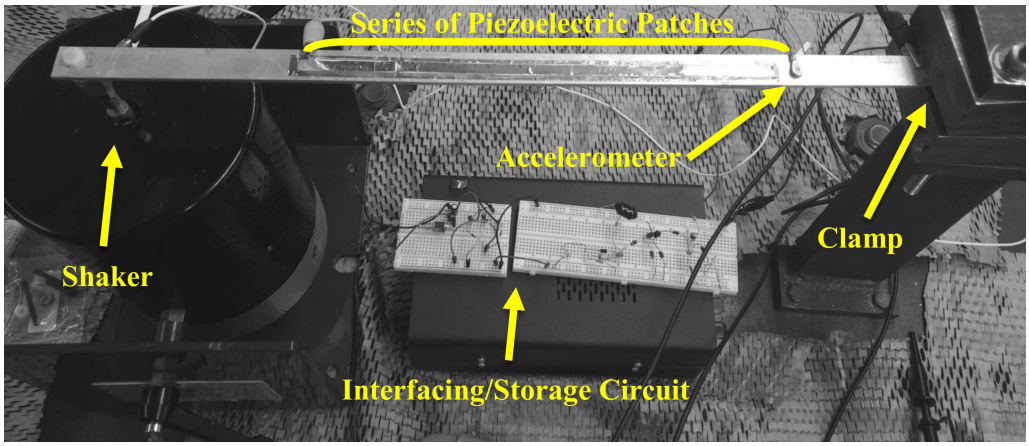


Figure 4.22: Experimental test setup with the modified cantilever beam.

Additionally, a larger piezoelectric layer leads to higher piezoelectric capacitance, which is another contributing factor to the lower voltage obtained on the piezoelectric patch.

A comparison between energy harvesting efficiency with/without SSHI circuit (Figure 4.21 (b)) for different piezoelectric patch length shows that the SSHI circuit provides a much better performance as compared to standard circuit for all different designs of the harvester. For the case of changes in patch location, a decreasing trend, followed by an increase in both the harvested power, and efficiency is observed in Figure 4.21 (c)-(d). Once again, introducing the SSHI circuit results in a higher efficiency of harvested power.

It was mentioned earlier that the overall performance of the SSHI circuit is, among other factors, dependent on the conversion quality factor $\lambda$, and the switching time delay $\varphi$ of the electronic breaker circuit. Therefore, a parametric study where only these parameters are changed is performed and the results are illustrated in Figure 4.23 (constants: $C_s = 10\,\mu F$, $C_v' = 5.5311\,nF$, $F \approx 11$ N, $L_p = 0.0325\,m$,

$L_1 = 0.1277\,m$, $f = 50$ Hz). It should be mentioned that switching time delay is simulated by triggering the voltage conversion command certain number of data points after the peak detection flag is up of the voltage on the piezoelectric patch. Since $\lambda$ and $\varphi$ are both parameters of the interfacing circuit, it is expected that the mechanical power does not change significantly. This is in fact observed in Figure 4.23 (a) and (c).

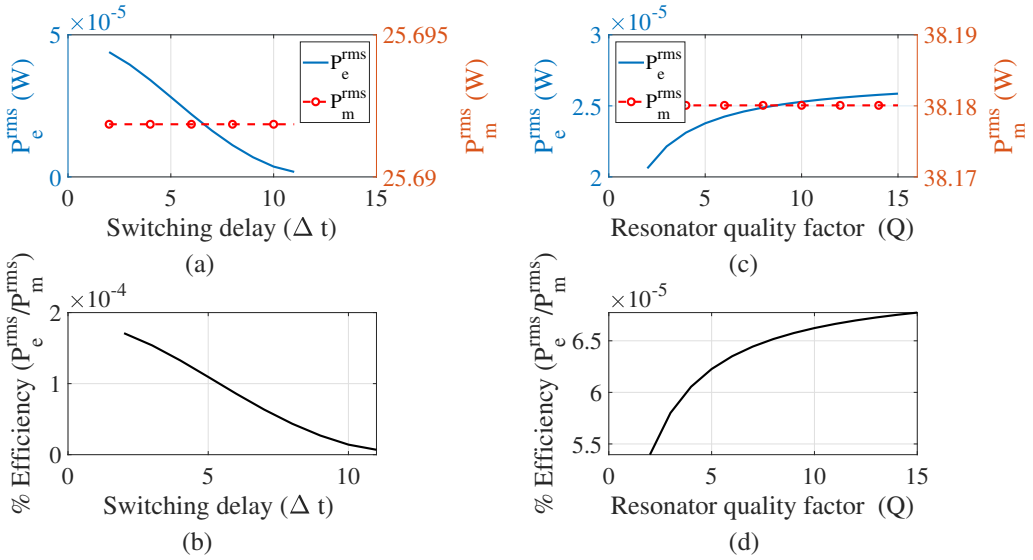


Figure 4.23: (a)-(b) Effect of switching delay in the electronic breaker voltage inversion ($\phi$), and (c)-(d) resonator quality factor ($\lambda$) on energy harvesting efficiency based on RMS of the power (constants: $f = 50$, $C_s = 10\ \mu F$, $C_v' = 5.5311$ nF, $L_p = 0.0325m$, $L_1 = 0.1277m$)

Nonetheless, the electrical power and efficiency are impacted drastically. For the case of changes in switching delay, the electrical power is reduced almost linearly as the delay increases. This in turn causes a constant decrease in the energy harvesting efficiency (Figure 4.23 (b)). Increasing the resonator quality factor $\lambda$ from 2 to 15 increases the harvested electrical power, and consequently, the power harvesting efficiency, exponentially.

## 4.4 Summary and Chapter Conclusions

In this chapter, an experimental test setup was developed based of a piezoelectric-coated cantilever beam, equipped with two different types of interfacing circuits (i.e. standard interfacing and non-linear synchronous switching circuit) and a storage capacitor. The behavior of the system during transient operation of charging the storage capacitor was comprehensively studied. The efficacy and accuracy of the iterative numerical model developed in chapter 3 was first investigated using the experimental test setup. Once the numerical model was validated, several parametric studies were performed to study system's behavior under variations of different system parameters. More precisely, the effect of excitation frequency of the host structure, the size of the storage capacitor, the length and location of the piezoelectric material, and parameters of the interfacing circuit were examined. According to the observations during experimentation and based on the results discussed in this chapter, following concluding remarks can be made:

- Performed experimental tests verified the functionality of the model proposed in chapter 3 and revealed that this numerical procedure is capable of simulating a complete energy harvesting system, comprised of piezoelectric patch, standard and non-linear interfacing circuits, and storage capacitor.

- Based on the performed parametric studies, it was shown that the utilization of non-linear processing through self-powered SSHI circuit can significantly enhance the efficiency of harvested power during the charging process. However, proper selection of circuit parameters has an impact on the overall performance of the system. Particularly, when electronic breaker is used to implement the

self-powered SSHI, increasing the quality factor while reducing the switching time delay positively affect the energy harvesting efficiency.

- It was also observed that the size of the storage capacitor, the length, and the location of the piezoelectric material have significant impacts on the efficiency of the energy harvesting system, and should therefore be optimally selected to enhance the overall power harvesting efficiency.

It can therefore be concluded that an accurate description of the PEH can be advantageous in the optimal design problems of practical energy harvesting systems.

# Chapter 5

# Simulation-Based Optimization of PEH

*"I have called this principle, by which each slight variation, if useful, is preserved, by the term of Natural Selection."*

from "On the Origins of Species" (1859) - Charles Darwin

This chapter addresses the simulation-based optimization of a PEH with a cantilever beam coated with piezoelectric patches, equipped with synchronous switching circuit. The objective is to find optimal positioning and size of the piezoelectric patch, the substrate cantilever beam, and the size of the storage capacitor that leads to higher efficiency of the power harvesting system. The semi-theoretical model that was fully explained in chapter 3 and experimentally validated in chapter 4 is the basis of the optimization scheme proposed in this chapter. An overview of the optimization flowchart proposed in this chapter is illustrated in Figure 5.1. Details

on each block of this flowchart will be fully described in this chapter. More precisely, section 5.1 outlines the basic concepts of Artificial Neural Network (ANN) and presents the architecture of the Neural Network (NN) model used in this thesis. Section 5.2 introduces the optimization scheme based on the GA optimization. The concept of GA optimization is explained using a benchmark function as an example. Section 5.3 describes the process of defining the PEH optimal design as an optimization problem which can be tackled using machine learning algorithms. Section 5.4 presents a complete analysis of the optimization results, quantifying the quality and performance of the ANN training using statistical measures. Finally, section 5.5 summarizes the chapter.

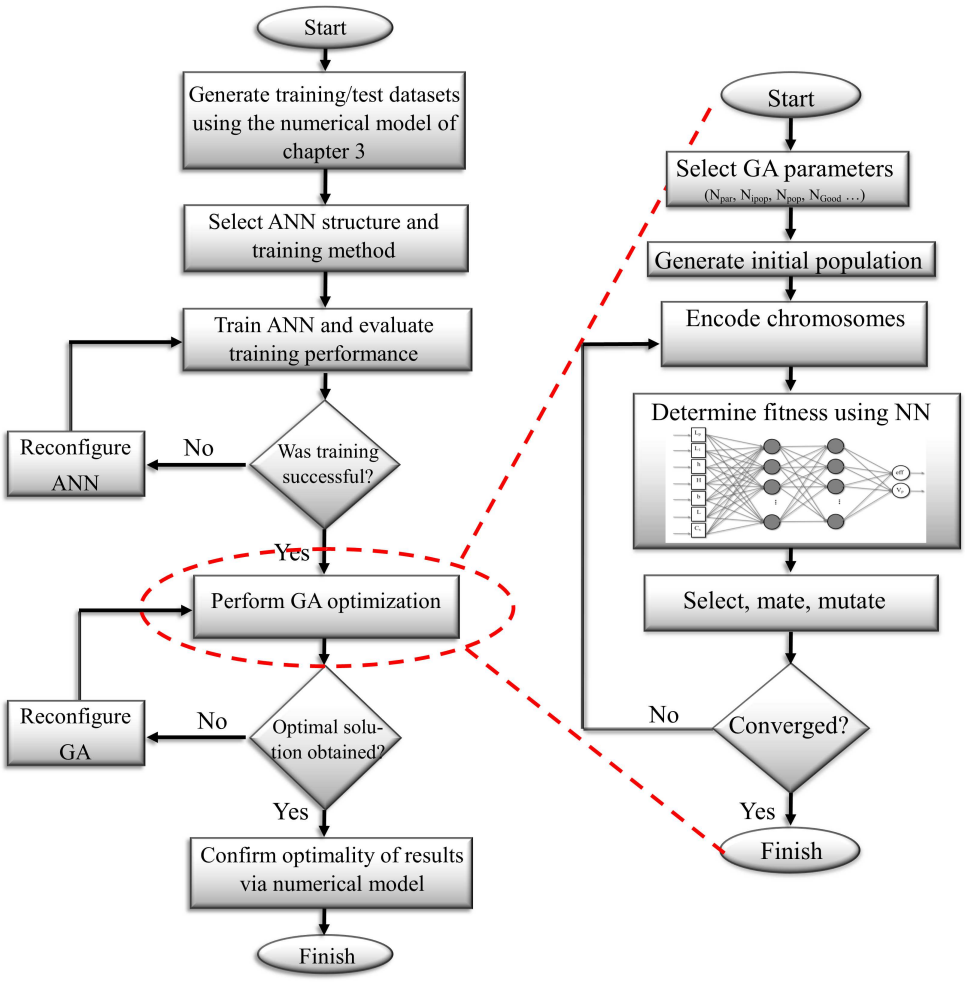


Figure 5.1: Flowchart of the proposed optimization procedure.

## 5.1 Artificial Neural Networks (ANN)

The numerical modeling procedure explained in chapter 3 and experimentally validated in chapter 4 is able to capture the underlying complex behavior of a PEH considering the transient charging process of an external storage device through a non-linear electronic interfacing circuit. However, the model lacks the computational efficiency required for multivariate optimization algorithms. For instance, calculation

of the dynamic displacement function $w(x,t)$ (equation (3.3) of section 3.1) for each beam section at every iteration of the simulation program requires large number of loop calculations. Simultaneously, to guarantee the convergence of the simulation and to provide numerical stability, relatively small (in the order of 0.001 s) time steps $\Delta t$ should be chosen. Therefore, the main drawback of using such accurate representation of the system is the required memory and processing power which might be beyond the capability of the everyday personal computers.

As an example, a typical transient charging simulation of the capacitor charging progress for 50 seconds performed in a personal computer equipped with an Intel® Core-i5-4570 processor [101] and 8 Giga Bytes of RAM, takes approximately 15 minutes. Considering that most optimization algorithms require multiple evaluation of the OF, the growing number of simulation time, as well as the growing memory requirements to store large data structures make it impractical to use the numerical iteration process during system optimization. The solution proposed in this thesis to overcome such complexities is to use a properly trained ANN instead of the expensive-to-evaluate numerical simulation model during the optimization procedure. Since the concept of NN might be unfamiliar to some readers, a brief introduction of NN is provided in the following sub-section.

### 5.1.1 Basic Concepts

ANNs or NNs [1] for short, are nature-inspired computer algorithms with a broad range of applications in many areas of science and engineering. NNs are extensively used for various machine learning problems includeing: function approximation,

[1] The acronyms ANN and NN are used interchangeably throughout this thesis.

regression, and classification predictive modeling [102]. The widespread use of NNs is the result of highly desirable properties of these computing networks, including, but not limited to parallel distributed structure, generalization (i.e. the ability to learn), non-linearity, adaptability [103]. The three main elements of an NN are as follows [104]:

- Neurons (also called nodes) - These are the processing elements of an NN;
- Connection topology - The way different Neurons are connected within the network;
- Learning algorithm - The way the network is trained to perform inference, as opposed to following a certain number of direct instructions.

Needless to say that appropriate selection of these three elements is application dependent and has potentially significant impacts on the performance of the network. The visual description of a generic ANN is depicted in Figure 5.2.

In Figure 5.2, the unit input signals ($x_{1,\dots,n}$) can either be external signals (from environment etc.), or, from another processing element or neuron. $\mathcal{W}_{n,j}$ represents the weight of the input signal $n$ to the neuron $j$ ($\mathcal{W}$ should not be confused with $W_{1,2,3}$ discussed in chapter 3 that represented the mode shapes of the beam). Mathematically speaking, the output signal of the $j$'th node ($y_j$) can be calculated as [103]:

$$y_j = g(\sum_{i=1}^{n} x_i \mathcal{W}_{i,j} - \theta_j) \tag{5.1}$$

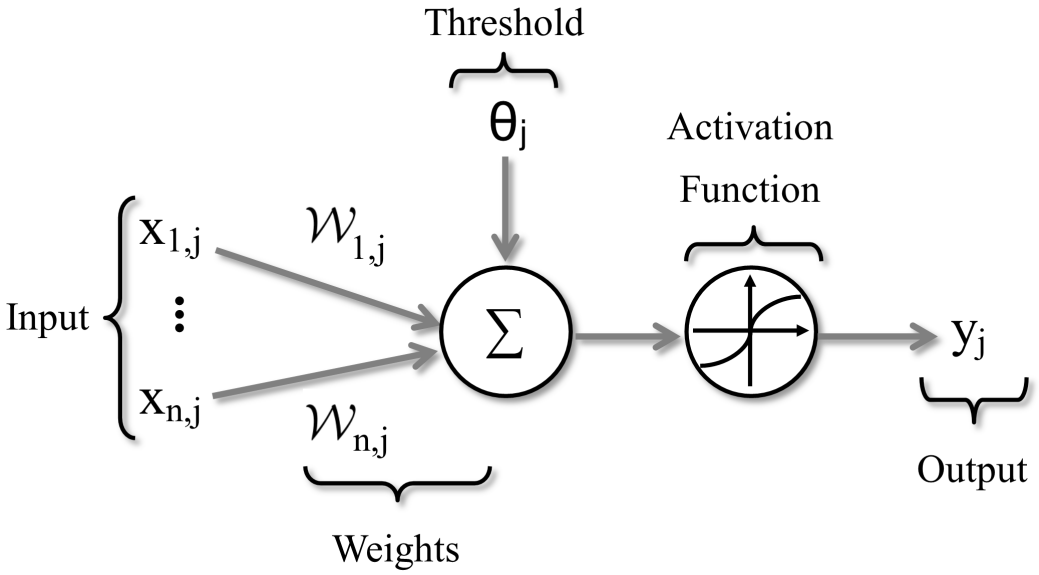


Figure 5.2: Simplified schematic of an ANN.

The activation function $g(\cdot)$ generates an output signal corresponding to weighted sum the input stimulus. This function can take different forms, ranging from a simple linear function, to ramp and step functions [103]. One of the most common form of the activation function, is the Sigmoid function which can be described by the following equation [2]

$$g(x) = \frac{1 - e^{-x}}{1 + e^{-x}} \tag{5.2}$$

The two most fundamental properties of NNs that makes them appealing for problems involving function approximation or regression, are the ability to perform supervised learning, and excellent computational efficiency. Machine learning can be

[2] The form given in equation (5.2) is an example of the so-called bipolar Sigmoid function. Other forms of Sigmoid functions are available and are defined differently.

broadly classified into three categories of supervised, unsupervised and reinforcement learning. In supervised learning, which is the method of choice in this thesis, some information regarding the desirable output is available and is used during the training process. NN models are able to *learn*, using a set of training rules and external instructions, and improve their performance over time [103]. The main objective during the training process of a NN is to fine-tune and adjust the weights of neurons in the network. Furthermore, NNs, due to their massive parallel structure can potentially perform fast computations, which could overcome the computational complexity of the numerical simulation model described in chapter 3.

The scientific literature is filled with multiple learning algorithms and different structure of NNs, each with its own unique advantages and disadvantages. Among the commonly used type of NNs are the multilayer feedforward networks trained based on the supervised back-propagation learning algorithm. The so-called Multi Layer Perceptron (MLP) NN has one input layer, one or more hidden layers, and an output layer. In this thesis, the MLP network architecture along with the Levenberg–Marquardt back-propagation training algorithm is employed. Structure of the network, as well as the training procedure is explained as follows.

### 5.1.2 Structure of the MLP

The structure of the MLP used in this study is illustrated in Figure 5.3. Once again, going back to the definition of power harvesting efficiency provided in section 4.3 and the amount of electrical charge defined by equation (3.34) and equation (3.35) of chapter 3, it can be seen that the efficiency is dependent on many physical and geometrical properties of the harvester, as well as the storage circuit. However, clear

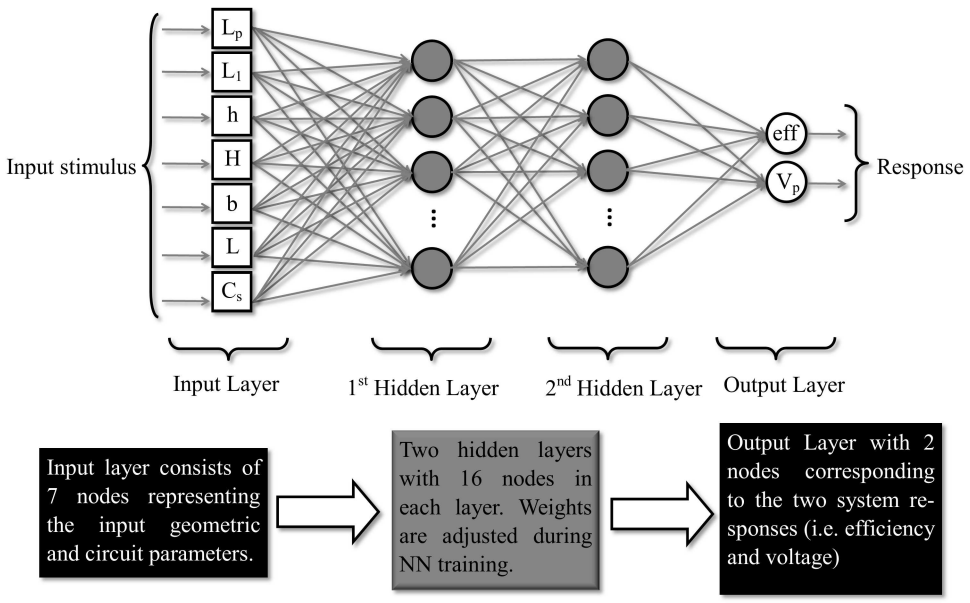


Figure 5.3: Structure of the MLP with 7 input nodes, 2 hidden layers and 2 output nodes.

mapping between a change in the physical or geometric variables and efficiency is not straightforward. This is in fact, the type of problem in which NNs excel.

The number of neurons in the input and output layer are problem specific, and as can be seen in Figure 5.3, the input layer consists of 7 input nodes corresponding to the 7 input parameters, while the output layer has only 2 neurons. The selection of input and output parameters is of paramount importance. Special care was taken to include any parameters that mostly influence the efficiency of energy harvester and power generation. These include six geometric parameters (piezoelectric patch length $L_p$ (m), patch location from the fixed-end $L_1$ (m), patch thickness $h$ (m), beam thickness $H$ (m), beam width $b$ (m), overall beam length $L$ (m)) and one circuit parameter (size of the external storage capacitor $C_s$ $\mu$F ).

The two neurons in the output layer correspond to efficiency of the system and the

generated piezoelectric voltage ($V_p$). The reason behind considering $V_p$ as an output of the network is as follows. Although the efficiency is a good measure for how good the design of a particular harvester is, for many practical application, such as the remote wireless sensors, the amount of voltage generated is also highly important, as certain electronic circuits and devices cannot maintain proper functionality if the supplied voltage drops below a certain threshold. Finally, there are 16 nodes in each of the hidden layers used in the MLP. Although there are certain guidelines for selecting the number of nodes in the hidden layer of a MLP, this process involves a certain number of trial and errors [103]. Generally speaking, there is a direct proportionality between the number of nodes in the hidden layer and the level of non-linearity in the process to be modeled by the NN [90].

### 5.1.3 Training of the MLP

As mentioned before, the training of the NN was performed using the Levenberg–Marquardt algorithm [105, 106]. There are several advantages to the Levenberg–Marquardt training algorithm that make it suitable for small to medium-sized problems, including fast and stable convergence [107]. Initially, the numerical simulation model of chapter 3 was used to generate datasets for NN training. Separate datasets were generated for base-motion and point-force excitation. Each dataset contained in total of 1000 data points corresponding to 1000 simulation runs. All simulations were performed with randomly generated inputs. Note that the magnitude and frequency of the external excitation signal, as well as the magnitude of the base excitation were kept constant through out the generation of training and test datasets.

Table 5.1 tabulates the number of nodes in each layer of the network. It should also be mentioned that resonance (50 Hz) and around resonance data (±10 Hz of the target resonance frequency) were removed from both the training, and the test dataset through a data cleaning process. The reasons is that during the NN training, if around resonance data were to be used, the outputs (efficiency and voltage) were orders to magnitude larger than non-resonance condition and therefore, around resonance data were treated as outliers (i.e. data points that are significantly larger or smaller than the rest of the training data) and removed through a data cleaning process. The exact range of the data being treated as outliers is application specific. However, following general guidelines may be considered.

Table 5.1: MLP parameters and Neural Network Training

| | |
|---|---|
| Number of nodes in the input layer | 7 |
| Number of hidden layers | 2 |
| Number of nodes in each hidden layer | 16 |
| Number of nodes in the output layer | 2 |
| Size of the training set | 750 |
| Size of the test set | 250 |

Ranges above the chosen ±10 Hz may be acceptable, given that the NN model can still be properly trained for the intended range of operation of the harvester. It is noted one more time that the NN model requires enough training data to capture the underlying trend across the frequency spectrum. If large portion of the data is removed prior to training the network, then the NN will not be able to properly predict the behavior of the system, as the network was not trained for the full range of operation of the system. On the other hand, using ranges below the selected ±10 Hz requires more investigation and analysis. To explain this further, the rationale

behind removing resonance data will be reiterated below.

In the context of function approximation and prediction using NN models, outliers can result in an increase in the variability of the dataset. Proper training of NN models for data with higher variability is challenging, and may result in a more complex NN structure with larger number of nodes and hidden layers. Higher number of hidden layers and nodes may further reduce the adaptability of the trained network and can potentially increase the chance of over-training is therefore not always desirable. It should be further clarified that since the excitation frequency was selected to be in the vicinity of the second natural frequency, only data $\pm 10$ Hz of the second natural frequency was removed from the NN training set, and the data points around the first natural frequency were included in their entirety during NN training.

In order to quantify the training performance, the notion of squared correlation coefficient, also known as the $R^2$ measure was employed. $R^2$ is a statistical measure that quantifies the performance of fit in regression analysis, and can be obtained as follow [108].

$$R^2 = 1 - \frac{\sum_{i=1}^{n} e_i^2}{\sum_{i=1}^{n} (y_i - \bar{y})^2} \tag{5.3}$$

where $e_i = y_i - \hat{y}_i$ is the residual prediction error, $y_i$ , $i = 1, \ldots, n$, is the output of the test data obtained from the numerical simulation model and $n$ is the total number of test data, $\hat{y}_i$ is the predicted output of the NN, and finally, $\bar{y}$ is the mean of the test data outputs. From equation (5.3), it can be seen that the closer the $R^2$ is to unity, the better the ANN has been trained. A test set with known input and

output parameters were used to calculate $R^2$ values for each NN training.

## 5.2 Simulation-Based Optimization via Genetic Algorithm

Selection of an appropriate algorithm for a particular optimization problem requires insight into the nature of the problem and a good grasp on the pros and cons of the available optimization techniques. Much like many areas of mathematical programming, computer optimization progressed with phenomenon speed over the past few years. Many new techniques were introduced, and many existing methods were further analyzed for convergence and stability. However in many cases, the choice of the algorithm employed for a particular problem is limited by the nature of the problem itself. Justification as to why a particular algorithm is chosen should therefore be provided.

If one were to define optimization as a logical search in which the goal was to obtain values of parameters that maximized (or minimized) a certain OF (also known as the fitness function), then one could broadly categorize optimization algorithms based on the way the logical search was performed, and the way the OF was evaluated. Most real-world problems are complex and usually stochastic. Therefore, closed-form solutions are either unknown, or very difficult or time-consuming to obtain. Although approximate closed-form solutions are available for many physical phenomenon, the simplifying assumptions oftentimes make the model too simplistic for optimization process in a real-world scenario. Therefore, model-based optimization methodologies that require analytical closed-form OFs, or need derivative or integral information

of the function are not always practical.

Unlike model-based methods, model-free or black-box optimization techniques only require the numeric value of the function. It is in such cases that simulation models are useful and can be used during the optimization process [90]. A class of model-free methods, known as *metaheuristics algorithms* (e.g. the downhill simplex or Nelder-mead algorithm [109], simulated annealing [110], or GA) were successfully applied to many real-world problems. As mentioned in chapter 3, PEH when considered in the context of a system operating in transient with interfacing and storage circuitry, can be better explained through a simulation model, as opposed to a closed-form analytic equation. That is why for the problem at hand, GA optimization was paired with a numerical OF based on the numerical simulation model and the corresponding trained NN. While the basics of GA optimization is straightforward, the concept might be unfamiliar to some portions of the audience of this thesis. Therefore, in the interest of reader-friendliness and clarity, a rather brief overview of the concept, along with a working example of a benchmark test function using GA optimization are provided.

### 5.2.1 Genetic Algorithms - Basic Concepts

GA optimization is essentially a search method that is built upon the principles of evelotionary biology and natural selection [111]. GA benefits from many advantages that metaheuristics algorithms offer. First and foremost, is the model-free nature of the GA which makes it a suitable choice for numeric OFs, or when no derivative information is available. In fact, OF in GA optimization can be any function that takes a certain number of input parameters, and generate a set of outputs (similar to

NNs). This makes GA optimization a perfect candidate for optimization problems involving numerical or experimental data. Second, under certain conditions, GA leads to a global optimization solution, as opposed to a local solution, which is also a very useful property when dealing with optimal design problems.

Generally speaking, an optimization problem using GA is comprised of the following five main steps.

i. **Chromosome encoding and generation of the initial population**.

This is the first step in defining a GA optimization problem. In this step, the optimization variables are arranged together to form a chromosome. The chromosome is simply a vector of parameters to be optimized. There are commonly two ways that variables can form a chromosome. The so-called binary-coded GA uses binary (ones and zeros) representation of the variables. Using a binary representation does not limit the use of this algorithm in problems involving real-values, as real integer values can be converted into binary numbers. The major concern is the so-called quantization error [111]. However, quantization error is inversely proportional to the number of bits ($N_{bits}$) used to represent the binary variable. Thus, selecting a large $N_{bits}$ reduces the effect of the quantization error. The algorithm then forms a relatively large number of randomly generated initial population ($N_{ipop}$) of chromosomes. Choosing a large number of $N_{ipop}$ is favorable, as it will increase the chances of finding a global solution [3].

ii. **OF evaluation and natural selection**.

[3] Large $N_{ipop}$ does not necessarily guarantee convergence to a global solution, but it significantly increases the change of a global solution.

The next step, is the evaluation of the OF for all chromosomes in the $N_{ipop}$ and selection of the chromosomes to form the subsequent generation. Through the process of natural selection, fittest candidates (i.e. candidates with the highest OF evaluation, or lowest cost) are selected to form the next generation. The next generation population ($N_{pop}$) is usually smaller in size than the $N_{ipop}$. The usual method of selecting the fittest chromosomes is to rank each chromosomes of the initial population based on their OF evaluation, and then select from the top of the list (i.e. best of fittest chromosome), going down.

iii. **Pairing**

Pairing is the process of selecting certain number of good chromosomes and forming the so-called mating pool. In each generation following the initial population, $N_{good}$ chromosomes are chosen to produce new offspring. There are multiple ways for the selecting the parent chromosomes. Random pairing, rank weighting and tournament selection are among the most popular methods (details for each method can be found in [111].).

iv. **Mating**

Usually, two parent chromosomes generate two new chromosomes (offspring) during the mating process. The idea is that since both parent chromosomes showed good traits (according to their respective OF evaluation), the resulting offspring is also expected to be fit, and might even lead to better performance.

v. **Mutation**

In optimization terms, mating, is in essence the exploitation of the local search space in hope of a better solution. On the other hand, mutation is the

exploration of the OF surface area. In order to prevent the algorithm from getting stuck in a local search area and increasing the chance of finding a global solution, a random portion of the population (usually between 2% to 5% of the $N_{pop}$) are mutated. That is to say that a portion of the chromosomes are deliberately modified to explore new traits. Thus, the mutation rate can set the trade-off between exploitation and exploration.

### 5.2.2 Benchmark Example

In the context of optimization, it is beneficial to have a number of functions with known global minima/maxima for performance evaluation purposes. A number of these so-called benchmark functions are available throughout literature. Benchmark functions can also be used to evaluate if a particular optimization algorithm is working properly. One of the commonly used benchmark functions, is the so-called Ackley function, first proposed by David Ackley in his Ph.D dissertation [112]. In the 2-D domain, the Aukley function is represented mathematically by:

$$f(x_1, x_2) = -a\ exp\Big(-b\sqrt{\frac{1}{2}(x_1^2 + x_2^2)}\Big) - \ exp\Big(\frac{1}{2}\cos(2\pi x_1) + \cos(2\pi x_2)\Big) + a + exp(1) \tag{5.4}$$

where $a = -20$ and $b = 0.2$ are the recommended values [113]. The mesh plot of the Ackley function for $-5 \leq x_1, x_2 \leq 5$ is illustrated in Figure 5.4.

The global minima of the Ackley function is known to be located at $f(0, 0) = 0$. A binary-coded GA with an initial population size of 100 random variables written

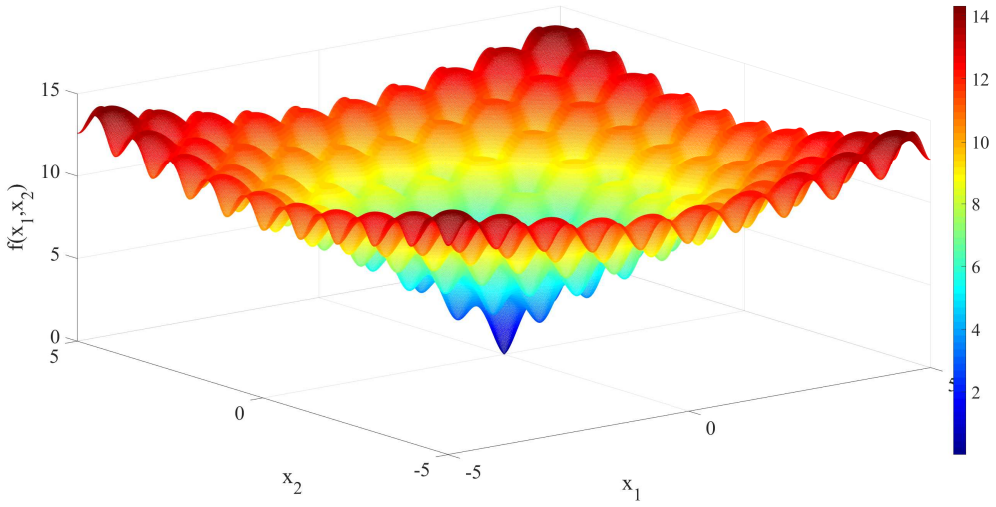


Figure 5.4: Mesh plot of the Ackley test function.

in MATLAB® is used as the optimization algorithm. The total number of bits in each gene is chosen to be 64, and the mutation-rate of 2% is selected. The pairing process is based on the rank weighting method [111].

Point distributions over the contour plot of the function's $x_1 - x_2$ plane are shown in Figure 5.5. The randomness of the initial population is clearly observed in Figure 5.5 (a). The second (Figure 5.5 (b)), third (Figure 5.5 (c), and twelfth (Figure 5.5(d)) distribution of points are also illustrated. Figure 5.5 clearly shows the convergence of the algorithm towards the global solution. Comparing Figure 5.5 (a) with Figure 5.5 (d), it can be seen that point distribution is initially scattered in the search space, and as the algorithm iteration progress, more points are located in the vicinity of the known global minima at $f(0, 0)$.

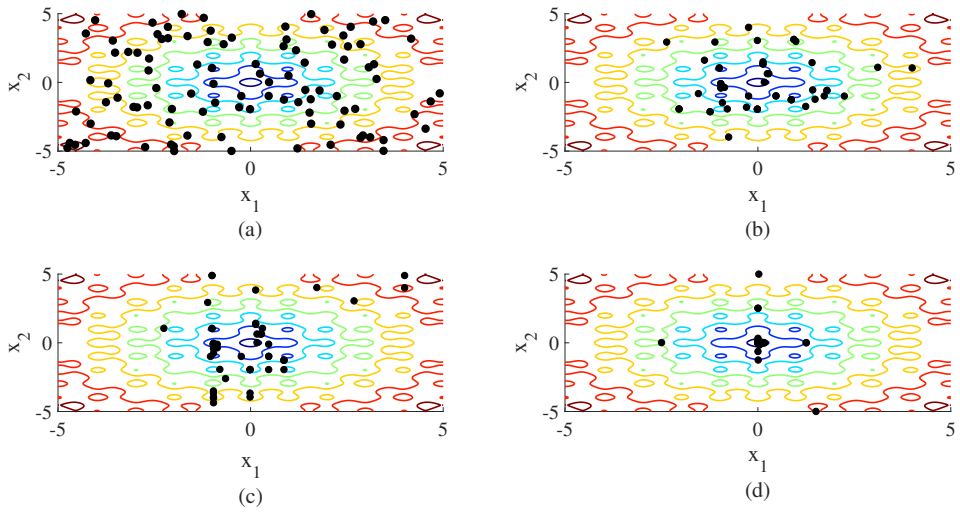


Figure 5.5: Contour plot of the Ackley function with associated point distribution for the initial (a), second (b), third (c), and twelfth (d) population of GA.

## 5.3 GA for PEH optimal design problem

As mentioned earlier in section 5.1.3, the 7 input variables are considered during the optimization process, leading to a 7-dimensional optimization problem. The chromosome for this particular problem is a row vector given in equation (5.5). The goal is to find the combination of the parameters in the chromosomes that results in the optimal value of the OF.

$$chromosome = [L_p \, L_1 \, h \, H \, b \, L \, C_s] \tag{5.5}$$

As is the case with all real-world optimization problems, there are always constraints and limitations on the input parameters. In the problem under study here, such constraints can be thought of as geometric limitations for the cantilever beam and the piezoelectric patch that the system designer should consider. The lower and upper limits for system parameters to be optimized is tabulated in Table 5.2.

Table 5.2: PEH physical parameters for the optimization problem, and the corresponding upper/lower bounds.

| Parameter | Lower Limit | Upper Limit |
|---|---|---|
| $L_p$ (m) | 0.002 | 0.4 |
| $L_1$ (m) | 0 | 0.4 |
| $h$ (m) | $5e^{-4}$ | $1e^{-3}$ |
| $H$ (m) | $5e^{-3}$ | $5e^{-2}$ |
| $b$ (m) | $5e^{-3}$ | 0.1 |
| $L$ (m) | 0.4 | 0.6 |
| $C_s$ ($\mu F$) | $1e^{-6}$ | $20e^{-6}$ |

In many practical optimization problems, it is common to have a fitness functions with more than one output. In the so-called multi-objective optimization problem, a set of sub-objectives are defined and the algorithm tries to find optimal values for all objectives, or find appropriate trade-off between conflicting objectives. For this study, a multi-objective OF is defined with piezoelectric voltage $V_P$ and the energy harvesting efficiency as outputs. Note that higher piezoelectric voltage does not necessarily translates to higher efficiency due to the inverse piezoelectric effect defined in chapter 2. This gives the system designer the flexibility to establish a balance between higher efficiency or higher generated piezoelectric voltage.

The OF is then evaluated for each chromosome in the initial population:

$$[eff\ V_p] = f(chromosome) = f(L_p\,, L_1\,, h\,, H\,, b\,, L\,, C_s) \tag{5.6}$$

To account for different scales of each of the sub-objectives in equation (5.6), a weighting factor can be used. Thus, the final weighted OF used in the GA

optimization is given as:

$$OF = (G_1 \times eff) + (G_2 \times V_p) \tag{5.7}$$

where $G_{1,2}$ correspond to the weights of the different sub-objectives. The designer can favor one objective over the other by changing these gains. For instance, in the case where a particular application requires higher voltage, $G_2$ can be selected to be higher than $G_1$ to put more emphasis on voltage, and, when higher efficiency is more desirable, $G_1$ can selected to be higher. This is a commonly used approach in multi-objective optimization and is usually referred to as the weighted-sum approach [114]. The weighted-sum is one of the simplest methods of defining a multi-objective OF. There are in fact other methods in the literature. Interested reader can refer to [115] for a comprehensive survey of some of these methods. Note that the numeric value of the OF is obtained from the NN model described in section 5.2, which was trained based on the data obtained from the numerical simulation model of chapter 3. More precisely, for each chromosome as the input to the network, NN output corresponds to the OF evaluation.

For this study, a natural selection rate of 50% is chosen, meaning that after each iteration, half of the chromosomes are selected to carry on their traits to the next generation. A diagram of the GA algorithm described above is depicted in Figure 5.6 and GA settings used in this thesis are summarized in Table 5.3. Selection of appropriate structural parameters in GA is application dependent. Nonetheless proper selection of these parameters is key in finding the optimal solution. For instance, while high mutation rate can cause the loss of a high fitness chromosome, low mutation rate reduces the chance of finding a global solution. The settings used

in this thesis are based on the guidelines proposed by Haupt *et al.* [111].

Table 5.3: GA optimization settings

| | |
|---|---|
| Number of parameters to optimize ($N_{pra}$) | 7 |
| Initial Population ($N_{ipop}$) | 2000 |
| Population ($N_{pop}$) | $\frac{N_{ipop}}{2} = 1000$ |
| Selected population for mating pool($N_{good}$) | $\frac{N_{pop}}{2} = 500$ |
| Maximum iteration | 200 |
| Mutation rate | 5% |

In order to investigate the effect of GA setting on the optimal design values, multiple settings were tested with the key parameters changed and their effect studied (except for the $N_{pra}$ which specific to this problem formulation). Also note that changing $N_{ipop}$ would in turn change the population size ($N_{pop}$) and the mating pool population ($N_{good}$). Maximum iteration was increased when larger population sizes were selected to ensure full convergence of the algorithm to optimal values. Reduced mutation rate of 2% was also examined.

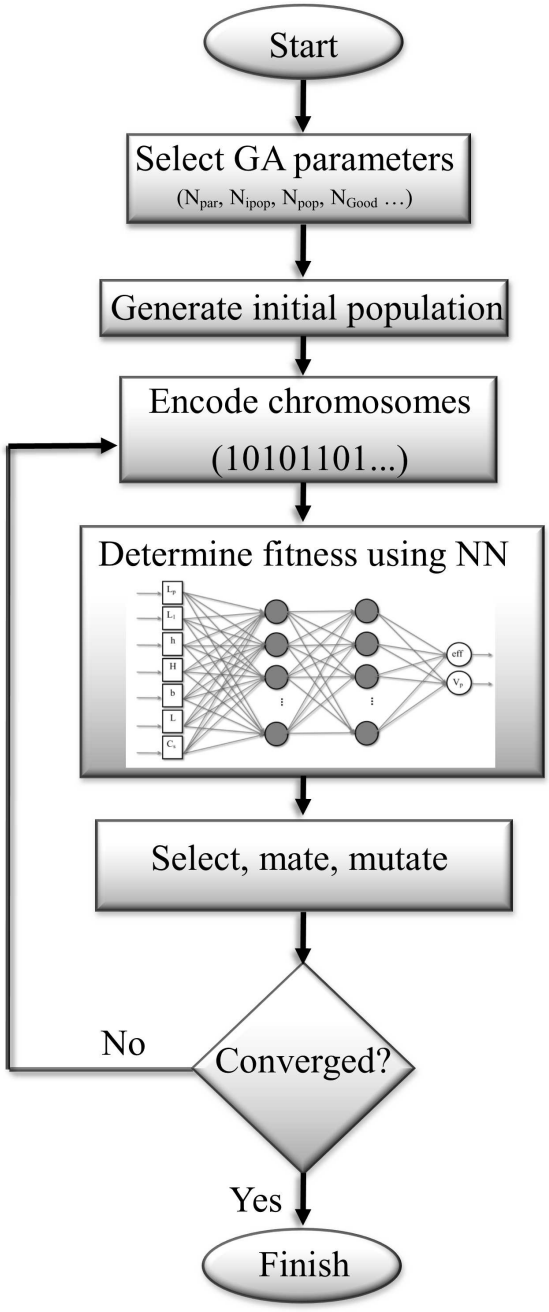


Figure 5.6: GA optimization flowchart.

## 5.4 Results and Discussions

This section summarizes the findings of this thesis in the pursuit of an optimal design criteria for PEH. Validity of the obtained optimal parameters are thoroughly analyzed. Before presenting the optimization results, the training performance and quality of the NN model is investigated, as one must first ensure that the NN model can effectively replicate the behavior of the simulation model.

### 5.4.1 NN training performance

As mentioned in section 5.1.3, a collection of randomly generated input/output relationships obtained from the original simulation model was used to generate two sets of training and test data. Approximately 1000 simulation runs were performed for each operating condition, that is, the cantilever beam under harmonic base-motion or tip force. Of the total number of 1000 data, approximately 75% were used for training the NN model, and the remaining 25% were used for performance evaluation. There are general guidelines in the literature on how to divide the total dataset into a training set and a performance evaluation set (e.g. Guyon [116]). The decision depends on a variety of factors including the size of the available dataset, as well as the variability of the data. The 3:1 ratio used in this thesis is a commonly used ratio in NN training. Following subsections describe the results obtained from the NN training.

**Beam under harmonic tip-force**

Figure 5.7 shows the regression plot for the NN training using the training dataset, and the performance evaluation using the test dataset both of which were obtained from the numerical model. The top plots of Figure 5.7 correspond to the predicted efficiency during training (top-left) and test (top-right), while the two bottom plots of Figure 5.7 correspond to the predicted piezoelectric voltage ($V_p$) for training (bottom-left) and test (bottom-right). The highest and lowest squared correlation coefficients ($R^2$) were obtained for the efficiency (top-left plot of Figure 5.7), and piezoelectric voltage test set (bottom-right plot of Figure 5.7), respectively. It can be seen that the variability of the training dataset for voltage output is higher than the variability of the efficiency dataset. This can explain the lower obtained $R^2$ value of 0.8679 for the test set. Nonetheless, for all four cases shown in Figure 5.7, the relatively high value of $R^2$, and also the relatively good agreement between the predicted output obtained from the NN, and the target output obtained from the numerical model, lead to the justification that the NN model for the case of the tip-force excitation is tuned to a satisfactory degree.

Furthermore, Figure 5.8 illustrates a comparison between the outputs obtained from simulation model (denoted as the *true values*) and the trained NN for only a few samples of the test dataset. Figure 5.8 (a) clearly shows that proper selection of system parameters can significantly improve efficiency. For both outputs (efficiency and $V_p$), predicted values obtained from the trained NN closely matches the true values of the simulation model.

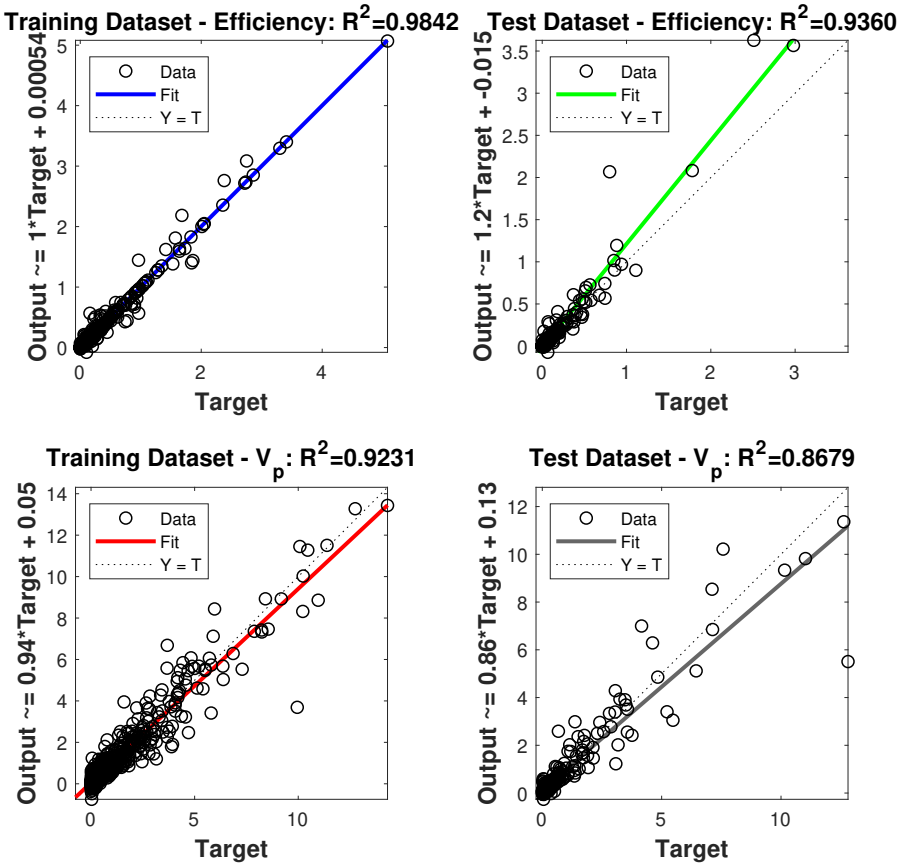


Figure 5.7: Regression plots for NN training (left) and test (right) datasets considering efficiency (top) and voltage (bottom) for the cantilever beam under tip-force

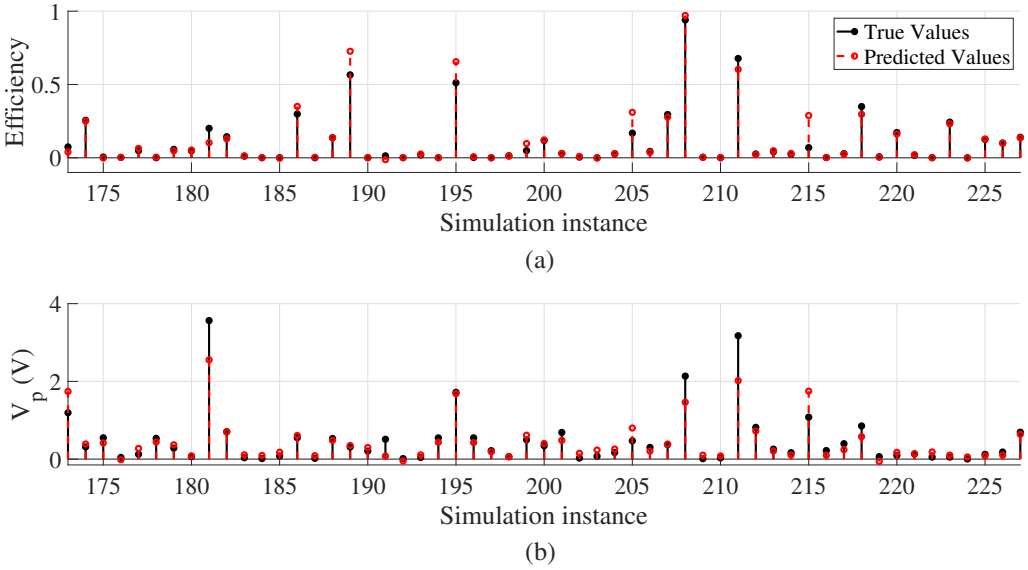


Figure 5.8: Difference between predicted values (obtained from NN) and true values (obtained from numerical model) for (a) efficiency and, (b) voltage using the tip-force test set.

### Beam under harmonic base-excitation

Similar to tip-force operating condition discussed in the previous sub-section, regression plots and prediction errors for base-excitation are illustrated in Figure 5.9 and Figure 5.10. From Figure 5.9 it can be seen that lower variability of the data results in a better training performance. This is evident from the higher $R^2$ values obtained for this case. The highest $R^2$ value of 0.99 was obtained for training dataset and voltage output. Similar to Figure 5.8, Figure 5.10 shows the difference between true and predicted values for the base-excitation case. The good agreement between predicted and true values is the result of successful NN training.

Two other important criteria to consider when training a NN is the possibility of over-fitting the network. Generally speaking, over-fitting is mostly related to the size of the nodes in the hidden layer [117]. Over-fitting the network reduces the

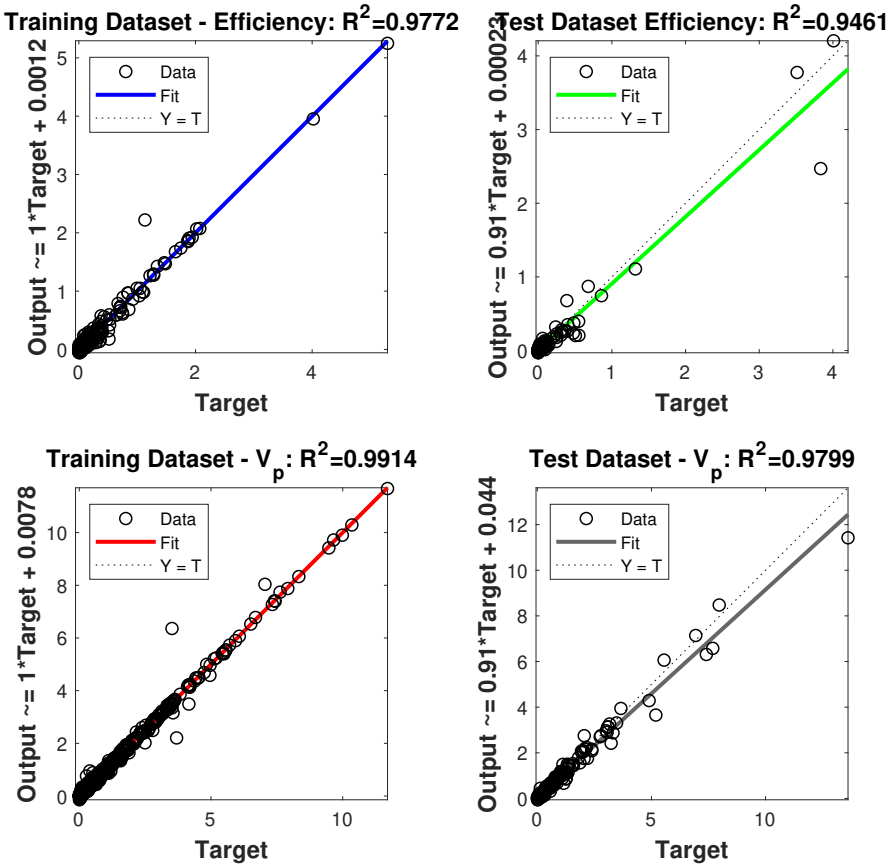


Figure 5.9: Regression plots for NN training (left) and test (right) datasets considering efficiency (top) and voltage (bottom) for the cantilever beam under base-excitation

network's predictive ability and can negatively influence the performance of the network when dealing with new test data (i.e. any data other than the data NN used during training). Figure 5.11 shows the learning progress of the NN model in time. It can be seen that the Mean Square Error (MSE) for the training set is monotonically decreasing at each epoch as expected. However, the MSE for the test set decreases up until epoch 28, and then slightly increases for each epoch afterwards. This flags that an over-training is happening in the network. In order to avoid this

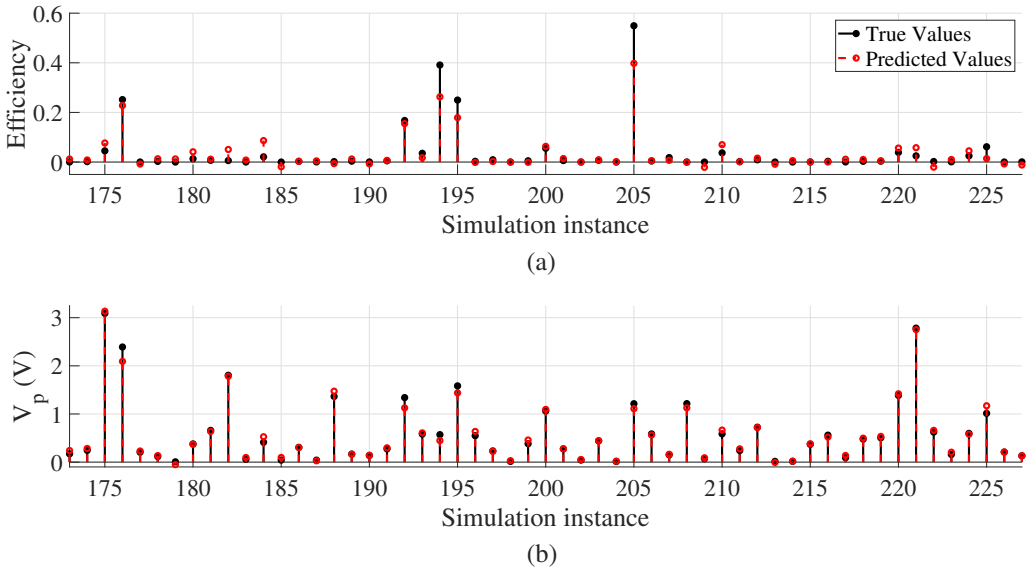


Figure 5.10: Difference between predicted values (obtained from NN) and true values (obtained from numerical model) for (a) efficiency and, (b) voltage using the base-excitation test set.

over-training, the training algorithm was forced to stop, if the MSE of the test set started to monotonically increase for 6 consecutive epochs.

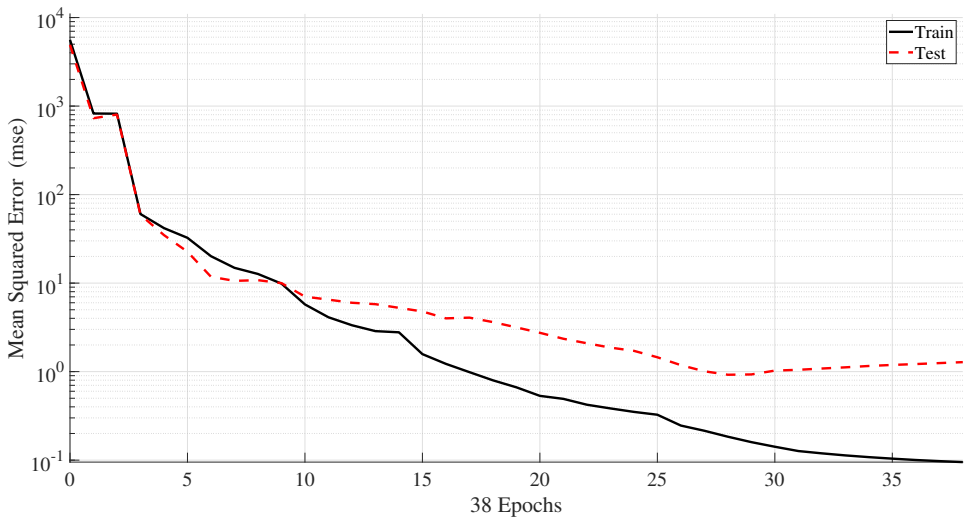


Figure 5.11: MSE vs. the number of epoch.

### 5.4.2 GA optimization results

After confirming the accuracy and performance of the trained NN, several GA optimizations were performed in order to find the optimal input parameters defined earlier in Table 5.2. It is helpful to look at the progress of the average, and the best (fittest) individual of each generation as the evolution progress. Figure 5.12 shows the average fitness and the best chromosome as a function of generation number. It can be seen that in this particular optimization, GA converges after $\approx 40$ generations. Note that the large number of initial population ($N_{ipop} = 2000$), the relatively large population size ($N_{pop} = 1000$), as well as the total number of generations it takes to reach to the solution, leads to multiple evaluations of the OF. Once again, the use of the computationally efficient NN model instead of the expensive-to-evaluate numerical simulation model is justified.

Table 5.4 tabulates several results obtained from multiple GA optimization. For

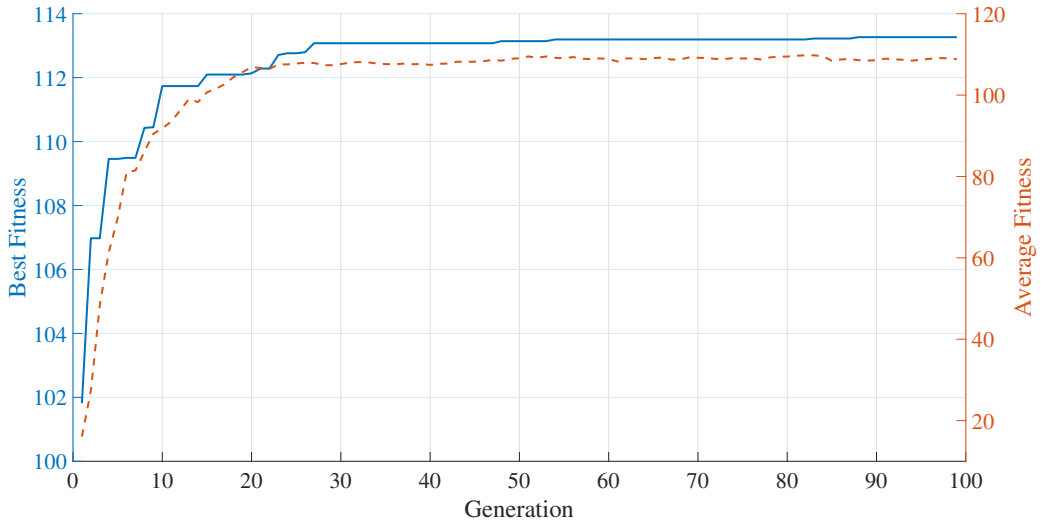


Figure 5.12: Average and best fitness of the generations

each operating condition (tip-force and base-excitation) two trained NN models were used to perform the OF evaluation. Using two different trained NNs for each case study helps investigate the sensitivity of the obtained designed parameters to NN training, and also the consistency of the optimization results. Note that the only difference between the two trained networks for each operating condition is the initial weights of the network nodes which causes the training to continue in a different direction. While some variations are observed in certain parameters (most noticeably piezoelectric length and location from the fixed-end) obtained optimal parameters are relatively consistent. Following comprehensive analysis and justifications are presented for data tabulated in Table 5.4.

Table 5.4: PEH optimal design parameters

| | | $R^2$ | $G_1$ | $G_2$ | $L_p$ (m) | $L_1$ (m) | $h$ (m) | $H$ (m) | $b$ (m) | $L$ (m) | $C_s(\ \mu)$F | $eff$ | $V_p$ (v) |
|---|---|---|---|---|---|---|---|---|---|---|---|---|---|
| Tip-excitation | NN1 | $OF_1 = 0.8730$ | 1 | 0 | 0.147 | $1.40e^{-3}$ | $9.97e^{-4}$ | 0.016 | 0.098 | 0.592 | $1.08e^{-6}$ | 1.9991 | 20.6 |
| | | $OF_2 = 0.8445$ | 1 | 0.01 | 0.157 | $3.10e^{-3}$ | $9.98e^{-4}$ | 0.015 | 0.098 | 0.594 | $1.01e^{-6}$ | 1.2655 | 12.93 |
| | NN2 | $OF_1 = 0.9360$ | 1 | 0 | 0.248 | $2.96e^{-4}$ | $9.79e^{-4}$ | 0.019 | 0.099 | 0.599 | $1.68e^{-6}$ | 3.1258 | 16.616 |
| | | $OF_2 = 0.8679$ | 1 | 0.01 | 0.251 | $3.32e^{-4}$ | $9.96e^{-4}$ | 0.019 | 0.099 | 0.6 | $1.56e^{-6}$ | 2.5584 | 13.586 |
| Base-excitation | NN1 | $OF_1 = 0.9461$ | 1 | 0 | 0.2653 | $4.59e^{-4}$ | $9.11e^{-4}$ | 0.017 | 0.055 | 0.597 | $1.0e^{-6}$ | 9.42 | 14.86 |
| | | $OF_2 = 0.9199$ | 1 | 0.01 | 0.2794 | $1.16e^{-4}$ | $8.95e^{-4}$ | 0.017 | 0.059 | 0.598 | $1.13e^{-6}$ | 7.19 | 22.06 |
| | NN2 | $OF_1 = 0.9115$ | 1 | 0 | 0.242 | $2.5e^{-4}$ | $9.91e^{-4}$ | 0.018 | 0.0988 | 0.5974 | $1.28e^{-6}$ | 8.34 | 12.204 |
| | | $OF_2 = 0.9728$ | 1 | 0.01 | 0.2555 | $5.59e^{-4}$ | $9.99e^{-4}$ | 0.017 | 0.0991 | 0.5975 | $1.05e^{-6}$ | 2.7 | 22.048 |

As was previously mentioned in section 5.3, $G_1$ and $G_2$ are the tuning parameters that the system designer can employ to favor either the piezoelectric voltage, or the energy harvesting efficiency during the course of the optimization process. For the results presented in Table 5.4, two cases are considered where only the energy harvesting efficiency (as defined earlier by equation (4.1) in chapter 4) is of interest ($G_2 = 0$), or efficiency is favored 100 more than voltage ($G_1 = G_2 \times 100$). Needless to say that any ratio between the tuning parameters can be used, with the only consideration being the actual numeric value of $G_1$ and $G_2$ which depends on the relative scale of the parameters in the OF. Looking at column 6, the piezoelectric length ($L_p$ (m)) and column 7, the location of the piezoelectric patch from the fixed-end ($L_1$ (m)), the GA converges to optimal $L_p$ and very small $L_1$ values, which corresponds to the patch close to the root of the beam. This is physically justifiable since high root strain would increase both efficiency and voltage, and therefore positioning the piezoelectric patch closer to the root is a logically sound choice. In all case studies, optimal $L_1$ converges to the lower-bound limit of zero, which corresponds to the root of the cantilever beam.

Optimal values for the thickness of the piezoelectric patch ($h$ (m)) and the beam thickness ($H$ (m)) are another consistent parameters throughout the two case studies. It can be seen from the column 8, that the optimal $h$ value is very close to the upper-bound defined in Table 5.2, so the thicker the piezoelectric patch, the higher the efficiency and voltage. This result is consistent with the piezoelectric constitutive equations in which generated electrical charge is proportional to the thickness of the piezoelectric patch. Note that the optimal choice of $H$ is not significantly influenced by the choice of the tuning gains $G_1$ and $G_2$, or even the type of beam excitation (i.e.

tip-force vs. base-excitation). In fact, for both case studies, thickness, $H$ averaged at $\approx 1.73e^{-2}$ (m).

Looking at the optimal length of the beam $L$, it can be seen that the optimization algorithm converged to the upper-bound value of 0.6 (m). This can be justified taking into account the target frequency and the natural frequency of the beam. Natural frequencies of the beam become smaller as the length increases. In the case of this optimization problem, the target frequency is fixed at 50 Hz to replicate the experimental and parametric studies of chapter 4. The closer the first natural frequency is to the target frequency, the harsher the movements of the beam and the higher the deflection along the beam length. The parameter that has the most influence on the natural frequency is the beam length. Interestingly, for all case studies tabulated in Table 5.4, the first natural frequency of the beam is relatively close to the target frequency of 50 Hz (averaged at $\approx 51.3137$ Hz). This is despite the fact that during NN training resonance data at $\pm 10$ Hz away from 50 Hz were treated as outliers and were intentionally removed from the training dataset.

This is further proof that properly trained NN can learn and mimic the behavior of a complex dynamical PEH in a satisfactory manner. NN does that by observing the data trend before and after the resonance frequency. The training data shows a rising trend before resonance followed by a decline in voltage. Although the actual numeric values predicted by the NN for around-resonance operation are not accurate (because the NN had not been trained for that operating condition), the rising trend around resonance mimicked by the NN correctly leads the GA towards the correct optimal values.

The optimal size of the external storage capacitor $C_s$, which is the only circuit

parameter throughout this optimization process, is also found to be relatively small. The reason is that perhaps larger values of $C_s$, although can potentially store more electrical energy, takes longer time to fully charge. Therefore, the total mechanical energy consumption is also higher, which, based on the efficiency definition used in this thesis, can reduce the overall energy harvesting efficiency. This might not always be the case and depends on the efficiency definition used. Finally, the last two columns, $eff$ and $V_p$ are the results obtained from the original numerical simulation model where the optimal parameters were used as inputs. It should also be noted that since the magnitude of the force for the tip-force case study, and the displacement amplitude of the base for the base-excitation case study does not have the same physical units, the optimization results for the two different case studies are not directly comparable.

The optimization results discussed thus far were obtained using the GA settings provided in Table 5.3. However, multiple simulations were performed with different settings to study the effect of GA settings on the obtained optimal design parameters. For instance, reducing the number of initial population from the original setting of 2000 to 1000 for the base excitation case study with $NN1$, resulted in slightly larger $L_p$ (from 0.2653 to 0.2761) while the patch location was moved further away from the fixed end ($L_p$ reduced from $4.59e^{-4}$ to $3.89e^{-4}$) Other parameters (thickness, width and capacitor size) were not impacted drastically. Note that reducing $N_{ipop}$ by half, in turn reduces the mating pool population by half. Furthermore, reducing the maximum iteration number by half (from 200 for results in Table 5.4 to 100) had a bigger impact on the optimal beam and patch length. As an example, the optimal beam length of 0.592 m for the first tip excitation case study, reduced to

0.482 m. That is because the maximum iteration number was reached and the GA optimization was terminated before converging to the final optimal value. Reducing the mutation rate form 5% to 2% had a minimal effect on the obtained optimal parameters. If very small initial population size was selected, then reducing the mutation rate could potentially impact the global solution as areas of the function space might be left out unexplored. However, for these simulations were at least 1000 initial points are evaluated at the beginning of the search, a 2% mutation rate does not impact the results significantly.

## 5.5 Summary and Chapter Conclusions

This chapter presented a new approach to simulation-based optimization of a piezoelectric energy harvester. It was shown that the combination of a properly trained NN along with the GA optimization provides an efficient tool, well-capable of tackling optimization problems involving expensive-to-evaluate objective functions. It was also shown that through proper training, NN models can adequately mimic the behavior of a piezoelectric energy harvester charging a storage device through electrical interfacing circuit. High $R^2$ values obtained for each case study proved that the proposed MLP structure with two hidden-layers sufficiently captures the underlying behavior of this complex system.

Optimization results obtained from GA were thoroughly analyzed. It can be concluded that certain geometric parameters, such as location of the piezoelectric patch on the host structure and the thickness of the patch, significantly influence the energy harvesting efficiency and therefore, optimal selection of these parameters should be considered. It should also be mentioned that the optimization scheme

proposed here is not limited to the cantilever beam type studied in this thesis and can be easily modified to incorporate other harvester designs, for instance, structures with mechanical non-linearity or different beam harvesters. Based on a simulation model of the system with acceptable performance, input/output data pairs can be used to train proper structure of a NN model, which can then be used in a black-box optimization algorithm, such as the GA.

# Chapter 6

# Thesis Conclusions and Future Works

*"Problems worthy of attack prove their worth by fighting back."*

Piet Hein - Danish Mathematician

This thesis investigated (i) the transient behavior of a piezoelectric energy harvesting system during the charging process of a storage device through different electronic interfacing circuits. While (ii) developing an accurate semi-theoretical model of the energy harvesting system based on the continuum mechanical model, the electromechanical coupling effect, and (iii) the impact of different interfacing circuits on the transient charging process were thoroughly studied. The thesis also (iv) developed an efficient tool for tackling simulation-based optimal design problem of an energy harvesting system. The new optimization scheme benefits from the long list of advantages that modern machine learning algorithms can offer.

This chapter sums up the thesis by restating major contributions of this work. Finally, possible future extensions are provided.

## 6.1 Thesis Contributions

The main contributions of this thesis are threefold: (i) development of an accurate semi-theoretical model of a piezoelectric energy harvesting system considering both the transient piezoelectric coupling, and the charging dynamics, (ii) comprehensive study and analysis, using physical experimentation, of the effect of various interfacing circuits on charging dynamics of the PEH, and, (iii) development an efficient optimization tool based on machine learning and evolutionary algorithms to tackle the optimal design problem of an energy harvester.

### 6.1.1 Semi-theoretical model of the charging process

The proposed semi-theoretical model of the piezoelectric energy harvester combines, for the first time, an accurate continuum mechanical model, and the precise electrical charging process, considering the electromechanical coupling effect. The physical process of charging of the external capacitor by a PEH considering electrical-mechanical coupling effect is well explained through the proposed iteration process. The focus of the proposed model is on transient charging characteristic of the system with different electronic interfacing and storage circuits. The iteration process allows the consideration of exact charge distribution in the system during the transient-phase of the system.

Two common types of interfacing circuits, namely, standard interfacing circuit, and self-powered non-linear SSHI circuit, were modeled and comprehensively studied through experimental tests. The effect of each interfacing circuit on the charging dynamics were carefully examined.

This experimentally validated semi-theoretical model has several distinguishing features, when compared to other modeling approaches, such as:

i. Unlike many of the available PEH modeling techniques that either focus on the mechanical-domain model, and simplify the effect of the electronic interfacing circuits, or vise versa, this numerical procedure is capable of accurately simulating a complete energy harvesting system, comprised of piezoelectric patch, linear or non-linear interfacing, and storage circuit.

ii. Unlike the majority of the proposed analytic expressions for harvested electrical power that overlook the charging dynamics during the transient phase and assume that the system is operating under steady-state condition, the proposed model can be used to simulate and study system's behavior during transient operation. This is an important characteristic of the model, since, in many practical situations, electrical power is delivered to the capacitive load during the transient operation of the harvester.

iii. The numerical nature of the model provides the required versatility to consider a wide range of PEHs and study the effect of various parameters during the modeling phase. For instance, the effect of the series resistance of the SSHI interfacing circuit on the charging transient of the storage device was easily incorporated into the model. In a similar fashion, the mechanical-domain

model can be adapted to include new beam designs (i.e. different geometry, shape, etc.), or consider different boundary conditions.

Overall, based on the results of the experimental studies, proposed numerical model outperforms traditional SDOF models and can be beneficial when considering transient PEH charging dynamics through interfacing circuits.

### 6.1.2 Optimal Design of a Piezoelectric Harvester

The thesis also embarked upon developing a new simulation-based optimization scheme for PEH. Through several experimentation and parametric studies, it was determined that certain geometric and circuit parameters (such as the location of the piezoelectric patch on the host structure, the thickness of the patch, the size of the beam, etc.) significantly influence the overall power harvesting efficiency. Thus, an optimization tool can greatly benefit the system designer.

This new approach to simulation-based optimization of a piezoelectric energy harvester, involves an accurate simulation model of the system (such as the developed semi-theoretical model of chapter 3), a properly trained NN, and a GA optimization. Combination of these elements, provide the system designer with an efficient tool to tackle the design optimization problem.

Proposed scheme is well-capable of tackling optimization problems involving expensive-to-evaluate objective functions. It was also shown that through proper training of the NN model using accurate simulation data, NN can adequately mimic the behavior of a PEH charging a storage device through electrical interfacing circuit. Statistical analysis of the learning process provided in chapter 5 proved that the

proposed MLP structure sufficiently captures the underlying behavior of the complex PEH.

It should also be mentioned that the optimization scheme proposed here is not limited to the cantilever beam studied in this thesis and can be easily modified to incorporate other harvester designs, for instance, structures with mechanical non-linearity or different beam harvesters. So long as a simulation model of the system with acceptable performance is available, input/output data pairs can be used to train proper structure of a NN model, which can then be used in a black-box optimization algorithm, such as the GA.

## 6.2 Possible Future Directions and Recommended Extensions

The modeling approach and the optimization scheme developed in this thesis, while showing good performance, can certainly be improved. Following items are only a few suggestions for future improvements of the topics discussed in this thesis.

i. Development of a fully theoretical model of the PEH that can accurately consider the effect of interfacing circuits and simulating system's behavior in both steady-state and transient operation.

ii. Augmenting the numerical model to incorporate mechanical non-linearity, for instance, using non-linear material property for the host structure, or non-linear beam models.

iii. Numerical modeling and detailed experimental study of the effect of the newly developed SECE interfacing circuit on the transient charging dynamics, and perhaps incorporation of a more accurate model of the diode bridge circuit.

iv. Considering the new Bayesian optimization approach as an alternative to method for optimization during the simulation-based optimization.

v. Experimental evaluation of the optimal design parameters proposed in this thesis using an experimental test setup capable of withstanding large vibration amplitudes.

vi. Modeling and optimization considering multiple piezoelectric elements attached at different locations with different length along the cantilever beam.

vii. Studying the effect of thermo-strain on the transient charging behavior of a vibration energy harvester.

# Bibliography

[1] S. Bagheri, N. Wu, and S. Filizadeh, "Modeling of capacitor charging dynamics in an energy harvesting system considering accurate electromechanical coupling effects," *Smart Materials and Structures*, vol. 27, no. 6, p. 065026, 2018.

[2] S. Bagheri, N. Wu, and S. Filizadeh, "Numerical modeling and analysis of self-powered synchronous switching circuit for the study of transient charging behavior of a vibration energy harvester," *Smart Materials and Structures*, 2019.

[3] S. Bagheri, N. Wu, and S. Filizadeh, "Application of artificial intelligence and evolutionary algorithms in simulation-based optimal design of a piezoelectric energy harvester," *Ready for submission.*

[4] S. Bagheri, N. Wu, and S. Filizadeh, "Simulation-based optimization of a piezoelectric energy harvester using artificial neural networks and genetic algorithm," in *28th IEEE International Symposium on Industrial Electronics (ISIE), Vancouver, Canada*, p. TBD, IEEE, 2019.

[5] A. Keshmiri, S. Bagheri, and N. Wu, "Simulation-based optimization of a non-uniform piezoelectric energy harvester with stack boundary," in *International*

*Conference on Advances in Electroceramic Materials (ICAEM), Vancouver, Canada*, p. TBD, WASET, 2019.

[6] D. Guyomar, A. Badel, E. Lefeuvre, and C. Richard, "Toward energy harvesting using active materials and conversion improvement by nonlinear processing," *IEEE transactions on ultrasonics, ferroelectrics, and frequency control*, vol. 52, no. 4, pp. 584–595, 2005.

[7] E. Lefeuvre, A. Badel, C. Richard, and D. Guyomar, "Piezoelectric energy harvesting device optimization by synchronous electric charge extraction," *Journal of Intelligent Material Systems and Structures*, vol. 16, no. 10, pp. 865–876, 2005.

[8] H. Shen, J. Qiu, H. Ji, K. Zhu, and M. Balsi, "Enhanced synchronized switch harvesting: a new energy harvesting scheme for efficient energy extraction," *Smart Materials and Structures*, vol. 19, no. 11, p. 115017, 2010.

[9] S. Du and A. A. Seshia, "An inductorless bias-flip rectifier for piezoelectric energy harvesting," *IEEE Journal of Solid-State Circuits*, vol. 52, no. 10, pp. 2746–2757, 2017.

[10] K. Cook-Chennault, N. Thambi, and A. Sastry, "Powering mems portable devices—a review of non-regenerative and regenerative power supply systems with special emphasis on piezoelectric energy harvesting systems," *Smart Materials and Structures*, vol. 17, no. 4, p. 043001, 2008.

[11] S. P. Beeby, M. J. Tudor, and N. White, "Energy harvesting vibration sources

for microsystems applications," *Measurement science and technology*, vol. 17, no. 12, p. R175, 2006.

[12] C. Dagdeviren, B. D. Yang, Y. Su, P. L. Tran, P. Joe, E. Anderson, J. Xia, V. Doraiswamy, B. Dehdashti, X. Feng, *et al.*, "Conformal piezoelectric energy harvesting and storage from motions of the heart, lung, and diaphragm," *Proceedings of the National Academy of Sciences*, vol. 111, no. 5, pp. 1927–1932, 2014.

[13] E. Worthington, "Piezoelectric energy harvesting: Enhancing power output by device optimisation and circuit techniques." PhD Dissertation - Cranfield University, UK, 2010.

[14] R. Vullers, R. van Schaijk, I. Doms, C. Van Hoof, and R. Mertens, "Micropower energy harvesting," *Solid-State Electronics*, vol. 53, no. 7, pp. 684–693, 2009.

[15] W. Liu, A. Badel, F. Formosa, Q. Zhu, C. Zhao, and G.-D. Hu, "A comprehensive analysis and modeling of the self-powered synchronous switching harvesting circuit with electronic breakers," *IEEE Transactions on Industrial Electronics*, vol. 65, no. 5, pp. 3899–3909, 2018.

[16] M. Hayes, "Synergies between energy harvesting and power electronics." IEEE Power Electronics Society, 2016.

[17] D. Guyomar and M. Lallart, "Recent progress in piezoelectric conversion and energy harvesting using nonlinear electronic interfaces and issues in small scale implementation," *Micromachines*, vol. 2, no. 2, pp. 274–294, 2011.

[18] A. Ballato, "Piezoelectricity: history and new thrusts," in *1996 IEEE Ultrasonics Symposium. Proceedings*, vol. 1, pp. 575–583, IEEE, 1996.

[19] W. P. Mason, "Piezoelectricity, its history and applications," *The Journal of the Acoustical Society of America*, vol. 70, no. 6, pp. 1561–1566, 1981.

[20] J. Curie and P. Curie, "Développement par compression de l'électricité polaire dans les cristaux hémièdres à faces inclinées," *Bulletin de minéralogie*, vol. 3, no. 4, pp. 90–93, 1880.

[21] G. Lippmann, "Principe de la conservation de l'électricité, ou second principe de la théorie des phénomènes électriques," *Journal de Physique Théorique et Appliquée*, vol. 10, no. 1, pp. 381–394, 1881.

[22] S. R. Moheimani and A. J. Fleming, *Piezoelectric transducers for vibration control and damping*. Springer Science & Business Media, 2006.

[23] T. Meeker, "Publication and proposed revision of ansi/ieee standard 176-1987," *IEEE Transactions on Ultrasonics Ferroelectrics and Frequency Control*, vol. 43, no. 5, pp. 717–772, 1996.

[24] A. Erturk and D. J. Inman, *Piezoelectric energy harvesting*. John Wiley & Sons, 2011.

[25] H. A. Sodano, D. J. Inman, and G. Park, "A review of power harvesting from vibration using piezoelectric materials," *Shock and Vibration Digest*, vol. 36, no. 3, pp. 197–206, 2004.

[26] A. Erturk and D. J. Inman, "Issues in mathematical modeling of piezoelectric energy harvesters," *Smart Materials and Structures*, vol. 17, no. 6, p. 065016, 2008.

[27] S. Roundy and P. K. Wright, "A piezoelectric vibration based generator for wireless electronics," *Smart Materials and structures*, vol. 13, no. 5, p. 1131, 2004.

[28] N. E. Dutoit, B. L. Wardle, and S.-G. Kim, "Design considerations for mems-scale piezoelectric mechanical vibration energy harvesters," *Integrated Ferroelectrics*, vol. 71, no. 1, pp. 121–160, 2005.

[29] Y. Jeon, R. Sood, J.-H. Jeong, and S.-G. Kim, "Mems power generator with transverse mode thin film pzt," *Sensors and Actuators A: Physical*, vol. 122, no. 1, pp. 16–22, 2005.

[30] H.-B. Fang, J.-Q. Liu, Z.-Y. Xu, L. Dong, D. Chen, B.-C. Cai, and Y. Liu, "A mems-based piezoelectric power generator for low frequency vibration energy harvesting," *Chinese Physics Letters*, vol. 23, no. 3, pp. 732–734, 2006.

[31] A. M. Flynn and S. R. Sanders, "Fundamental limits on energy transfer and circuit considerations for piezoelectric transformers," *IEEE transactions on power electronics*, vol. 17, no. 1, pp. 8–14, 2002.

[32] A. Erturk and D. J. Inman, "A distributed parameter electromechanical model for cantilevered piezoelectric energy harvesters," *Journal of vibration and acoustics*, vol. 130, no. 4, p. 041002, 2008.

[33] A. Erturk and D. J. Inman, "An experimentally validated bimorph cantilever model for piezoelectric energy harvesting from base excitations," *Smart materials and structures*, vol. 18, no. 2, p. 025009, 2009.

[34] C. Lan, L. Tang, and R. L. Harne, "Comparative methods to assess harmonic response of nonlinear piezoelectric energy harvesters interfaced with ac and dc circuits," *Journal of Sound and Vibration*, vol. 421, pp. 61–78, 2018.

[35] W. Wu, A. Wickenheiser, T. Reissman, and E. Garcia, "Modeling and experimental verification of synchronized discharging techniques for boosting power harvesting from piezoelectric transducers," *Smart Materials and Structures*, vol. 18, no. 5, p. 055012, 2009.

[36] A. Wickenheiser, T. Reissman, E. Garcia, and W. Wu, "A study of the transient charging behavior of several approaches to piezoelectric energy harvesting," in *2008 Int. Conf. Adaptive Struct. Technol.*, 2008.

[37] A. M. Wickenheiser, T. Reissman, W.-J. Wu, and E. Garcia, "Modeling the effects of electromechanical coupling on energy storage through piezoelectric energy harvesting," *IEEE/ASME Transactions on Mechatronics*, vol. 15, no. 3, pp. 400–411, 2010.

[38] A. Erturk and D. J. Inman, "On mechanical modeling of cantilevered piezoelectric vibration energy harvesters," *Journal of Intelligent Material Systems and Structures*, vol. 19, no. 11, pp. 1311–1325, 2008.

[39] N. Tran, M. H. Ghayesh, and M. Arjomandi, "Ambient vibration energy

harvesters: A review on nonlinear techniques for performance enhancement," *International Journal of Engineering Science*, vol. 127, pp. 162–185, 2018.

[40] T. Yildirim, M. H. Ghayesh, W. Li, and G. Alici, "A review on performance enhancement techniques for ambient vibration energy harvesters," *Renewable and Sustainable Energy Reviews*, vol. 71, pp. 435–449, 2017.

[41] R. Harne and K. Wang, "A review of the recent research on vibration energy harvesting via bistable systems," *Smart materials and structures*, vol. 22, no. 2, p. 023001, 2013.

[42] Z. Yang, A. Erturk, and J. Zu, "On the efficiency of piezoelectric energy harvesters," *Extreme Mechanics Letters*, vol. 15, pp. 26–37, 2017.

[43] F. Cottone, H. Vocca, and L. Gammaitoni, "Nonlinear energy harvesting," *Physical Review Letters*, vol. 102, no. 8, p. 080601, 2009.

[44] A. Keshmiri, N. Wu, and Q. Wang, "A new nonlinearly tapered fgm piezoelectric energy harvester," *Engineering Structures*, vol. 173, pp. 52–60, 2018.

[45] A. Arrieta, P. Hagedorn, A. Erturk, and D. Inman, "A piezoelectric bistable plate for nonlinear broadband energy harvesting," *Applied Physics Letters*, vol. 97, no. 10, p. 104102, 2010.

[46] Z. Zhou, W. Qin, W. Du, P. Zhu, and Q. Liu, "Improving energy harvesting from random excitation by nonlinear flexible bi-stable energy harvester with a variable potential energy function," *Mechanical Systems and Signal Processing*, vol. 115, pp. 162–172, 2019.

[47] A. J. Lee and D. J. Inman, "Broadband energy harvesting performance of a piezoelectrically generated bistable laminate," in *Sensors and Instrumentation, Aircraft/Aerospace and Energy Harvesting, Volume 8*, pp. 1–14, Springer, 2019.

[48] D. Pan and F. Dai, "Design and analysis of a broadband vibratory energy harvester using bi-stable piezoelectric composite laminate," *Energy Conversion and Management*, vol. 169, pp. 149–160, 2018.

[49] A. Keshmiri and N. Wu, "A wideband piezoelectric energy harvester design by using multiple non-uniform bimorphs," *Vibration*, vol. 1, no. 1, pp. 93–104, 2018.

[50] X. Xie, A. Carpinteri, and Q. Wang, "A theoretical model for a piezoelectric energy harvester with a tapered shape," *Engineering Structures*, vol. 144, pp. 19–25, 2017.

[51] J. Baker, S. Roundy, and P. Wright, "Alternative geometries for increasing power density in vibration energy scavenging for wireless sensor networks," in *3rd international energy conversion engineering conference*, p. 5617, 2005.

[52] A. Erturk and D. Inman, "Broadband piezoelectric power generation on high-energy orbits of the bistable duffing oscillator with electromechanical coupling," *Journal of Sound and Vibration*, vol. 330, no. 10, pp. 2339–2353, 2011.

[53] A. Hajati and S.-G. Kim, "Ultra-wide bandwidth piezoelectric energy harvesting," *Applied Physics Letters*, vol. 99, no. 8, p. 083105, 2011.

[54] Z. Yang and J. Zu, "Comparison of pzn-pt, pmn-pt single crystals and pzt

ceramic for vibration energy harvesting," *Energy Conversion and Management*, vol. 122, pp. 321–329, 2016.

[55] Z. Yang, Z. Qin, and J. Zu, "Charging capacitors using single crystal pmn-pt and pzn-pt energy harvesters coupled with the sshi circuit," *Sensors and Actuators A: Physical*, vol. 266, pp. 76–84, 2017.

[56] G.-T. Hwang, H. Park, J.-H. Lee, S. Oh, K.-I. Park, M. Byun, H. Park, G. Ahn, C. K. Jeong, K. No, *et al.*, "Self-powered cardiac pacemaker enabled by flexible single crystalline pmn-pt piezoelectric energy harvester," *Advanced materials*, vol. 26, no. 28, pp. 4880–4887, 2014.

[57] L. Garbuio, M. Lallart, D. Guyomar, C. Richard, and D. Audigier, "Mechanical energy harvester with ultralow threshold rectification based on sshi nonlinear technique," *IEEE Transactions on Industrial Electronics*, vol. 56, no. 4, pp. 1048–1056, 2009.

[58] M. Lallart and D. Guyomar, "An optimized self-powered switching circuit for non-linear energy harvesting with low voltage output," *Smart Materials and Structures*, vol. 17, no. 3, p. 035030, 2008.

[59] S. Du, Y. Jia, and A. A. Seshia, "An efficient inductorless dynamically configured interface circuit for piezoelectric vibration energy harvesting," *IEEE Transactions on Power Electronics*, vol. 32, no. 5, pp. 3595–3609, 2017.

[60] Z. Chen, M.-K. Law, P.-I. Mak, W.-H. Ki, and R. P. Martins, "Fully integrated inductor-less flipping-capacitor rectifier for piezoelectric energy harvesting," *IEEE Journal of Solid-State Circuits*, vol. 52, no. 12, pp. 3168–3180, 2017.

[61] A. Badel, A. Benayad, E. Lefeuvre, L. Lebrun, C. Richard, and D. Guyomar, "Single crystals and nonlinear process for outstanding vibration-powered electrical generators," *IEEE transactions on ultrasonics, ferroelectrics, and frequency control*, vol. 53, no. 4, pp. 673–684, 2006.

[62] I. Lien, Y. Shu, W. Wu, S. Shiu, and H. Lin, "Revisit of series-sshi with comparisons to other interfacing circuits in piezoelectric energy harvesting," *Smart Materials and Structures*, vol. 19, no. 12, p. 125009, 2010.

[63] Z. Yang, J. Zu, and Z. Xu, "Reversible nonlinear energy harvester tuned by tilting and enhanced by nonlinear circuits," *IEEE/ASME Transactions on Mechatronics*, vol. 21, no. 4, pp. 2174–2184, 2016.

[64] M. Lallart, L. Garbuio, L. Petit, C. Richard, and D. Guyomar, "Double synchronized switch harvesting (dssh): A new energy harvesting scheme for efficient energy extraction," *IEEE transactions on ultrasonics, ferroelectrics, and frequency control*, vol. 55, no. 10, pp. 2119–2130, 2008.

[65] W. Liu, C. Zhao, A. Badel, F. Formosa, Q. Zhu, and G. Hu, "Compact self-powered synchronous energy extraction circuit design with enhanced performance," *Smart Materials and Structures*, vol. 27, no. 4, p. 047001, 2018.

[66] S. Du, Y. Jia, C. Zhao, G. A. Amaratunga, and A. A. Seshia, "A passive design scheme to increase the rectified power of piezoelectric energy harvesters," *IEEE Transactions on Industrial Electronics*, vol. 65, no. 9, pp. 7095–7105, 2018.

[67] Y. Wu, A. Badel, F. Formosa, W. Liu, and A. Agbossou, "Nonlinear vibration

energy harvesting device integrating mechanical stoppers used as synchronous mechanical switches," *Journal of Intelligent Material Systems and Structures*, vol. 25, no. 14, pp. 1658–1663, 2014.

[68] Y. S. Shih, D. Vasic, and W. J. Wu, "A non-contact mechanical solution for implementing synchronized switching techniques for energy harvesting using reed switches," *Smart Materials and Structures*, vol. 25, no. 12, p. 125013, 2016.

[69] N. Kong and D. S. Ha, "Low-power design of a self-powered piezoelectric energy harvesting system with maximum power point tracking," *IEEE Transactions on power electronics*, vol. 27, no. 5, pp. 2298–2308, 2012.

[70] J. Liang and W.-H. Liao, "Improved design and analysis of self-powered synchronized switch interface circuit for piezoelectric energy harvesting systems," *IEEE Transactions on Industrial Electronics*, vol. 59, no. 4, pp. 1950–1960, 2012.

[71] H. Liu, J. Liang, and C. Ge, "A mechatronic power boosting design for piezoelectric generators," *Applied Physics Letters*, vol. 107, no. 14, p. 141902, 2015.

[72] S. Lu and F. Boussaid, "A highly efficient p-sshi rectifier for piezoelectric energy harvesting," *IEEE Transactions on Power Electronics*, vol. 30, no. 10, pp. 5364–5369, 2015.

[73] C. Richard, D. Guyomar, and E. Lefeuvre, "Self-powered electronic breaker with automatic switching by detecting maxima or minima of potential dif-

ference between its power electrodes," *FR2005/003000, publication number: WO/2007/063194*, 2007.

[74] W. Liu, A. Badel, F. Formosa, Q. Zhu, C. Zhao, and G. Hu, "Comparative case study on the self-powered synchronous switching harvesting circuits with bjt or mosfet switches," *IEEE Transactions on Power Electronics*, 2018.

[75] L. Zhu, R. Chen, and X. Liu, "Theoretical analyses of the electronic breaker switching method for nonlinear energy harvesting interfaces," *Journal of Intelligent Material Systems and Structures*, vol. 23, no. 4, pp. 441–451, 2012.

[76] Y. Shu, I. Lien, and W. Wu, "An improved analysis of the sshi interface in piezoelectric energy harvesting," *Smart Materials and Structures*, vol. 16, no. 6, p. 2253, 2007.

[77] Y. Shu and I. Lien, "Analysis of power output for piezoelectric energy harvesting systems," *Smart materials and structures*, vol. 15, no. 6, p. 1499, 2006.

[78] Z. Chen, J. He, J. Liu, and Y. Xiong, "Switching delay in self-powered nonlinear piezoelectric vibration energy harvesting circuit: Mechanism, effects and solution," *IEEE Transactions on Power Electronics*, 2018.

[79] M. W. Shafer, M. Bryant, and E. Garcia, "Designing maximum power output into piezoelectric energy harvesters," *Smart Materials and Structures*, vol. 21, no. 8, p. 085008, 2012.

[80] J. M. Dietl and E. Garcia, "Beam shape optimization for power harvesting," *Journal of Intelligent Material Systems and Structures*, vol. 21, no. 6, pp. 633–646, 2010.

[81] B. Zheng, C.-J. Chang, and H. C. Gea, "Topology optimization of energy harvesting devices using piezoelectric materials," *Structural and Multidisciplinary Optimization*, vol. 38, no. 1, pp. 17–23, 2009.

[82] A. M. Wickenheiser and E. Garcia, "Power optimization of vibration energy harvesters utilizing passive and active circuits," *Journal of Intelligent Material Systems and Structures*, vol. 21, no. 13, pp. 1343–1361, 2010.

[83] J. Brufau-Penella and M. Puig-Vidal, "Piezoelectric energy harvesting improvement with complex conjugate impedance matching," *Journal of Intelligent Material Systems and Structures*, vol. 20, no. 5, pp. 597–608, 2009.

[84] H. Jabbar, H. J. Jung, N. Chen, D. H. Cho, and T. H. Sung, "Piezoelectric energy harvester impedance matching using a piezoelectric transformer," *Sensors and Actuators A: Physical*, vol. 264, pp. 141–150, 2017.

[85] N. Chen, T. Wei, D. S. Ha, H. J. Jung, and S. Lee, "Alternating resistive impedance matching for an impact-type microwind piezoelectric energy harvester," *IEEE Transactions on Industrial Electronics*, vol. 65, no. 9, pp. 7374–7382, 2018.

[86] E. Benkhelifa, M. Farnsworth, A. Tiwari, G. Bandi, and M. Zhu, "Design and optimisation of microelectromechanical systems: a review of the state-of-the-art," *International Journal of Design Engineering*, vol. 3, no. 1, pp. 41–76, 2010.

[87] P. Mangaiyarkarasi, P. Lakshmi, and V. Sasrika, "Enhancement of vibration

based piezoelectric energy harvester using hybrid optimization techniques," *Microsystem Technologies*, pp. 1–10, 2019.

[88] R. I. Bourisli and M. A. Al-Ajmi, "Optimization of smart beams for maximum modal electromechanical coupling using genetic algorithms," *Journal of Intelligent Material Systems and Structures*, vol. 21, no. 9, pp. 907–914, 2010.

[89] M. Farnsworth, A. Tiwari, and R. Dorey, "Modelling, simulation and optimisation of a piezoelectric energy harvester," *Procedia CIRP*, vol. 22, pp. 142–147, 2014.

[90] A. Gosavi, *Simulation-based optimization: parametric optimization techniques and reinforcement learning*. Springer, 2003.

[91] S. S. Rao and F. F. Yap, *Mechanical vibrations*, vol. 4. Prentice Hall, Upper Saddle River, NJ, 2011.

[92] R. G. Ballas, *Piezoelectric multilayer beam bending actuators: Static and dynamic behavior and aspects of sensor integration*. Springer Science & Business Media, 2007.

[93] N. Wu, "Study of forced vibration response of a beam with a breathing crack using iteration method," *Journal of Mechanical Science and Technology*, vol. 29, no. 7, pp. 2827–2835, 2015.

[94] S. Du, Y. Jia, C. Zhao, S.-T. Chen, and A. A. Seshia, "Real-world evaluation of a self-startup sshi rectifier for piezoelectric vibration energy harvesting," *Sensors and Actuators A: Physical*, vol. 264, pp. 180–187, 2017.

[95] V. Aubry and F. Meyer, "Schottky diodes with high series resistance: Limitations of forward i-v methods," *Journal of Applied Physics*, vol. 76, no. 12, pp. 7973–7984, 1994.

[96] 3M Canada, "*3M Scotch-Weld Epoxy.*" [Online]. Available from: *https://www.3mcanada.ca/3M/fixLINK/.* [Accessed 17 April 2019].

[97] Siemens AG, "*LMS SCADAS Mobile.*" [Online]. Available from: *https://www.plm.automation.siemens.com/en/products/lms/testing/scadas.* [Accessed 16 April 2019].

[98] Keysight Technologies, "*4 Channel Analog Oscilloscope.*" [Online]. Available from: *https://www.keysight.com/en/pcx-x2015004/oscilloscopes.* [Accessed 17 April 2019].

[99] PCB Piezotronics, "*PCB ICP Accl..*" [Online]. Available from: *http://www.pcb.com/Home.* [Accessed 10 July 2018].

[100] Diodes Incorporated, "*Diodes and Rectifiers.*" [Online]. Available from: *https://www.diodes.com/.* [Accessed 16 April 2019].

[101] Intel Corporation, "*Intel® Core™ i5-4570 Processor.*" [Online]. Available from: *https://ark.intel.com/content/www/us/en/ark/products/75043/intel-core-i5-4570-processor-6m-cache-up-to-3-60-ghz.html.* [Accessed 16 April 2019].

[102] A. K. Jain, J. Mao, and K. Mohiuddin, "Artificial neural networks: A tutorial," *Computer*, no. 3, pp. 31–44, 1996.

[103] S. Haykin, *Neural networks: a comprehensive foundation*. Prentice Hall PTR, 1994.

[104] J.-R. Chen, "Theory and applications of artificial neural networks." PhD Dissertation - Durham University, UK, 1991.

[105] D. W. Marquardt, "An algorithm for least-squares estimation of nonlinear parameters," *Journal of the society for Industrial and Applied Mathematics*, vol. 11, no. 2, pp. 431–441, 1963.

[106] K. Levenberg, "A method for the solution of certain non-linear problems in least squares," *Quarterly of applied mathematics*, vol. 2, no. 2, pp. 164–168, 1944.

[107] H. Yu and B. M. Wilamowski, "Levenberg-marquardt training," *Industrial electronics handbook*, vol. 5, no. 12, p. 1, 2011.

[108] N. R. Draper and H. Smith, *Applied regression analysis*, vol. 326. John Wiley & Sons, 2014.

[109] J. A. Nelder and R. Mead, "A simplex method for function minimization," *The computer journal*, vol. 7, no. 4, pp. 308–313, 1965.

[110] S. Kirkpatrick, C. D. Gelatt, and M. P. Vecchi, "Optimization by simulated annealing," *science*, vol. 220, no. 4598, pp. 671–680, 1983.

[111] R. L. Haupt and S. E. Haupt, *Practical genetic algorithms*. John Wiley & Sons, 2004.

[112] D. Ackley, *A connectionist machine for genetic hillclimbing*, vol. 28. Springer Science & Business Media, 2012.

[113] S. Surjanovic and D. Bingham, "Vistual library of simulation experiments: Test functions and datasets." [Online]. Available from: *https://www.sfu.ca/ ssurjano/index.html/*. [Accessed 15 April 2019].

[114] R. T. Marler and J. S. Arora, "The weighted sum method for multi-objective optimization: new insights," *Structural and multidisciplinary optimization*, vol. 41, no. 6, pp. 853–862, 2010.

[115] R. T. Marler and J. S. Arora, "Survey of multi-objective optimization methods for engineering," *Structural and multidisciplinary optimization*, vol. 26, no. 6, pp. 369–395, 2004.

[116] I. Guyon, "A scaling law for the validation set training set ratio," *preprint*, 1996.

[117] I. V. Tetko, D. J. Livingstone, and A. I. Luik, "Neural network studies. 1. comparison of overfitting and overtraining," *Journal of chemical information and computer sciences*, vol. 35, no. 5, pp. 826–833, 1995.